©Copyright 2020
Xiayu Linpeng

Dopant Qubits in Direct Band Gap Materials

Xiayu Linpeng

A dissertation
submitted in partial fulfillment of the
requirements for the degree of

Doctor of Philosophy

University of Washington

2020

Reading Committee:

Kai-Mei C. Fu, Chair

Xiaodong Xu

Lukasz Fidkowski

Program Authorized to Offer Degree:
Physics

University of Washington

Abstract

Dopant Qubits in Direct Band Gap Materials

Xiayu Linpeng

Chair of the Supervisory Committee:
Professor Kai-Mei C. Fu
Physics Department

Quantum information is currently one of the most important research fields in physics. The dopant qubits in direct band gap materials are promising candidates to build large-scale photon-based quantum network for applications in quantum computation and quantum communication. In this thesis, we study the optical and spin properties of different dopant systems in order to find the best one as a qubit candidate. The first study of dopant qubits in direct band gap materials was on donors in GaAs, from Yamamoto's group about 10 years ago. The donor qubits in GaAs only have ns-scale dephasing time which is limited by inhomogeneous hyperfine fields in the crystal. In order to improve the coherence time, we study the acceptors in GaAs which use the hole spins as the qubit states instead of the electron spins for donors. As the hole has a Bloch wave function with p-symmetry, the overlap with nuclear spin is zero thus the hyperfine interaction is weaker. However, from our measurements, we find the dephasing time is still in ns-scale. This short dephasing time is because of the long-range dipole-dipole hyperfine interaction together with a non-zero heavy-hole-light-hole mixing.

As the acceptor system does not show specific advantages, we move back to the donor system and study the system in different materials. We have performed a systematic study of the longitudinal spin relaxation time T_1 for donor qubits in three different materials (GaAs, InP, and CdTe). For these three materials, the spin relaxation times are all in ms-scale and our theory study shows the T_1 is limited by phonon interaction mediated by

spin-orbit coupling. Though none of these three materials show great coherence properties, this T_1 study leads to our research on donors in ZnO which is a material with much weaker spin-orbit coupling thus longer T_1. We have demonstrated optical spin initialization and coherent control for donors in ZnO. With these spin-control techniques, we have measured a T_1 up to hundreds of ms, an inhomogeneous dephasing time T_2^* of 17 ns and a spin-echo dephasing time T_2 of 50 μs. The donors in ZnO have T_1 several orders of magnitudes higher than the other dopant systems we have studied. Even though the T_2^* is only in ns-scale, ZnO can potentially get nuclear-spin-free isotopic purification, which can greatly enhance the dephasing time. To utilize donors in ZnO for the quantum network applications, it is necessary to get single donor and high-fidelity spin control. We show our current progress on single donor isolation with focused ion beam and high-fidelity spin control with microwave. Though these two tasks are not accomplished yet, the progress is promising and we expect they can be achieved in the next few years.

TABLE OF CONTENTS

Page

List of Figures . . . iv

List of Tables . . . vi

Chapter 1: Introduction . . . 1
- 1.1 Dopant qubits in direct band gap materials . . . 1
- 1.2 Quantum network based on dopant qubits . . . 4

Chapter 2: Acceptors in strained GaAs . . . 8
- 2.1 Introduction . . . 8
- 2.2 Epitaxial lift-off . . . 9
- 2.3 Sample description . . . 11
- 2.4 Induced strain and Photoluminescence properties . . . 11
- 2.5 Spectrum of THT . . . 15
- 2.6 Optical pumping and T_1 measurement . . . 15
- 2.7 Coherent population trapping and the spin decoherence time T_2^* . . . 17
- 2.8 Theory of the longitudinal spin relaxation time T_1 . . . 21
- 2.9 Theory of the inhomogeneous dephasing time T_2^* . . . 26
- 2.10 Conclusion . . . 27

Chapter 3: Longitudinal spin relaxation of donors in GaAs, InP, and CdTe . . . 28
- 3.1 Introduction . . . 28
- 3.2 Samples and experimental technique . . . 30
- 3.3 Magneto-photoluminescence spectra for GaAs, InP, and CdTe . . . 33
- 3.4 GaAs and CdTe T_1 measurements . . . 35
- 3.5 Experimental Results . . . 36
- 3.6 Theory . . . 39
  - 3.6.1 Low-field spin-relaxation . . . 39
  - 3.6.2 High-field spin-relaxation . . . 41

3.7 Conclusion 50

Chapter 4: Coherence properties of donors in ZnO 52
4.1 Introduction 52
4.2 Setup and Photoluminescence spectrum 54
4.3 Spin initialization and T_1 measurement 55
4.4 Calibration of Spin Population 58
4.5 Optical spin coherent control 59
4.5.1 effective 2-level Hamiltonian 60
4.5.2 Master equation of 4-level density matrix model 61
4.5.3 Experimental data 62
4.6 T_2^* and T_2 measurement 65
4.7 Conclusions 69

Chapter 5: Progress towards single donor isolation with focused ion beam in ZnO 70
5.1 Introduction 70
5.2 Thin film fabrication with FIB 71
5.3 PL measurements on the four FIB thin films 73
5.3.1 PL measurements on the 1st thin film 73
5.3.2 PL measurements on the 2nd thin film 75
5.3.3 PL measurements on the 3rd thin film 77
5.3.4 PL measurements on the 4th thin film 79
5.4 PL quenching effect 81
5.5 Conclusion 81

Chapter 6: Progress towards high-fidelity spin control with microwave pulses in ZnO 83
6.1 Introduction 83
6.2 Selection rules in Voigt geometry and Faraday geometry 84
6.2.1 Selection rules in Voigt geometry 84
6.2.2 Selection rules in Faraday geometry 87
6.2.3 Energy diagram at low fields 88
6.3 Optical pumping in the Faraday geometry 88
6.4 Microwave strength needed for GHz-scale Rabi frequency 91
6.5 Design of the microstrip resonator 92
6.6 Fabrication and characterization of the microstrip resonator 96

6.7 Conclusion 97

Chapter 7: Summary and outlook 98

Appendix A: Supplementary information for longitudinal spin relaxation in GaAs, InP and CdTe 101

A.1 Surface depletion effects 101

A.2 Numerical solution of donor-bound electron in magnetic field 103

A.3 Theory of spin-relaxation via the admixture mechanism 104

A.3.1 General expression for the admixture spin-relaxation rate 104

A.3.2 Numerical calculation of admixture spin-relaxation rate 106

A.3.3 Admixture mechanism in moderate magnetic fields 108

A.4 Spin relaxation via the direct spin-phonon mechanism 112

A.4.1 General expression for the direct spin-phonon spin-relaxation rate . . 112

A.4.2 Numerical calculation of direct spin-phonon spin-relaxation rate . . . 113

A.4.3 Analytic calculation of direct spin-phonon spin-relaxation rate 114

Appendix B: Two routines to make ZnO thin film using FIB 116

B.1 Routine 1: top milling 116

B.2 Routine 2: side milling 119

Bibliography 122

LIST OF FIGURES

Figure Number Page

1.1 Energy diagram and cartoon model of a donor system. 1
1.2 Illustration of quantum network and the protocol to create a two-node network. 4
2.1 ELO process and the change of GaAs PL spectra after the ELO process. . . . 10
2.2 Optical image, PL and PLE spectra of the strained GaAs sample. 13
2.3 Electron and hole Zeeman splitting as a function of magnetic fields. 14
2.4 THT spectra of acceptors in strained GaAs. 16
2.5 Optical pumping and T_1 measurements of acceptors in strained GaAs. 17
2.6 Coherent population trapping of acceptors in strained GaAs. 18
2.7 Energy diagram of the Λ-system. 19
3.1 Energy diagram, PL spectra, optical pumping and T_1 measurements of donors. 32
3.2 Magneto-photoluminescence spectra in the Voigt geometry for donors in GaAs, InP and CdTe. 34
3.3 Energy diagram, PL spectrum, optical pumping and T_1 measurements for donors in CdTe and GaAs. 35
3.4 T_1 as a function of the Zeeman splitting for donor systems in GaAs, InP and CdTe. 36
3.5 T_1 as a function of temperature for InP at different fields. 37
3.6 T_1 as a function of the Zeeman splitting at two different temperatures. 38
3.7 Schematic of spin relaxation mechanisms. 42
3.8 Theoretical results for spin-relaxation time T_1 via the admixture mechanism, using both analytic and numerical wave functions. 44
3.9 Theoretical results for the spin relaxation time via the direct spin-phonon mechanism for GaAs, InP and CdTe. 48
4.1 Experimental geometry, energy diagram, PL spectra and g-factor measurements of donors in ZnO. 54
4.2 TES spectra and the effects of resonant excitation. 56
4.3 Optical pumping and T1 measurements for donors in ZnO. 57
4.4 Calibration of the spin population using the optical pumping curve. 59

4.5 Single-pulse and double-pulse measurements of optical coherent rotation for donors in ZnO. . . . 64
4.6 Measurements of dephasing time for donors in ZnO. . . . 65
4.7 Theoretical distribution of the hyperfine field including both the Ga and ^{6}7Zn nuclei. . . . 67
5.1 SEM images of the four FIB ZnO thin films. . . . 72
5.2 PL measurements on the 1st FIB thin film. . . . 74
5.3 PL measurements on the 2nd FIB thin film. . . . 76
5.4 PL measurements on the 3rd FIB thin film. . . . 78
5.5 PL measurements on the 4th FIB thin film. . . . 80
5.6 Proposed protocol for single donor isolation with FIB. . . . 82
6.1 Illustration of the Voigt and Faraday geometry. The corresponding PL spectra are also plotted to confirm the selection rules. . . . 86
6.2 Energy diagram of the donor system at small magnetic fields in the Voigt geometry and Faraday geometry. . . . 88
6.3 Illustration of the direct-excitation setup and side-excitation setup. . . . 89
6.4 Optical pumping curves at 3 different fields in Faraday geometry: 1 T, 0.3 T, and 0.1 T. . . . 90
6.5 T_1 measurements in the Farraday geometry. . . . 90
6.6 Schematic of a microstrip line. . . . 93
6.7 Design and simulated field distribution in the microstrip resonator. . . . 94
6.8 Simulated reflection spectrum. . . . 94
6.9 Geometry and simulated field distribution of the microstrip transmission line. 95
6.10 Optical image of the resonator chips and the measurements of the reflection spectrum. . . . 96
A.1 Time-resolved photoluminescence during optical pulse. . . . 102
A.2 Energies of excited state orbitals vs. dimensionless magnetic field β from numerical simulation of hydrogen atom in magnetic field. . . . 103
A.3 The overlap integral between the Gaussian approximation for the wavefunction and the numerical solution was maximized as a function of β. . . . 109
B.1 Illustration of the top milling. . . . 116
B.2 Illustration of the side milling. . . . 119

LIST OF TABLES

Table Number Page

2.1 Parameters used to calculate the strain and energy shift in ELO. 12
2.2 Fitting parameters for the 3-level density matrix model without and with broadening. The errors are 2σ errrors from fitting. 20
2.3 Parameters used to calculate T_1. Parameters Δ and $|g_{HH}^{\perp}|$ are determined from experiments. 26
3.1 Sample parameters of GaAs, InP and CdTe used in the T_1 measurements. . . 31
3.2 Material parameters relevant to the donor-bound electron spin relaxation in GaAs, InP, and CdTe. 45
4.1 Parameters used for the simulation. 63

ACKNOWLEDGMENTS

The work in this thesis can not be finished without the help and support from many people.

First, I would like to thank my advisor Kai-Mei Fu who gives me the opportunity to explore all the different research topics. I cannot imagine a better advisor than Kai-Mei. She not only discusses the physics with us but also helps us a lot in the real experiments. Without her help, I would not be able to keep my research on track during the 6 years PhD program. I would also like to thank the members in my reading committee: Xiaodong Xu and Lukasz Fidkowski for their expertise in condensed matter physics.

I was new to optics when I first came to the group. I would like to thank Todd Karin and Sarah Harvey, who gave me the first lesson on optical experiments. I also learnt from Todd on all the other research abilities such as programming, presentation and writing. Maria Viitaniemi and Vasileios Niaouris has helped me a lot on the experiments in ZnO. Mikhail V. Durnev and Mikhail M. Glazov contribute significantly on the theory of spin relaxation. I have collaborated closely with Ding Zhong, Pasqual Rivera, and Kyle Seyler on experiments in 2D materials, from which I have gained better understandings in condensed matter physics and optical experiments. I also acknowledge the collaboration with Cameron Johnson, Kelsey Bates, Bethany Matthews, Steven R. Spurgeon, David Peterson, and Scott Braswell.

I would like to also acknowledge the other past and present members in the Fu lab for providing excellent research environments: Michael Gould, Ed Kleinsasser, Nicole Thomas, Yaxuan Zhou, Srivatsa Chakravarthi, Christian Pederson, Zeeshawn Kazi, Alan Logan, Christopher Munley, Emma Schmidgall, Chris Moore, Lilli Thiel, Nick Brunelle, Isaiah Kim, April Opsvig, Ian Christen, Maya Dunn, Seth Hyra, Brianna Birkel, andd Matthew Stanfield.

Next, I want to thank the Physics department at the University of Washington, especially our graduate program advisor Catherine Provost for all the helps when I first came here.

I also want to acknowledge all the sample growth collaborators: Andreas D. Wieck and Arne Ludwig for the p-type GaAs MBE sample, Aswin Vishnuradhan, M. Kawasaki and Y. Kozuka for the ZnO crystals, S. P. Watkins for the MOCVD InP and ZnO nanowires, Satoru Seto for the CdTe crystal.

At last, I want to thank my friends and my parents for the support and love over the years.

Chapter 1

INTRODUCTION

1.1 Dopant qubits in direct band gap materials

A qubit (quantum bit) is a quantum two-level system that is used as the building block for quantum applications. A dopant atom in a semiconductor is an atom that has different valence electrons than the other atoms in the crystal. It can either be a donor (with one more electron) or an acceptor (with one less electron, or with a hole). The spin states of the electron or hole are utilized as the qubit states. A dopant qubit is a relatively simple system that can be described with the effective-mass picture. In the effective-mass approximation, the dopant system contains a dopant center and an electron or a hole surrounding it, similar to a hydrogen atom but we need to use the effective electron or hole mass and the effective dielectric constant. The ground spin states of the dopant qubit can be coupled to the excited states, i.e. the donor bound exciton (D^0X) or acceptor bound exciton (A^0X), forming a Λ-system, as shown in Fig. 1.1. Spin control and readout can be realized by utilizing the two

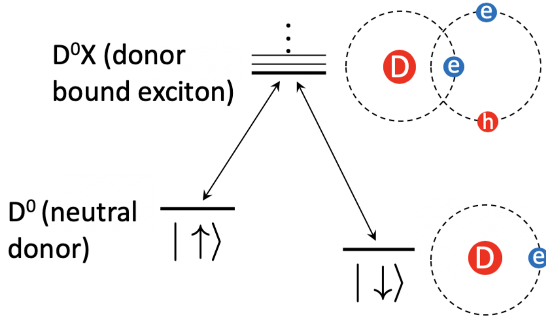

Figure 1.1: Energy diagram and cartoon model of a donor system. In the cartoon model, 'D' denotes donor center, 'e' denotes electron, and 'h' denotes hole. The acceptor system has a similar structure with the following changes: e→h, h→e, and D→A. 'A' denotes acceptor center.

optical transitions in the Λ-system.

In the past decades, research of dopant qubits is mostly focused on silicon donors [1, 2, 3] due to the advantage of mature silicon fabrication techniques. Numerous methods have been developed to improve the qubit quality and spin control fidelity for donors in silicon. Ultra-pure isotopically purified silicon is synthesized to achieve near-second spin coherence time [1]. Nanoscale positioning of single donors is developed to precisely engineer the interaction between different donors [2]. However, because silicon is an indirect band gap material, the optical transitions for the donor systems are not efficient [4, 5, 6]. This prevents the usage of silicon donors in photon-based applications such as long-distance quantum communication and large-scale quantum networks [4, 7, 8]. In our work, we study the dopant qubits in direct band gap materials including GaAs, InP, CdTe, and ZnO. Potentially, they can have long coherence times and high-fidelity spin control similar to silicon donors. Additionally, they have high-efficient optical transitions, which are suitable for photon-based remote entanglement and large-scale quantum networks.

Some pioneering work has been done in Yamamoto's group about 10 years ago, in which they have studied donors in GaAs [9, 10, 11, 12]. Basic spin-control techniques have been developed and spin coherence properties have been measured. The donors in GaAs show ms-scale spin relaxation time T_1 and ∼2 ns inhomogeneous dephasing time T_2^*. As GaAs is a III-V compound, both Ga and As have no stable isotopes with zero nuclear spins, it is not possible to increase the coherence time through isotopic purification. The short T_2^* for donors in GaAs makes it not a promising candidate for qubit applications.

One major goal of our study is to test different dopant systems and find the most suitable one for qubit applications [13, 14, 15]. The first system we explore is the acceptor in GaAs, discussed in Chapter 2. Different from the s-symmetry for electrons, the Bloch wave function of holes in GaAs has a p-symmetry. Therefore, the wave function overlap of the hole with the nearby nuclei is zero, leading to a much weaker hyperfine interaction. As the inhomogeneous hyperfine field is the main source for the dephasing, the coherence time for acceptors is expected to be much longer than that of donors. One challenge to study the acceptors in bulk GaAs is the degeneracy of heavy hole (HH) and light hole (LH). Due to this degeneracy, the hole is a 4-level system and there is fast spin relaxation (less than

nanosecond) between the HH and LH states. To lift the HH-LH degeneracy, we apply strain to the GaAs sample through epitaxial lift-off (ELO), i.e. transferring a thin epitaxial GaAs layer to a non-GaAs substrate. This strain introduces a HH-LH splitting and allows us to study just the HH subband. However, we experimentally find that the T_2^* is still in ns-scale, ~7 ns. Theoretically we determine that the short T_2^* is limited by a HH-LH mixing originating from a small shear strain introduced to the sample during the ELO process. This hole mixing could be improved with the help of strain engineering techniques such as piezoelectric actuators which could provide larger and more homogeneous strain.

As the acceptor system is not so promising, we move back to the donor system. Chapter 3 shows our study of spin relaxation time for donors in three different semiconductors: GaAs, InP, and CdTe. For all of the materials, the spin relaxation time has a B^{-3} to B^{-4} dependence on magnetic fields. We find that the observed T_1 can be explained with an electron-phonon interaction mediated by spin-orbit coupling. As the donor system is a relative simple system that can be well described by the effective-mass picture, the theoretical model can be calculated quantitatively. Good agreements with the experiments are obtained on GaAs and CdTe. The measured T_1 of GaAs, InP and CdTe is in the scale of 1 ms, which is not long enough for qubit applications. To get longer T_1, we need to use a material with weaker spin-orbit coupling. This leads to our study of donors in ZnO which has much weaker spin-orbit coupling than the other three materials.

In Chapter 4, we present a detailed characterization of donors in ZnO, including the photoluminescence (PL) spectroscopy, spin-control techniques, and measurements of the spin coherence properties. For the ZnO donors, the spin is initialized using optical pumping with a ~95% fidelity at high magnetic fields. The spin coherent rotation is realized with an ultra-fast laser pulse. With these spin-control techniques, we measure a spin relaxation time T_1 up to 0.1 s, an inhomogeneous dephasing time T_2^* of 17 ns, and a spin-echo dephasing time T_2 of 50 μs. Even though the measured dephasing time in this natural ZnO sample is still in ns-scale, it can be greatly enhanced by isotopic purification as only 4.1% of Zn and 0.038% of O have nuclear spins.

In order to utilize the donors for quantum network, it is necessary to isolate single donor and get high-fidelity spin control (see Sec. 1.2). In Chapter 5 and Chapter 6, we

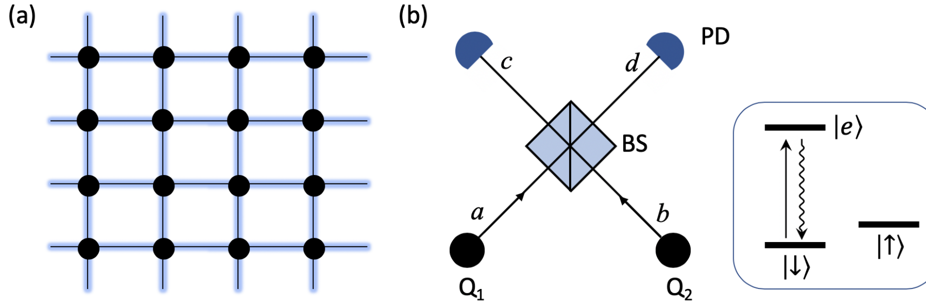

Figure 1.2: (a) Illustration of a 2D quantum network. (b) A protocol for heralded entanglement generation of a two-node network based on photon interference. BS: beam splitter. PD: photodiode.

show our progress on single donor isolation with focused ion beam (FIB) and high-fidelity spin control with microwave. With FIB, we fabricate sub-micrometer ZnO thin films and perform a PL study on the fabricated samples. Though single donor isolation is not achieved in the fabricated thin films, this PL study could give a good guidance on future experiments that utilize FIB to isolate single donors. For the microwave spin control, there are two main challenges: achieving optical pumping at low fields in the presence of inhomogeneous optical broadening and getting a high enough microwave field amplitude to perform coherent spin control within the 17 ns T_2^* time. Optical pumping at low fields is realized by selectively exciting the spin transition with circular polarization in the Faraday geometry. We have demonstrated optical pumping at magnetic field down to 0.3 T with relatively good fidelity. To obtain a high enough microwave amplitude at the donor position, we have designed a microstrip resonator that provides strong in-plane field strength. With the resonator structure, the desired 0.1 GHz Rabi frequency of the electron spins can be achieved with an input microwave power of ~2 W.

1.2 Quantum network based on dopant qubits

The ultimate goal of our work is to utilize the dopant qubits to build a large-scale quantum network [4, 16]. A quantum network consists of quantum nodes that are connected through remote entanglement [17]. Each quantum node consists of multiple qubits that can be

entangled through local interaction, e.g. an electron spin coupled to nearby nuclear spins through the hyperfine interaction [18]. This quantum network can be useful for both long-distance quantum communication and measurement-based quantum computation. A major challenge of building a large-scale quantum network is how to efficiently create the remote entanglement between quantum nodes. Figure 1.2 (b) shows a typical protocol to create a two-node network based on photon interference. Each node in this protocol is just a single qubit, an electron spin with $|\uparrow\rangle$ and $|\downarrow\rangle$ states. The ground $|\uparrow\rangle$ and $|\downarrow\rangle$ states can be coupled to the excited state $|e\rangle$ optically. The excitation laser is tuned on resonance with $|\downarrow\rangle \leftrightarrow |e\rangle$ transition. With an optical π-pulse, the spin $|\downarrow\rangle$ is excited to $|e\rangle$, then it relaxes and emits a photon. To create the remote entanglement, the two qubits are first prepared in a superposition state of $|\uparrow\rangle$ and $|\downarrow\rangle$:

$$|\Psi\rangle = (\alpha\,|\uparrow\rangle + \beta\,|\downarrow\rangle) \otimes (\alpha\,|\uparrow\rangle + \beta\,|\downarrow\rangle), \tag{1.1}$$

where α and β satisfy $|\alpha|^2 + |\beta|^2 = 1$. Then the optical π-pulses are applied to both qubits.

$$|\Psi\rangle = (\alpha\,|\uparrow\rangle + \beta\,|e\rangle) \otimes (\alpha\,|\uparrow\rangle + \beta\,|e\rangle), \tag{1.2}$$

The excited state $|3\rangle$ emits a photon on the timescale of its radiative lifetime.

$$|\Psi\rangle = (\alpha\,|\uparrow\rangle + \beta\,|\downarrow\rangle\,a^\dagger) \otimes (\alpha\,|\uparrow\rangle + \beta\,|\downarrow\rangle\,b^\dagger), \tag{1.3}$$

where $a^\dagger$ ($b^\dagger$) is the creation operator of a photon at path a (b). At the beam splitter, operators $a^\dagger$ and $b^\dagger$ transform according to

$$\begin{aligned} a^\dagger &\to \frac{\sqrt{2}}{2}(d^\dagger + ic^\dagger), \\ b^\dagger &\to \frac{\sqrt{2}}{2}(c^\dagger + id^\dagger). \end{aligned} \tag{1.4}$$

Therefore, the quantum state becomes:

$$
\begin{aligned}
|\Psi\rangle &= (\alpha\,|\uparrow\rangle + \frac{\sqrt{2}}{2}\beta\,|\downarrow\rangle\,d^\dagger + i\frac{\sqrt{2}}{2}\beta\,|\downarrow\rangle\,c^\dagger) \otimes (\alpha\,|\uparrow\rangle + \frac{\sqrt{2}}{2}\beta\,|\downarrow\rangle\,c^\dagger + i\frac{\sqrt{2}}{2}\beta\,|\downarrow\rangle\,d^\dagger) \\
&= \alpha^2\,|\uparrow\uparrow\rangle + \alpha\beta\frac{\sqrt{2}(|\uparrow\downarrow\rangle + i\,|\downarrow\uparrow\rangle)}{2}c^\dagger + \alpha\beta\frac{\sqrt{2}(|\downarrow\uparrow\rangle + i\,|\uparrow\downarrow\rangle)}{2}d^\dagger \\
&+ i\frac{\beta^2}{2}\,|\downarrow\downarrow\rangle\,(d^\dagger d^\dagger + c^\dagger c^\dagger).
\end{aligned}
\tag{1.5}
$$

If there is a click at the photodiode in path d, the conditional possibility is $|\alpha|^2$ for a single-photon event, which corresponds to the two-qubit entangled state $(|\downarrow\uparrow\rangle + i\,|\uparrow\downarrow\rangle)/\sqrt{2}$. There is also a possibility of $|\beta|^2$ for a two-photon event, which corresponds to the qubit state of $|\downarrow\downarrow\rangle$. The parameter β is set to be small so that the two-photon event is less likely to happen. However, a smaller β also leads to smaller success probability for the single-photon event. In the experiment, the choice of β needs to be balanced between high fidelity and high success probability. In this single-photon protocol, the speed of entanglement generation depends linearly on the photon collection efficiency.

In the single-photon protocol, the fidelity of the entanglement is always imperfect due to the existence of the two-photon event $|\downarrow\downarrow\rangle$. To eliminate the error due to the two-photon events, we can use a two-photon protocol: after detecting the first photon, we can apply a π-pulse to both qubits and perform this photon detection process again. The $|\downarrow\downarrow\rangle$ state in Eq. 1.5 changes to $|\uparrow\uparrow\rangle$ due to the π-pulse and do not emit photon in the second photon detection process. With this double-photon protocol, the parameter β can be set at $\sqrt{2}/2$ and the fidelity of the entanglement can theoretically be 100% if all quantum gates are perfect. However, the success probability is much lower than the single-photon protocol as the success probability is proportional to the square of the detection efficiency which is typically really small [19]. The remote entanglement protocols have been realized in both nitrogen-vacancy centers and hole quantum dots [19, 17, 20]. The hole quantum dots have high radiative efficiency but the generated entangled state does not have a high fidelity due to the short coherence time of the qubits. In contrast, the nitrogen-vacancy centers have long spin coherence time but a low radiative efficiency at the zero phonon line.

To utilize the photon-based protocols for the entanglement generation, there are several

requirements for the qubits.

1. **Single qubit isolation**: The system can be separated into different single qubits. Each qubit can be controlled individually.

2. **Identical qubits**: The photon emitted from different qubits need to be indistinguishable so the interference can happen at the beam splitter.

3. **High radiative efficiency**: The qubit needs to have high radiative efficiency at the zero phonon line (ZPL) in order to have fast entanglement generation.

4. **High-fidelity qubit control**: The qubit states can be coherently controlled with high fidelity in order to create the desired quantum states.

5. **Long coherence**: The qubit needs to have long coherence times so that the quantum states do not decay significantly during the entanglement generation.

Donors in ZnO can potentially satisfy all the requirements. Requirement 1: Single donor isolation can be achieved in high-purity ZnO crystal with small donor density. This will require ZnO crystals with higher chemical purity than the samples in our current study. We are also working on reducing the donor numbers in our current samples by physical methods such as focused ion beam. Requirement 2: The inhomogeneous linewidth in a natural ZnO sample is in the order of 20 GHz. This value can possibly be reduced to the lifetime limited linewidth, $\sim$0.2 GHz, with chemical and isotopic purification. Another method is to tune the photon frequencies on resonance with each other using strain or the DC Stark effect. Requirement 3: The dopant qubits in direct band gap materials typically have near unity radiative efficiency at the ZPL. This is the specific advantage of donors in direct band gap materials compared to other qubit systems. Requirement 4: Similar to donors in silicon, donors in ZnO should also be able to achieve high-fidelity spin control with microwave. Requirement 5: Our measurements have shown donors in ZnO have spin relaxation times up to hundreds of ms while the dephasing time is only in ns-scale. With nuclear-spin-free isotopic purification, spin dephasing time up to ms-scale might be achievable.

Chapter 2

ACCEPTORS IN STRAINED GAAS

2.1 Introduction

Spin systems in semiconductors have been actively studied due to the potential applications for nanoscale spintronics and quantum information technologies. Most efforts are focused on electron spins in low-dimensional systems, e.g. quantum dots (QDs) and donors [20, 14]. However, due to the hyperfine interaction with the nuclei in the crystals, the coherence time of electron spins is short, typically on the nanosecond scale. Isotopic purification can significantly reduce this effect in group-IV and group II-VI semiconductors, e.g. in diamond and silicon. For group III-V semiconductors such as GaAs, this technique is not applicable as there is no stable isotope with zero nuclear spins. An alternative solution is to use hole spins which have much weaker contact hyperfine interaction due to the p-symmetry of the hole Bloch wave function. Research in III-V QDs has shown µs-scale hole spin coherence time [21, 22], compared to ns-scale in electron spins [23, 12]. Spin control techniques such as optical pumping, coherent population trapping (CPT) and ultra-fast optical control have been demonstrated [21, 22, 24]. Remote entanglement between two hole spins has been performed leveraging this enhanced coherence time [20]. In addition to the enhanced coherence properties, faster electronic gate operations are possible due to large spin-orbit interaction, demonstrated in silicon and germanium QDs [25, 26].

A hole bound to an acceptor is an analogous spin qubit system to a hole-doped QD with the added feature of high optical homogeneity [27]. Different QDs could have different emission energy due to the different shape and strain in the QDs. For the acceptor system, the wave function is just determined by the Coulomb interaction between the acceptor and bound carriers. Therefore, the optical transitions of different acceptors have similar energy,

---

This chapter is a slightly modified version of a paper in preparation written by the author of this thesis [15].

which is useful for the applications of quantum networks. However, it is challenging to utilize the acceptors in a bulk GaAs crystal. Due to the degeneracy of the heavy hole (HH) and light hole (LH) valence bands, the strong spin-orbit interaction results in a short spin relaxation time, typically much less than 1 ns [28, 29]. This is not a problem in QDs as the interaction between HH and LH is significantly suppressed by the large HH-LH splitting (tens of meV) [30, 31] due to the strain and spatial confinement. By analogy, if a large strain can be introduced to a p-doped GaAs crystal, relaxation times much longer than ns should also be achievable for hole spins bound to acceptors.

In this chapter, we apply 0.042% compressive strain to a GaAs epitaxial layer and study the optical and spin properties of an ensemble of acceptors. We demonstrate spin control such as optical pumping and CPT for acceptor systems in this strained GaAs sample. Microsecond-scale longitudinal hole spin relaxation time T_1 is observed. The measured field dependence of T_1 can be explained by a combination effect of a hole-phonon interaction through the deformation potentials and a HH-LH mixing due to an in-plane magnetic field. A ~7 ns decoherence time T_2^* is extracted from the CPT measurements. This time is much shorter than the measured >100 ns T_2^* for single hole spins in III-V QDs determined by similar CPT measurements [21, 22]. We attribute the short measured T_2^* in our strained GaAs sample to the dipole-dipole hyperfine interaction modified by the HH-LH mixing from a weak shear strain in the sample. This effect is weaker in QDs due to the much larger HH-LH splitting and thus smaller hole mixing. The work in this chapter is the first demonstration of spin control and measurements for the acceptor system in bulk GaAs with a strain induced HH-LH splitting. Though the measured T_1 and T_2^* are relatively short, from our theoretical model, we show that both of them can be improved by increasing the HH-LH mixing and reducing the hole mixing. This can possibly be achieved by applying larger and more homogeneous strain with techniques such as wafer bonding [32] or a piezoelectric actuator [33].

2.2 Epitaxial lift-off

The strain is introduced to GaAs through the epitaxial lift-off (ELO) process. The as-grown GaAs sample contains a thin GaAs epitaxial layer, a 100 nm AlAs sacrificial layer and the

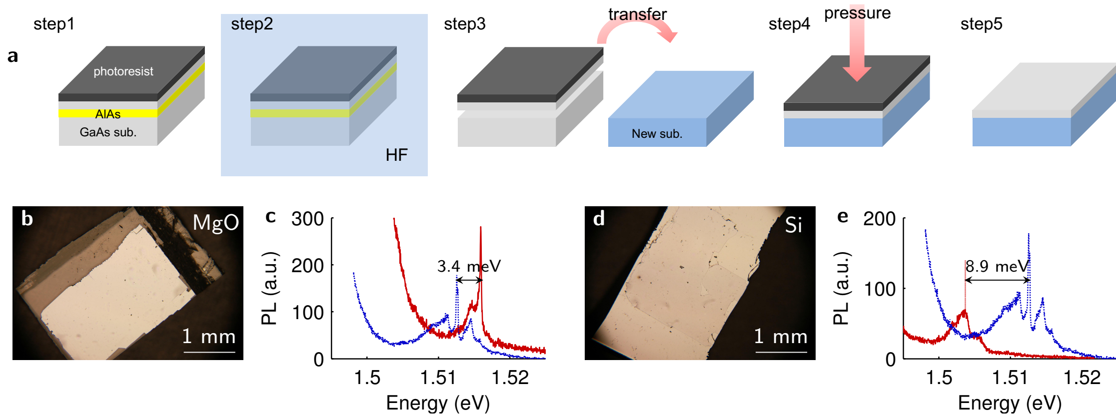

Figure 2.1: (a). Procedure of the epitaxial lift off. (b) and (c). The optical microscope photo and the PL spectrum of GaAs epitaxial layer transferred to MgO. The blue curve is for the sample before ELO and the red curve is for the sample after ELO. (d) and (e). The optical microscope photo and the PL spectrum of GaAs epitaxial layer transferred to Si.

GaAs substrate. The ELO process is as shown in Fig 2.1(a).

1. A ∼1 mm thick photoresist layer is applied to the membrane before the etching for protection. The photoresist creates a small bending on the epitaxial layer to let the acid etch in during step 2.

2. The sample is put in 5% hydrofluoric (HF) acid overnight. The acid selectively etches the AlAs sacrificial layer.

3. After the etching, the membrane is transferred to a beaker with water for cleaning and then to a non-GaAs substrate. A thin paper tissue is used to wick the water out between the epitaxial layer and the MgO substrate.

4. The sample is then put in a membrane box (SPI membrane storage box, square) to add pressure on top of the GaAs epitaxial layer to improve bonding with the new substrate.

5. After waiting for ∼3 days, the sample is taken out and the photoresist on top of the epitaxial layer is removed by putting the sample in hot solvent for several mins.

Two test samples are used to verify the effectiveness of the ELO technique, as shown in Fig. 2.1(b-e). The GaAs epitaxial layers are transferred to a MgO substrate to create a compressive strain and to a Si substrate to create a tensile strain. Photoluminescence (PL) spectra before and after ELO are taken to confirm the induced strain. Due to the deformation potential in GaAs, compressive strain induces a blue shift and tensile strain induces a red shift in the PL spectra. The theory of this is further discussed in Sec. 2.4. From the PL spectra, a 3.4 meV blue shift is introduced for the GaAs sample transferred to a MgO substrate and an 8.9 meV red shift is introduced for the GaAs sample transferred to a Si substrate. These two GaAs samples are n-type samples so the major PL peaks are from donors instead of acceptors. The remaining of this chapter will be focused on a p-type GaAs sample transferred to a MgO substrate as described in Sec. 2.3.

2.3 Sample description

The studied strained sample consists of a 2 µm (001) p-type GaAs epitaxial layer on a MgO substrate. The GaAs layer is doped with carbon with an acceptor density of $\sim 2.5\times10^{14}$ cm^{-3}, determined from Hall measurements. The GaAs is transferred and bonded to the MgO substrate through the ELO process at room temperature. The compressive strain is introduced to GaAs when the sample is cooled down to 1.5 K due to the different thermal expansion rate of GaAs and MgO. The MgO substrate is chosen as the carrier as it is transparent at the band gap of GaAs and can produce significant compressive strain due to the large magnitude difference of the thermal expansion coefficient compared to GaAs. An optical microscope image of the transferred GaAs epitaxial layer on MgO is shown in Fig. 2.2(a). We note that this ELO method is not perfect; some cracking is observed, and the possible slippage between the membrane and substrate can result in both strain reduction and strain inhomogeneity.

2.4 Induced strain and Photoluminescence properties

The sample is mounted in a helium immersion cryostat which is cooled down to 1.5 K. Assuming the GaAs epitaxial layer is perfectly bonded to the MgO substrate at room temperature, the induced strain due to the different thermal expansion rates of GaAs and

MgO is

$$\varepsilon = \frac{(c_g k_g - c_m k_m)\Delta T}{c_g}, \tag{2.1}$$

where ε is the induced strain in GaAs, c_g (c_m) and k_g (k_m) are the lattice constant and thermal expansion rate for GaAs (MgO), and $\Delta T \simeq -298.5$ K is the temperature change of the GaAs sample. Under the induced compressive strain, the change of the band gap energy is

$$\Delta E = 2(a_c - a_v) \cdot (1 - \frac{C_{12}}{C_{11}}) \cdot \varepsilon, \tag{2.2}$$

with a corresponding HH-LH splitting of

$$E_{HH} - E_{LH} = 2b(1 + 2\frac{C_{12}}{C_{11}}) \cdot \varepsilon, \tag{2.3}$$

where a_c, a_v, b are the deformation potential constants and C_{ij} are the elastic stiffness tensor in GaAs [34]. The material parameters are summarized in Table 2.1. Theoretically, a 0.059% compressive strain should be introduced to the GaAs epitaxial layer. We note that we have ignored the small change of thermal expansion rate with temperature [35]. Based on this estimation, the corresponding band-edge energy shift is 5.4 meV and the HH-LH splitting is 3.8 meV.

Figure 2.2(b) shows the photoluminescence (PL) spectra before and after ELO at 0 T and 1.5 K. The main sharp peaks are from the transitions between the acceptor bound exciton (A^0X) and the neutral acceptor (A^0) states. In the unstrained sample, the HH and LH states are degenerate resulting in three acceptor peaks Γ_3, Γ_5 and Γ_1 [27]. These three peaks originate from different combination of the HH and LH states in A^0X and the energy

a_c (eV)	a_v (eV)	C_{12}/C_{11}	b (eV)
-7.17 [34]	1.16 [34]	0.4526 [34]	-1.7 [34]

c_g ($\AA$)	c_m ($\AA$)	k_g (K^{-1})	k_m (K^{-1})
5.653	4.212	5.8×10^{-6} [36]	10.42×10^{-6} [35]

Table 2.1: Parameters used to calculate the strain and energy shift in ELO.

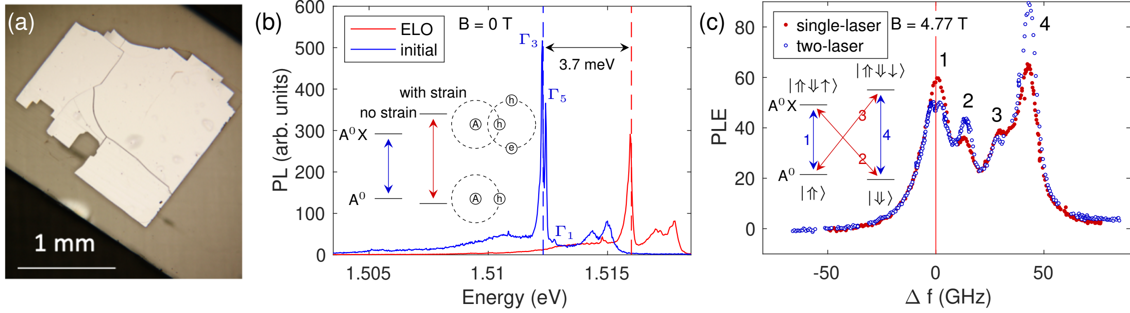

Figure 2.2: (a) Optical microscope image of the a GaAs epitaxial layer transferred to the MgO substrate. (b) PL spectra of the GaAs epitaxial layer before and after ELO process at 1.5 K and 0 T. Excitation at 1.653 eV with 80 nW power. The laser spot diameter is ∼1 µm. The inset shows the cartoon model of the acceptor systems and how the energy changes with strain between A^0 and A^0X. In the cartoon diagram, "A" denotes the acceptor center, "h" denotes hole, and "e" denotes electron. (c) Single-laser and two-laser PLE spectra at 1.5 K and 4.77 T. We note that we have used background subtraction on both spectra where we use the PLE intensity at large Δf as the background. The single-laser PLE spectrum is taken by scanning a laser across all four transitions and collecting the signal from the two hole transition (THT). A typical THT spectrum is shown in Sec. 2.5. The two-laser PLE spectrum is taken with a second laser fixed at the energy of transition 1. Δf is the detuning of the scanning laser compared to the energy of transition 1. Both lasers are at 1 µW and 45 degree polarization between horizontal (parallel to the magnetic field) and vertical (perpendicular to the magnetic field). The laser spot diameter is ∼1 µm. The inset shows the energy structure of the acceptor system. Transitions 1, 2 (3, 4) are polarized in the horizontal (vertical) direction.

splitting between them is due to hole-hole interaction and crystal field [27]. In the strained sample, as there is a large HH-LH splitting, the holes in A^0X are HH-only thus there is just one PL peak, as shown in Fig. 2.2(b). Compared with the unstrained sample, a ∼3.7 meV blue shift of the acceptor transition is observed on the ELO sample. This energy shift is used as an estimation for the change in band gap energy. We note that we have ignored the change of exciton binding energy with strain in the estimation. This 3.7 meV blue shift corresponds to a ∼0.041% compressive strain and ∼2.6 meV HH-LH splitting. These values match reasonably well with our theoretical estimation. As the 2.6 meV HH-LH splitting is much larger than the 0.13 meV thermal energy at 1.5 K, the majority of the holes are in the HH-like ground states.

The spin state of A^0 in this strained sample is determined by the heavy hole with $m_h = \pm 3/2$, denoted by $|\Uparrow\rangle$ and $|\Downarrow\rangle$. The A^0X contains two holes and one electron. As the two holes are in a spin anti-parallel state, the allowed states are $|\Uparrow\Downarrow\uparrow\rangle$ and $|\Uparrow\Downarrow\downarrow\rangle$, where $|\uparrow\rangle$ ($|\downarrow\rangle$) denotes the electron spin state. As shown in the inset of Fig. 2.2(c), in an in-plane magnetic field ($\mathbf{B}\perp[001]$), there are four allowed optical transitions: transitions 1 ($|\uparrow\rangle \leftrightarrow |\Uparrow\Downarrow\uparrow\rangle$) and 4 ($|\downarrow\rangle \leftrightarrow |\Uparrow\Downarrow\downarrow\rangle$) polarized in the horizontal direction (parallel to the magnetic field), and transitions 2 ($|\downarrow\rangle \leftrightarrow |\Uparrow\Downarrow\uparrow\rangle$) and 3 ($|\uparrow\rangle \leftrightarrow |\Uparrow\Downarrow\downarrow\rangle$) polarized in the vertical direction (perpendicular to the magnetic field). A single-laser photoluminescence excitation (PLE) spectrum is taken to resolve all four transitions, as shown in Fig. 2.2(c). The PLE spectrum is taken by scanning a laser across all 4 transitions and collecting the signal from THT transitions (see Sec. 2.5). The inhomogenous linewidth of the acceptor transitions is $\sim$10 GHz. The splittings between the four peaks corresponds to the electron and hole Zeeman splittings in the Voigt geometry ($\mathbf{B}\perp[001]$). The measured electron and hole g-factors are $|g_e^\perp| = 0.432$ and $|g_h^\perp| = 0.155$, as shown in Fig. 2.3.

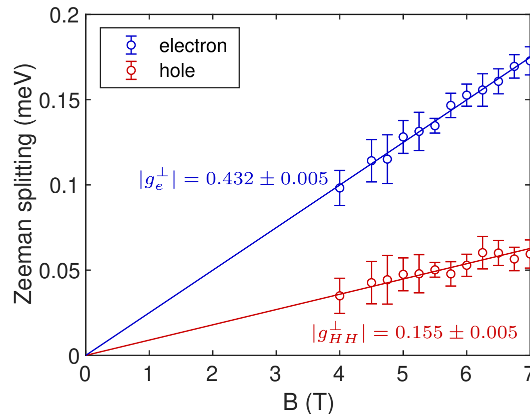

Figure 2.3: Electron and hole Zeeman splitting as a function of magnetic fields. The Zeeman splittings are extracted from PL spectra at different fields with horizontal and vertical polarization.

A two-laser PLE spectrum is taken to confirm the validity of the energy diagram. The two-laser PLE spectrum is taken by fixing one laser at transition 1 and scanning a second laser across all four transitions. Compared to the single-laser PLE, there is a decrease in

signals from transitions 1 and 3, and an enhancement of transitions 2 and 4. These changes are consistent with the effect of optical pumping where the fixed laser pumps the spin states from $|\Uparrow\rangle$ to spin $|\Downarrow\rangle$. Signals from transitions 1 and 3 (2 and 4) decrease (increase) as the intensity of these two transitions are proportional to the population in $|\Uparrow\rangle$ ($|\Downarrow\rangle$). Additionally, a small dip in peak 1 is observed which is attributed to spectral hole burning. A fit of the dip shows a homogeneous linewidth of ~1 GHz, corresponding to a ~0.2 ns A^0X radiative lifetime, which is in reasonable agreement with experimental measurements [27]. A small dip in peak 2 is expected due to CPT which will be further discussed in Section 2.7. However, due to the scan resolution and low intensity of both lasers, the CPT dip is not clearly resolved in this spectrum.

2.5 Spectrum of THT

The two hole transitions (THT) are the transitions from the A^0X state to a higher orbital A^0 state. The wave function A^0 is hydrogen like. The main donor lines are from A^0X to n=1 states of A^0. The THT transitions are from A^0X to n>1 states of A^0, as shown in Fig. 2.4. For all the PLE spectra, we collect the signal from the n=2 THT transition.

2.6 Optical pumping and T_1 measurement

In the $A^0 \leftrightarrow A^0X$ system, the A^0 holes can be initialized to a certain spin state by optical pumping. As shown in Fig. 2.5(a), a 5 µs laser pulse is applied resonantly on transition 1 so the spin states are pumped from spin $|\Uparrow\rangle$ to spin $|\Downarrow\rangle$. The PL signal from transition 2, which is proportional to the population of $|\Uparrow\rangle$, is recorded during the optical pumping pulse. A decrease of the spin population is clearly observed, indicating partial spin initialization is achieved.

The spin relaxation time T_1 is measured by initializing the spin to $|\Downarrow\rangle$, and measuring the recovery of the PL from transition 2 as a function of variable time τ. A single exponential fit is used to extract T_1 from the recovery curve, as shown in Fig. 2.5(b). T_1 as function of magnetic field at different spots on the sample is shown in Fig. 2.5(c). Between 5 and 7 T, T_1 at different spots is similar, following approximately a B^{-3} dependence. We attribute the spin relaxation to an admixture mechanism of hole mixing by magnetic fields and a hole-

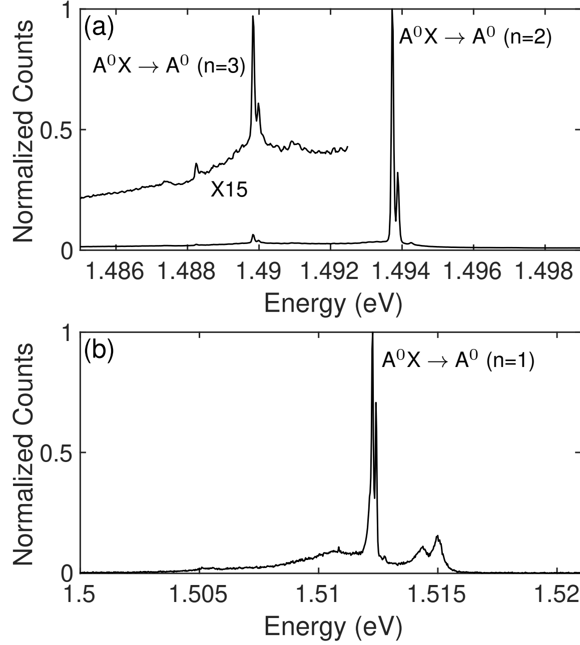

Figure 2.4: (a) Spectrum of the n=2 and n=3 THT transitions. The laser is resonantly on the main acceptor transition at 1.512 eV with 0.9 µW power. The temperature is at 2 K and the magnetic field is at 0 T. (b) The corresponding spectrum of the main acceptor lines. The laser is at 1.653 eV with 13 nW power. The laser has a spot size of ∼1 µm. The spectra are taken in the sample before ELO process.

phonon interaction through the deformation potentials. The detailed theory is discussed in Sec. 2.8. The calculation based on this theory matches the experimental result, as shown in Fig. 2.5(c). We note that the T_1 can be further increased by applying a larger biaxial strain. T_1 longer than 100 µs has been measured in self-assembled InGaAs QDs due to much larger HH-LH splittings than our system [30]. In our sample, 100 µs T_1 can be achieved by applying a strain greater than 0.4% (assuming the hole mixing factor does not change). This large strain could be achieved experimentally with piezoelectric actuator [33].

Below 5 T, T_1 is noticeably different at different locations on the sample and does not have a clear B-field dependence. A possible mechanism to explain this behavior is a combination of hole-hole interaction and inhomogeneous hyperfine fields, which is shown to be a mechanism for T_1 of donors at low fields [13]. This interaction depends on the local

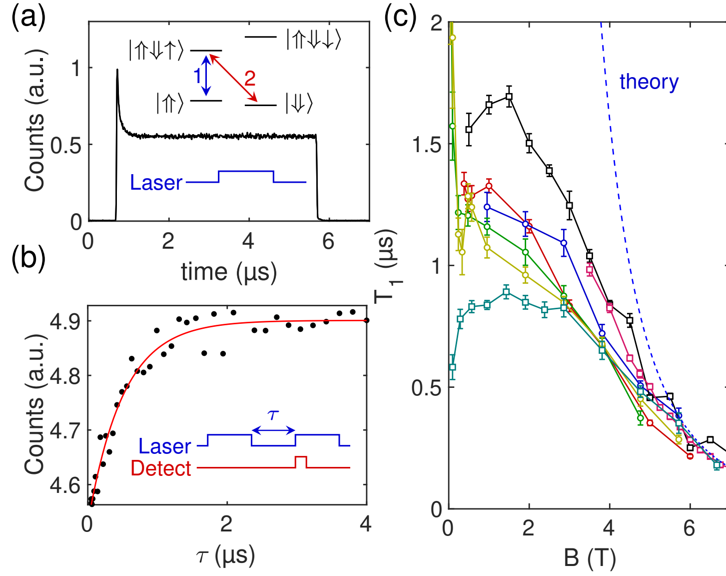

Figure 2.5: (a) An optical pumping curve at 1.5 K and 1.9 T. The inset shows the laser sequence. The laser is resonantly on transition 1 with 45 nW power and the PL from transition 2 is collected through a single photon counting module (SPCM). The laser spot diameter is ∼1 μm. The insets show the energy diagram and the laser sequence. The detection is on all the time during the laser sequence. (b) A population recovery curve at 1.5 K and 1.9 T. The laser and detection are on the same transitions as **a**. A single exponential curve is used to fit for the T_1. $T_1 = 0.51 \pm 0.04$ μs for this data. The inset shows the laser sequence. The detection window is 0.8 μs. (c) T_1 as a function of the magnetic fields. Different colors represent different locations on the sample. The dashed line shows the curve from theoretical calculation.

environments, which can vary across the sample.

2.7 *Coherent population trapping and the spin decoherence time T_2^**

Next, we perform coherent population trapping (CPT) on the A^0-A^0X system to investigate the hole-spin coherence properties. As shown in Fig. 2.6(a), the A^0X state $|\Uparrow\Downarrow\uparrow\rangle$, together with the two A^0 states, $|\Uparrow\rangle$ and $|\Downarrow\rangle$, form a Λ-system. With a control laser driving the transition 1 ($|\Uparrow\rangle \leftrightarrow |\Uparrow\Downarrow\uparrow\rangle$) and a probe laser driving the transition 2 ($|\Downarrow\rangle \leftrightarrow |\Uparrow\Downarrow\uparrow\rangle$), a destructive interference occurs when the energy difference between the two lasers equals the hole Zeeman splitting. On two-laser resonance, the system is pumped into a dark state, i.e. a superposition state between $|\Uparrow\rangle$ and $|\Downarrow\rangle$.

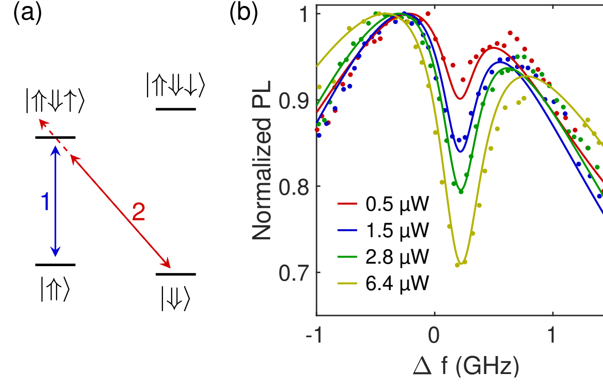

Figure 2.6: (a) Energy diagram of the CPT experiment. The control laser is fixed at transition 1 and the probe laser is scanned across transition 2. (b) CPT with different probe laser power. Each curve is a two-laser PLE spectrum where Δf is the detuning of the probe laser compared to the energy of transition 2. The solid curves are from a simultaneous fit of the data at all different probe laser powers using the 3-level density matrix model. The control laser is fixed at transition 1 with 3 µW. The polarization of both lasers are set at 45 degrees. The laser spot diameter is ∼1 µm. The temperature is 1.5 K and the magnetic field is 7 T. We note that we have used background subtraction on all CPT curves where we use the signal at large Δf as the background.

In our experiment, CPT is revealed by the two-laser PLE spectrum. The energy of the control laser is fixed near the resonance of transition 1 and the probe laser is scanned across the transition 2. A dip in the PLE spectrum occurs when the probe laser is on resonance with transition 2, as shown in Fig. 2.6(b). The linewidth and depth of the dip depend on the laser powers, the spontaneous emission rate of the $|\Uparrow\Downarrow\uparrow\rangle$ state, and the dephasing rate between $|\Uparrow\rangle$ and $|\Downarrow\rangle$. The CPT phenomenon is simulated by solving the master equation of a 3-level density matrix considering all relaxation and dephasing terms.

In the master equation $\partial\rho/\partial t = -i[H,\rho] + L(\rho)$, H is the Hamiltonian of the system

$$H_i = -\hbar \begin{pmatrix} \Delta_c & 0 & \Omega_c/2 \\ 0 & \Delta_p & \Omega_p/2 \\ \Omega_c^*/2 & \Omega_p^*/2 & 0 \end{pmatrix} \begin{matrix} |\Uparrow\rangle \\ |\Downarrow\rangle \\ |\Uparrow\Downarrow\uparrow\rangle \end{matrix} , \tag{2.4}$$

where Δ_c (Δ_p) and Ω_c (Ω_c) are the detuning and strength of the control (probe) laser, as

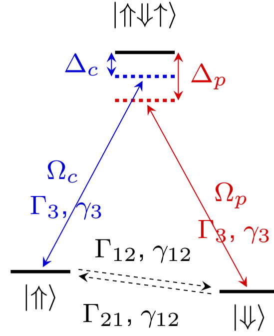

Figure 2.7: Energy diagram of the Λ-system.

shown in Fig. 2.7. L is the Linblad operator including the relaxation and dephasing between different states

$$L = \begin{pmatrix} -\Gamma_{12}\rho_{11} + \Gamma_{21}\rho_{22} + \Gamma_3\rho_{33} & -(\frac{\Gamma_{12}+\Gamma_{21}}{2} + \gamma_{12})\rho_{12} & -(\frac{\Gamma_{12}+2\Gamma_3}{2} + \gamma_3)\rho_{13} \\ -(\frac{\Gamma_{12}+\Gamma_{21}}{2} + \gamma_{12})\rho_{21} & \Gamma_{12}\rho_{11} - \Gamma_{21}\rho_{22} + \Gamma_3\rho_{33} & -(\frac{\Gamma_{21}+2\Gamma_3}{2} + \gamma_{s3})\rho_{23} \\ -(\frac{\Gamma_{12}+2\Gamma_3}{2} + \gamma_3)\rho_{31} & -(\frac{\Gamma_{21}+2\Gamma_3}{2} + \gamma_3)\rho_{32} & -2\Gamma_3\rho_{33} \end{pmatrix}. \tag{2.5}$$

Γ_{12} and Γ_{21} are the spin relaxation rates between $|\Uparrow\rangle$ and $|\Downarrow\rangle$. The spin relaxation time T_1 satisfies

$$\Gamma_{12} = \frac{1}{\mathrm{T}_1} \cdot \frac{1}{1 + e^{-g\mu_B B/k_b T}}, \tag{2.6}$$

$$\Gamma_{21} = \frac{1}{\mathrm{T}_1} \cdot \frac{e^{-g\mu_B B/k_b T}}{1 + e^{-g\mu_B B/k_b T}}, \tag{2.7}$$

where $g\mu_B B$ is the hole Zeeman splitting and $k_b T$ is the thermo energy. $\gamma_{12} = 1/\mathrm{T}_2$ is the dephasing rate between $|\Uparrow\rangle$ and $|\Downarrow\rangle$. Γ_3 and γ_3 are the spin relaxation rate and dephasing rate between the excited state $|\Uparrow\Downarrow\uparrow\rangle$ and the ground spin states, respectively. For simplicity, we assume they are the same for $|\Uparrow\rangle$ and $|\Downarrow\rangle$. The population of the excited state ρ_{33} after equilibrium is calculated as the final result, which is proportional to the detected PL intensity in the two-laser PLE experiment.

In Fig. 2.6, the CPT curves at different probe powers are simultaneously fit with the density matrix model. The fit parameters are listed in Table 2.2 (the “no broadening” column). The dephasing rate between the two spin states is found to be 0.15 ± 0.02 GHz, corresponding to an inhomogeneous dephasing time T_2^* of 6.8 ± 0.7 ns. The measured T_2^* in our sample is significantly smaller than the >100 ns T_2^* measured in single III-V QDs [21, 22].

We note that the small measured T_2^* is not due to the g-factor broadening caused by possible inhomogeneous strain in our sample. From a strain-dependent g-factor measurements of hole spins in InGaAs/GaAs QDs [37], the change of the in-plane g-factor with strain is small. Based on this reference and the linewidth of PLE spectrum in Fig. 2.2(c), an upper-limit estimation of the g-factor broadening is $\sim 8\times10^{-5}$ in our sample. Including this broadening in the density matrix model, there is no change of the fitted value of T_2^*, as shown in Table 2.2. The broadening is included by assuming a Gaussian distribution of Δ_c in the model:

$$\rho_{33} = \int \rho_{33}(\Delta_c)p(\Delta_c)\, d\Delta_c, \tag{2.8}$$

where $p(\Delta_c)$ is a Gaussian distribution of Δ_c with a center value Δ_{c0} and a standard deviation Δ_{inhomo}. With a g-factor broadening of 8×10^{-5}, $\Delta_c = 0.003$ GHz.

parameter	no broadening	with broadening
T_2^* (ns)	6.8 ± 0.7	6.8 ± 0.7
T_1 (µs)	0.09 ± 0.01	0.10 ± 0.01
Γ_3 (GHz)	0.63 ± 0.03	0.63 ± 0.03
γ_3 (GHz)	0.64 ± 0.05	0.64 ± 0.05
Ω^2/power (GHz^2/µW)	0.046 ± 0.004	0.046 ± 0.004
Δ_{c0} (GHz)	0.215 ± 0.009	0.215 ± 0.009
Δ_{inhomo} (GHz)	NA	0.003

Table 2.2: Fitting parameters for the 3-level density matrix model without and with broadening. The errors are 2σ errrors from fitting.

A possible mechanism for the short T_2^* is the HH-LH mixing [38, 39]. Even though the contact term in the hyperfine interaction is zero for hole spins, the long-range dipole-dipole term can still cause spin dephasing. This term has an Ising form for HH states so it

does not have an effect on dephasing in an in-plane external magnetic field. However, the hyperfine interaction for LH states does not have an Ising-form so it can still contribute to the dephasing significantly. We assume the HH states are mixed with LH states by a small mixing factor β:

$$|\pm 3/2\rangle = |\pm 3/2\rangle \pm \beta|\mp 1/2\rangle \tag{2.9}$$

The detailed theory is discussed in Sec. 2.9. With a mixing factor of $|\beta| = 0.047$, the theoretical results of T_2^* matches with the measured value of 6.8 ns. We attribute the hole mixing due to a nonzero shear strain ε_{xy}. The $|\beta| = 0.047$ corresponds to a $|\varepsilon_{xy}|$ of 0.004%. This weak shear strain can originate from the imperfect bonding between the GaAs epilayer and the MgO substrate. The mixing factor extracted here is consistent with the value extracted from the T_1 theory in Sec. 2.8 which gives $\beta = 0.03$.

2.8 *Theory of the longitudinal spin relaxation time* T_1

Due to the spin-orbit interaction described by the Luttinger-Kohn Hamiltonian, the ground states of holes bound to an acceptor are modified by higher orbital states. In a spherical model [40], the ground states of the holes are

$$\begin{aligned}
|\pm\frac{3}{2}'\rangle &= f(r)Y_0^0(\theta,\phi)|\pm\frac{3}{2}\rangle + \sqrt{\frac{1}{5}}g(r)Y_2^0(\theta,\phi)|\pm\frac{3}{2}\rangle \\
&- \sqrt{\frac{2}{5}}g(r)Y_2^{\pm 1}(\theta,\phi)|\pm\frac{1}{2}\rangle + \sqrt{\frac{2}{5}}g(r)Y_2^{\pm 2}(\theta,\phi)|\mp\frac{1}{2}\rangle, \\
|\pm\frac{1}{2}'\rangle &= f(r)Y_0^0(\theta,\phi)|\pm\frac{1}{2}\rangle - \sqrt{\frac{1}{5}}g(r)Y_2^0(\theta,\phi)|\pm\frac{1}{2}\rangle \\
&+ \sqrt{\frac{2}{5}}g(r)Y_2^{\mp 1}(\theta,\phi)|\pm\frac{3}{2}\rangle + \sqrt{\frac{2}{5}}g(r)Y_2^{\pm 2}(\theta,\phi)|\mp\frac{3}{2}\rangle,
\end{aligned} \tag{2.10}$$

where $Y_n^m(\theta,\phi)$ is the spherical harmonic function, $f(r)$ and $g(r)$ are the radial parts of the envelope functions.

For a Hamiltonian H in the basis of $|\pm 3/2\rangle$, $|\pm 1/2\rangle$, it can always be written in a general

form:

$$H = \begin{pmatrix} H_{11} & H_{12} & H_{13} & H_{14} \\ H_{12}^* & H_{22} & H_{23} & H_{24} \\ H_{13}^* & H_{23}^* & H_{33} & H_{34} \\ H_{14}^* & H_{24}^* & H_{34}^* & H_{44} \end{pmatrix}. \tag{2.11}$$

In the basis of $|\pm 3/2'\rangle$, $|\pm 1/2'\rangle$, if there are no terms related to the spatial or momentum operators in the Hamiltonian, it follows this change:

$$\begin{cases} H_{11} \to H_{11}(I_{ff} + \frac{1}{5}I_{gg}) + H_{22}\frac{2}{5}I_{gg} + H_{33}\frac{2}{5}I_{gg} \\ H_{22} \to H_{22}(I_{ff} + \frac{1}{5}I_{gg}) + H_{11}\frac{2}{5}I_{gg} + H_{44}\frac{2}{5}I_{gg} \\ H_{33} \to H_{33}(I_{ff} + \frac{1}{5}I_{gg}) + H_{11}\frac{2}{5}I_{gg} + H_{44}\frac{2}{5}I_{gg} \\ H_{44} \to H_{44}(I_{ff} + \frac{1}{5}I_{gg}) + H_{22}\frac{2}{5}I_{gg} + H_{33}\frac{2}{5}I_{gg} \\ H_{12} \to H_{12}(I_{ff} - \frac{1}{5}I_{gg}) + H_{34}\frac{2}{5}I_{gg} \\ H_{13} \to H_{13}(I_{ff} - \frac{1}{5}I_{gg}) - H_{24}\frac{2}{5}I_{gg} \\ H_{24} \to H_{24}(I_{ff} - \frac{1}{5}I_{gg}) - H_{13}\frac{2}{5}I_{gg} \\ H_{34} \to H_{34}(I_{ff} - \frac{1}{5}I_{gg}) + H_{12}\frac{2}{5}I_{gg} \\ H_{14} \to H_{14}(I_{ff} + \frac{1}{5}I_{gg}) \\ H_{23} \to H_{23}(I_{ff} + \frac{1}{5}I_{gg}) \end{cases} \tag{2.12}$$

where $I_{ff} = \int_0^\infty f^2(r)r^2dr$ and $I_{gg} = \int_0^\infty g^2(r)r^2dr$. We directly use $f(r)$ and $g(r)$ calculated from Ref. [40]. $f(r)$ can be approximately fit by function $\frac{a}{a_0^3}e^{-br/a_0}$ with $a = 9.241$, $b = 3.075$ and $a_0 = 5$ nm. $g(r)$ can be approximately fit by function $\frac{c\,r}{a_0^4}e^{-dr/a_0}$, with $c = 6.978$ and $d = 2.677$. Using these functions, I_{ff} is estimated to be 0.73 and I_{gg} is estimated to be 0.27. As I_{gg} is small compared to I_{ff} and it does not change the form of the Hamiltonian, I_{gg} terms are ignored in all calculations for simplicity.

In this basis, the system can be described by the following Hamiltonian

$$H = H_0 + H_B + H_{\varepsilon_{xy}} + H_{\text{ph}}. \tag{2.13}$$

H_B is due to the Zeeman effect in the Voigt geometry ($\mathbf{B}\perp\hat{z}$):

$$H_B = I_{ff} g_0 \mu_B B J_x \tag{2.14}$$

where J_x is the 3/2 spin operator, and g_0 is the hole g-factor. The term $I_{ff} = \int_0^\infty f^2(r) r^2 dr$ is the modification factor of the Hamiltonian in the new basis.

H_0, $H_{\varepsilon_{xy}}$ and H_{ph} are all calculated from the Bir-Pikus Hamiltonian due to strain [34]:

$$H_{\text{BP}} = \begin{pmatrix} P+Q & -S & R & 0 \\ -S^\dagger & P-Q & 0 & R \\ R^\dagger & 0 & P-Q & S \\ 0 & R^\dagger & S^\dagger & P+Q \end{pmatrix} \begin{matrix} |3/2\rangle \\ |1/2\rangle \\ |-1/2\rangle \\ |-3/2\rangle \end{matrix}, \tag{2.15}$$

$$\begin{cases} P = a_v(\varepsilon_{xx} + \varepsilon_{yy} + \varepsilon_{zz}) \\ Q = \dfrac{b}{2}(\varepsilon_{xx} + \varepsilon_{yy} - 2\varepsilon_{zz}) \\ R = -\dfrac{\sqrt{3}}{2} b(\varepsilon_{xx} - \varepsilon_{yy}) + id\varepsilon_{xy} \\ S = d(\varepsilon_{xz} - i\varepsilon_{yz}) \end{cases} \tag{2.16}$$

The values of the deformation potential constants are $a_v = 1.16$ eV, $b = -1.7$ eV, and $d = -4.55$ eV [34]. H_{BP} is in the basis of $|\pm 3/2\rangle$, $|\pm 1/2\rangle$. To change to the basis of $|\pm 3/2'\rangle$, $|\pm 1/2'\rangle$ in Eq. 2.10, the Hamiltonian needs to be mutiplied by a factor of I_{ff}.

H_0 is due to the applied biaxial strain in the sample.

$$H_0 = \begin{pmatrix} \Delta & 0 & 0 & 0 \\ 0 & 0 & 0 & 0 \\ 0 & 0 & 0 & 0 \\ 0 & 0 & 0 & \Delta \end{pmatrix} \begin{matrix} |3/2'\rangle \\ |1/2'\rangle \\ |-1/2'\rangle \\ |-3/2'\rangle \end{matrix}, \tag{2.17}$$

where Δ is the HH-LH splitting. $H_{\varepsilon_{xy}}$ describes the components from the weak shear strain ε_{xy}. The strain ε_{xy} is attributed to imperfect bonding between the GaAs epitaxial layer

and the MgO substrate.

$$H_{\varepsilon_{xy}} = \begin{pmatrix} 0 & 0 & iI_{ff}d\varepsilon_{xy} & 0 \\ 0 & 0 & 0 & iI_{ff}d\varepsilon_{xy} \\ -iI_{ff}d\varepsilon_{xy} & 0 & 0 & 0 \\ 0 & -iI_{ff}d\varepsilon_{xy} & 0 & 0 \end{pmatrix}, \tag{2.18}$$

where d is the deformation potential constant. H_{ph} describes the hole-phonon interaction. It has the same format as the Bir-Pikus Hamiltonian but the strain ε_{ij} is replaced by the strain tensor introduced by phonon [41]:

$$\varepsilon_{i,j}^{\mathrm{ph}} = \frac{i}{2}\sqrt{\frac{\hbar}{2\rho\omega}}(q_i\eta_j + q_j\eta_i)e^{i\mathbf{q}\cdot\mathbf{r}}, \tag{2.19}$$

where ρ is the mass density, $\mathbf{q}$ is the phonon wave vector, ω is the phonon frequency, and $\boldsymbol{\eta}$ is the phonon polarization. For LA phonon, $\boldsymbol{\eta} = (q_x, q_y, q_z)/q$. For TA phonon, there are two modes: $\boldsymbol{\eta_1} = (q_y, -q_x, 0)/q_\perp$ and $\boldsymbol{\eta_2} = (q_xq_z, q_yq_z, -q_\perp^2)/qq_\perp$, where $q_\perp = \sqrt{q_x^2 + q_y^2}$. $H_{\varepsilon_{xy}}$, H_B and H_{ph} are all small compared to H_0 and are treated perturbatively.

With the two terms $H_0 + H_B$ in the Hamiltonian, the eigenstates of the HH change to

$$|3/2''\rangle = |3/2'\rangle + I_{ff}\tfrac{\sqrt{3}g_0\mu_B B}{2\Delta}\,|1/2'\rangle\,, \tag{2.20}$$

$$|-3/2''\rangle = |-3/2'\rangle + I_{ff}\tfrac{\sqrt{3}g_0\mu_B B}{2\Delta}\,|-1/2'\rangle\,, \tag{2.21}$$

In the HH subspace, $H_{\varepsilon_{xy}}$ changes to

$$H_{\varepsilon_{xy}}^{HH} = -I_{ff}\beta\sqrt{3}g_0\mu_B B \begin{pmatrix} 0 & -i \\ i & 0 \end{pmatrix} \begin{matrix} |3/2''\rangle \\ |-3/2''\rangle \end{matrix}, \tag{2.22}$$

where $\beta = I_{ff}d\varepsilon_{xy}/\Delta$ is the hole mixing factor due to the shear strain ε_{xy}. Equation 2.22 corresponds to an in-plane HH g-factor of

$$|g_{HH}^{\perp}| = 2\sqrt{3}I_{ff}\beta g_0, \tag{2.23}$$

and the in-plane HH eigen-states are

$$|3/2^{\perp}\rangle = \tfrac{1}{\sqrt{2}}(|3/2''\rangle + i\,|{-3/2''}\rangle), \tag{2.24}$$

$$|{-3/2^{\perp}}\rangle = \tfrac{1}{\sqrt{2}}(|3/2''\rangle - i\,|{-3/2''}\rangle). \tag{2.25}$$

The spin relaxation rate between the two HH states is calculated using the Fermi's golden rule:

$$\Gamma = \frac{1}{(2\pi)^2\hbar}\sum_{\alpha}\int d^3q|M|^2\delta(\hbar q s_{\alpha} - |g_{HH}^{\perp}|\mu_B B) \tag{2.26}$$

where α denotes different phonon modes, s_α is the sound speed of mode α, and $|g_{HH}^{\perp}|\mu_B B$ is the in-plane Zeeman splitting. M is the matrix element of H_{ph} between the two HH states:

$$\begin{aligned} M &= \langle -3/2^{\perp}|H_{ph}|3/2^{\perp}\rangle \\ &= \frac{I_{ff}g_{HH}^{\perp}\mu_B B}{4\beta\Delta}\sqrt{\frac{\hbar}{2\rho\omega}}\cdot[\,d(q_x\eta_z + q_z\eta_x)i\sqrt{3}b(q_x\eta_x - q_y\eta_y)], \end{aligned} \tag{2.27}$$

where we have used the approximation $e^{i\mathbf{q}\cdot\mathbf{r}} \simeq 1$ as $\mathbf{q}\cdot\mathbf{r}$ is small. The spin relaxation rate Γ is

$$\Gamma = \frac{1}{240\pi}(\frac{I_{ff}}{\beta\Delta})^2\frac{(|g_{HH}^{\perp}|\mu_B B)^5}{\rho\hbar^4}(3b^2 + d^2)(\frac{2}{3s_l^5} + \frac{1}{s_t^2}), \tag{2.28}$$

and the measured spin relaxation time T_1 is $1/\Gamma$ multiplied by the phonon factor $1/F_{\text{ph}}$ [13]:

$$T_1 = \frac{1}{\Gamma F_{\text{ph}}} = \frac{1}{\Gamma}(\frac{2}{e^{|g_{HH}^{\perp}|\mu_B B/k_B T} - 1} + 1)^{-1}. \tag{2.29}$$

where $k_B T$ is the thermal energy. The values of the parameters used to calculate T_1 are listed in Table 2.3. With a mixing factor $\beta = 0.03$, we find theoretical T_1 curve agrees well with the measured data at high fields, shown in Fig. 2.5(c). Using the measured value of $g_{HH}^{\perp} = 0.155$, this mixing factor corresponds to a hole g-factor of g_0=2.04. This agrees with the values from previous literatures which have reported hole g-factors ranging from 0.52 to 2.34 [42, 43, 44].

ρ (kg/m^3)	s_l (m/s)	s_t (m/s)	b (eV)
5.32×10^3[13]	4.73×10^3[13]	3.35×10^3[13]	-1.7[34]

d (eV)	Δ (meV)	I_{ff}	$\lvert g_{HH}^{\perp}\rvert$
-4.55 [34]	2.0	0.73	0.155

Table 2.3: Parameters used to calculate T$_1$. Parameters Δ and $|g_{HH}^{\perp}|$ are determined from experiments.

2.9 Theory of the inhomogeneous dephasing time T_2^*

The spin dephasing originates from the dipole-dipole inhomogeneous hyperfine fields between the hole spins and the nearby nuclear spins in the crystal. The Hamiltonian of this hyperfine interaction between the hole and a nucleus is

$$H_I = \frac{C_j}{2}\Omega f^2(r) \cdot \begin{pmatrix} I_z & \frac{I_x - iI_y}{\sqrt{3}} & 0 & 0 \\ \frac{I_x + iI_y}{\sqrt{3}} & \frac{I_z}{3} & -\frac{2}{3}(I_x - iI_y) & 0 \\ 0 & -\frac{2}{3}(I_x + iI_y) & -\frac{I_z}{3} & \frac{I_x - iI_y}{\sqrt{3}} \\ 0 & 0 & \frac{I_x + iI_y}{\sqrt{3}} & -I_z \end{pmatrix}, \tag{2.30}$$

where C_j is the hyperfine constant ($C_{Ga} = 3$ µeV, $C_{As} = 4.4$ µeV) [38], I_i ($i = x, y, z$) is the nuclear spin operator, r is the position of the nucleus, and Ω is the unit cell volume. For pure HH spin, the Hamiltonian in the HH subbands has an Ising form, i.e. $H_I^{HH} \propto I_z \cdot \sigma_z$. In the Voigt geometry ($\mathbf{B} \perp \hat{z}$), as the hole spin is in the in-plane direction, the hyperfine interaction does not contribute to the spin dephasing thus the T$_2^*$ should be much longer than nanoseconds. However, in our sample, due to the existence of the shear strain ε_{xy}, the HH is mixed with LH:

$$|3/2^*\rangle = |3/2'\rangle - i\beta\,|-1/2'\rangle\,, \tag{2.31}$$

$$|-3/2^*\rangle = |-3/2'\rangle + i\beta\,|1/2'\rangle\,, \tag{2.32}$$

where $\beta = I_{ff} d\varepsilon_{xy}/\Delta$ is the mixing factor. In this new basis, H_I in the HH subband changes to

$$H_I^{HH} = \frac{C_j}{2}\Omega f^2(r) \cdot (I_z \cdot \sigma_z + \frac{2\beta}{\sqrt{3}} I_y \cdot \sigma_x - \frac{2\beta}{\sqrt{3}} I_x \cdot \sigma_y). \tag{2.33}$$

Utilizing the same method in Ref. [45], T_2^* is calculated to be

$$\frac{\hbar}{T_2^*} = \frac{2|\beta|}{\sqrt{3}} \sqrt{\frac{2(\int_0^\infty f^4(r) r^2 dr)\Omega \sum_j I_j(I_j+1)(C_j)^2}{3}}, \tag{2.34}$$

where the summation is over all nuclei in a unit cell. The measured 6.8 ns T_2^* corresponds to a mixing factor $|\beta| = 0.047$. This is similar to the 0.03 mixing factor estimated from T_1 measurements in Sec. 2.8. The consistency of the mixing factor extracted from the two independent measurements supports that the HH-LH mixing is the limiting factor of both T_1 and T_2^* in this system.

2.10 Conclusion

We have introduced compressive strains into a p-type GaAs epitaxial layer through the ELO technique. This strain breaks the degeneracy of HH and LH, leading to µs-scale T_1. CPT measurements show a 6.8 ns T_2^* in this strained sample. We attribute this short T_2^* to an effect of HH-LH mixing. We have established a theoretical framework to calculate both T_1 and T_2^* quantitatively based on the mechanisms of hole-phonon interaction and dipole-dipole hyperfine interaction mediated by HH-LH mixing. We find good agreements between this theoretical calculation and our experimental results. Other strain engineering techniques such as wafer bonding [32] or using a piezoelectric actuator [33] could be utilized in the future to provide stronger and more homogeneous strain in the sample, which can potentially enhance both T_1 and T_2^* [46].

Chapter 3

LONGITUDINAL SPIN RELAXATION OF DONORS IN GAAS, INP, AND CDTE

3.1 Introduction

In the last chapter, we show our study of acceptors in strained GaAs but only find µs-scale T_1 and a 6.8 ns T_2^*. While it is possible to enhance the coherence time with other strain engineering techniques, the current performance suggests that a more promising path is to return to the electron donor system in direct band gap materials. In this chapter, we perform a study of the longitudinal spin relaxation time of donors in three different materials: GaAs, InP, and CdTe.

In the last decade, the prospects for spin-based quantum information have spurred renewed interest in the fundamental mechanisms for spin relaxation in semiconductors [47, 48, 49, 50]. Shallow impurities in direct-bandgap materials are promising candidates for quantum applications relying on spin-photon interfaces [51, 52, 53], as these systems boast high optical homogeneity [54], strong spin-photon coupling, and the potential in II-VI materials [55] to enhance spin coherence times with isotope purification [56, 57]. While electron spin relaxation is now relatively well understood in III-V semiconductor quantum dots both theoretically and experimentally [50, 58, 59, 60, 61, 62, 63], it is still an open question whether the same processes dominate in the similar direct band-gap donor system. In contrast to quantum dots, in which the size, shape, composition, and strain field for each dot are to a large extent unknown, the physical properties relevant to spin relaxation for the homogeneous donor system have been measured. This enables quantitative comparison of spin-relaxation rates between theory and experiment which should help predict which donor systems are most promising for future applications.

Here we measure the longitudinal spin-flip time T_1, the fundamental limit for the storage

This chapter is a slightly modified version of a published paper written by the author of this thesis [13].

time for quantum information, in three semiconductors: GaAs, InP, and CdTe. All three are direct bandgap materials with similar band structure allowing for the optical pumping of the donor-bound electron spins under resonant exciton excitation. We show that at low magnetic fields, T_1 is proportional to B^2 with a proportionality constant highly dependent on temperature and donor density. At high magnetic fields, we find that T_1 is proportional to $B^{-\nu}$, with the power ν in the range $3 \lesssim \nu \lesssim 4$. The competition of these two dependencies leads to a maximum of T_1 in GaAs and InP at relatively high magnetic field: (1.4 ± 0.1) ms at 4 T for GaAs and (0.40 ± 0.01) ms at 1.9 T for InP. Due to technical issues, we are unable to observe this maximum for CdTe; however, the highest T_1 measured is (1.23 ± 0.07) ms at 1.1 T with T_1 expected to rapidly increase at lower fields.

The low magnetic-field T_1 behavior for GaAs and InP is consistent with a spin relaxation mechanism controlled by the hyperfine coupling of the electron spin with static fluctuations of the host-lattice nuclear spins. In this situation, spin precession is randomized due to the finite electron correlation time at each donor site [64, 65]. Although the mechanism for the extremely-short correlation time τ_c ($\tau_{c,\mathrm{GaAs}} \simeq 25$ ns, $\tau_{c,\mathrm{InP}} \simeq 40$ ns) is not completely clear, our measurement is consistent with prior works [65, 66]. Our results show that the nuclear-spin environment, known to be the dominant factor in spin dephasing [58, 48], plays an important role in longitudinal relaxation even at low doping densities ($\sim 10^{14}$ cm^{-3}) and moderate magnetic fields (up to several tesla).

On the high-field side, the similar magnetic-field dependence observed in all three semiconductors is suggestive of a universal mechanism. We theoretically investigate the dominant spin-relaxation mechanisms and find that two mechanisms, (i) the direct spin-phonon interaction and, (ii) the admixture mechanism caused by Dresselhaus spin-orbit coupling combined with the piezoelectric electron-phonon interaction, can account for the magnitude of the observed relaxation in GaAs and CdTe. The strength of the direct spin-phonon interaction is surprising because it was found to be negligible compared to the admixture mechanism in the similar quantum dot system [50]. The relative weakness of the admixture mechanism is related with the symmetry of the system. This is most clearly seen in the limit of small magnetic fields where the donor-bound electron confinement potential is spherically symmetric. The Dresselhaus spin-orbit interaction, which couples the spin-up

and spin-down states in the admixture mechanism, results in a weak coupling between the ground orbital state with states of high angular momentum. In contrast, quantum dots exhibit strong axial confinement, resulting in a relatively strong coupling to the nearest excited state. At high field, the external magnetic field partially reduces the symmetry of the donor confinement potential, enhancing the admixture mechanism. However, the coupling is still typically much weaker than it is in quantum dots. We find, however, that both the direct spin-phonon interaction and the admixture mechanism are too weak to account for the observed relaxation in InP.

3.2 Samples and experimental technique

We study two GaAs, three InP, and two CdTe n-doped samples with the parameters given in Table 3.1. Spin-relaxation is measured optically in the Voigt geometry (photon wave vector $\mathbf{k} \perp \mathbf{B}$) with the magnetic field aligned parallel to the sample surface. Magneto-photoluminescene spectra exhibiting optically resolved Zeeman transitions for all three semiconductors are shown in Sec. 3.3. Λ-transitions suitable for optically pumping the electron spin are found by resonantly exciting one of the Zeeman sublevels of the neutral donor (D^0) to the lowest neutral donor-bound exciton (D^0X) transition and observing the corresponding Raman transition. The optically excited and collected transitions for InP (GaAs, CdTe) are labelled in the energy diagram and photoluminescence spectra in Figs. 3.1(a),(b) [Sec. 3.4, Figs. 3.3(a),(b),(e),(f)].

To measure the spin relaxation time in the magnetic field, we optically deplete one of the Zeeman spin sublevels and monitor the recovery of its thermal population in the course of spin relaxation. At high magnetic fields, the optically-resolved spin Raman transitions enable frequency-selective optical pumping of the donor electron state. At low fields, while the transitions cannot be spectrally resolved, optical pumping is still obtained by utilizing the optical polarization selection rules. Optical pumping is confirmed by monitoring the time-dependence of the collected transition intensity during optical excitation after the system has reached thermal equilibrium. A typical high-field optical pumping pulse sequence and photoluminescence trace are depicted in Figs. 3.1(c),(d). The decrease in photoluminescence intensity is only observed with resonant spin excitation. Two-laser experiments in

Sample	N_e (cm^{-3})	ℓ (μm)	Growth Method
InP-1[67]	5.6 $\times 10^{13}$	5.1	MOCVD
InP-2[67]	2.3 $\times 10^{14}$	7.4	MOCVD
InP-3[67]	1.8 $\times 10^{15}$	4.2	MOCVD
GaAs-1[68]	3×10^{13}	15	MBE
GaAs-2	5×10^{13}	10	MBE
CdTe-1[69]	1×10^{14}	>1000	Bridgman
CdTe-2[70]	$> 10^{14}$	>1000	Bridgman

Table 3.1: Sample parameters. $N_e = N_D - N_A$ is the electron density, ℓ is the sample thickness. Metal organic vapour phase epitaxy and molecular beam epitaxy are abbreviated by MOCVD and MBE respectively. The InP epilayer is grown directly on an InP substrate. The GaAs epilayer is grown on 4 microns of $Al_{0.3}Ga_{0.7}As$ on a GaAs substrate. Further details on sample growth are given in the references.

GaAs have also confirmed that this decrease is due to spin-pumping and not, for example, due to photo-induced ionization [9]. A clear optical pumping signal cannot be observed in the highest purity InP sample, InP-1. The cause is attributed to surface depletion effects discussed further in Appendix A.1. For the remainder of the chapter we will restrict ourselves to the remaining six samples, where reliable signals are detected.

Spin-relaxation measurements are performed by varying the recovery time between optical pumping pulses which are produced by an acousto-optic modulator (AOM) from the output of a narrow-band continuous-wave Ti:Sapphire laser. The AOM extinction ratio, r_e was measured to be $>10^4$ giving an upper-bound of the maximum measurable T_1 of $r_e\tau_{op}$, in which τ_{op} is the characteristic timescale of optical pumping. Given the several microsecond τ_{op} [Fig. 3.1(d)], we have the ability to measure T_1 exceeding 10 ms. The "Raman" photoluminescence is collected during the first part of the optical pumping pulse, see Fig. 3.1(e). As the recovery time increases, we observe an increase in the collected signal as the system returns to thermal equilibrium. At each magnetic field, the recovery is fitted to a weighted exponential with time constant T_1 [71], as shown in Fig. 3.1(e). Measurements are performed for fields up to 7.0 T. Reduced visibility of the optical pumping signal places a technical limit on the minimum magnetic field measurement for each sample.

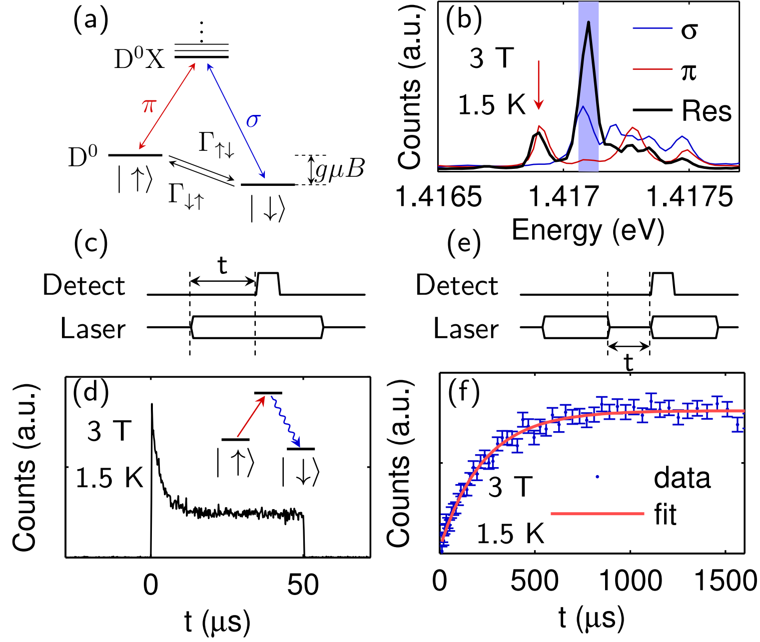

Figure 3.1: (a) Energy level diagram for the InP donor system. (b) Photoluminescence spectrum of InP. Excitation at 1.549 eV with 50 μW power, for the two above-bandgap excitation spectra (red and blue). σ (π) denote linear collection polarization perpendicular (parallel) to the magnetic field. Resonant excitation spectrum (black) uses excitation at 1.417 eV with 100 μW π-polarized light, with σ-polarized light collected. (c) Pulse sequence for optical pumping. The Ti:Sapphire laser is pulsed on and off repetitively on the π transition, while PL from the σ transition is detected. The time between pulses significantly exceeds T_1. (d) Optical pumping trace for InP with laser power 10 μW. The inset sketches the population transfer process during optical pumping. The amplitude of the exponential curve is proportional to the population in $\uparrow$. (e) Pulse sequence for T_1 measurement. The detector gate-on time is 2 μs and the laser pulse length is 50 μs. (f) T_1 measurement for InP with laser power 10 μW. The data is fit with an exponential plus a background yielding the time constant $T_1 = (0.23 \pm 0.1)$ ms. Error bars denote the standard deviation of the recovery signal in each time bin over the many repetitions of the pulse sequence. The corresponding representative data for GaAs and CdTe are given in Appendix 3.4. All experiments used $\sim$30 μm laser spot size.

3.3 Magneto-photoluminescence spectra for GaAs, InP, and CdTe

Representative magneto-photoluminescence spectra for GaAs-2, InP-2, and CdTe-2 are shown in Fig. 3.2. In all three samples we can observe the free exciton (labeled X), donor-bound exciton $D^0X \rightarrow D^0$,1s transition (labeled D^0X), ionized donor-bound exciton transition $D^+X \rightarrow D^+$ (labeled D^+X), and acceptor-bound exciton $A^0X \rightarrow A^0$,1s transition (labeled A^0X). Also observed in GaAs and InP are the D^0X two-electron satellite (TES) transitions which correspond to the $D^0X \rightarrow D^0, nl^m$ transition, where n, l, m specify the quantum numbers of the excited D^0 orbital at $B = 0$. For GaAs and InP, the fine-structure of the D^0X spectra is well resolved due to the hole spin and spin-orbit interaction as well as the nearby D^0X excited orbital states. In the CdTe samples, which are bulk crystals, this structure is unresolved, limiting our ability to optically pump the system to electron Zeeman splittings greater than 0.1 meV.

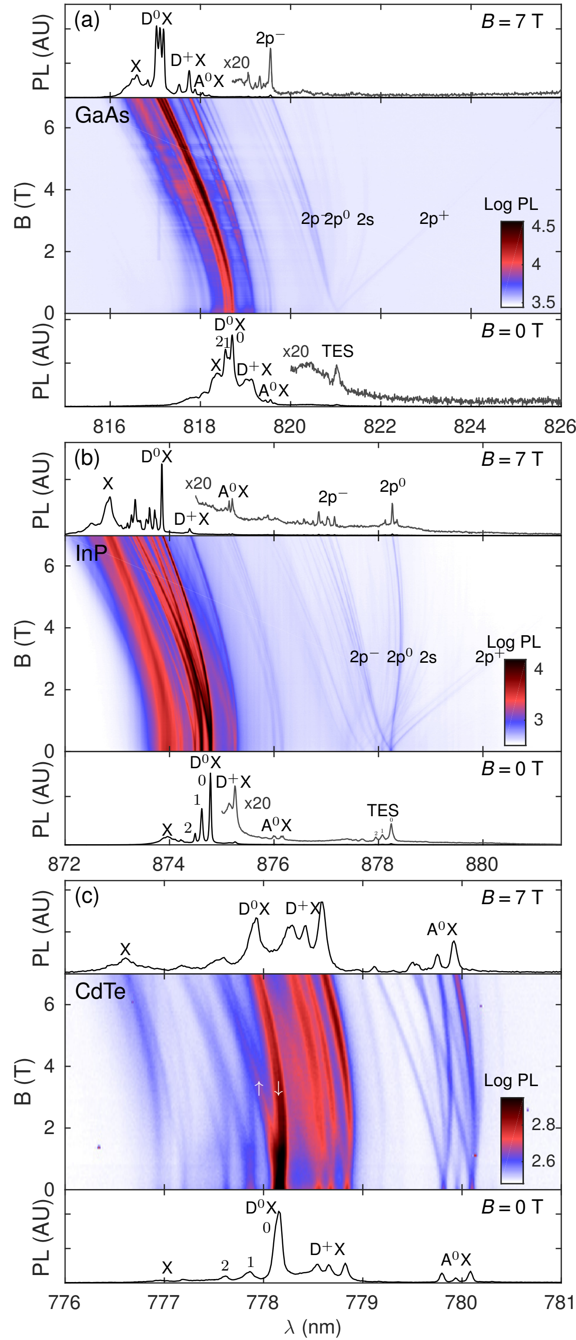

Figure 3.2: Magneto-photoluminescence spectra in the Voigt geometry. (a) GaAs-2. The oscillations in photoluminescence intensity with field are attributed to oscillations in magneto-absorption due to the diamagnetic exciton effect [72], $T = 2$ K, excitation and collection are performed in linear polarizations oriented at $\pm 45°$ with respect to the magnetic field direction, 1 mW excitation power at 810 nm. (b) InP-2, $T = 2.3$ K, σ-polarization excitation, all polarizations collected, 40 μW above band-gap excitation power. (c) CdTe-2. $T = 1.6$ K. π-polarization excitation, σ-polarization collection, 20 μW above band-gap excitation power.

3.4 GaAs and CdTe T_1 measurements

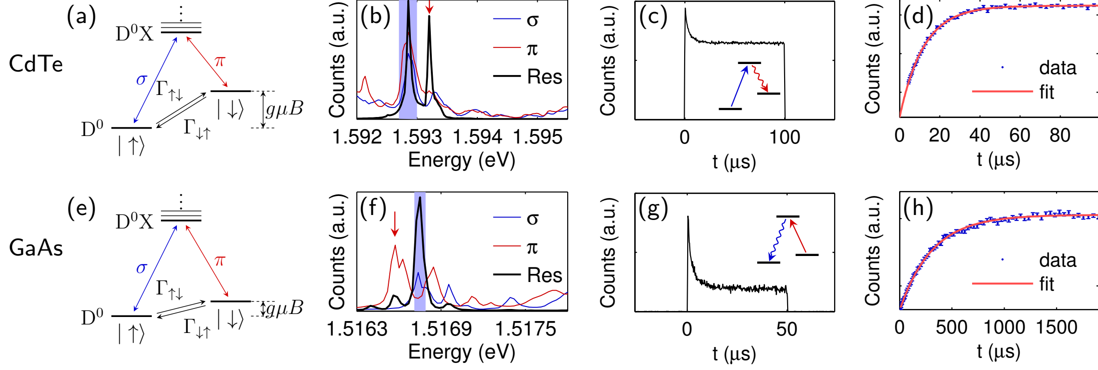

Figure 3.3: (a) Energy level diagram for donor system in CdTe. (b) Photoluminescence spectrum of CdTe at $B = 3.5$ T, $T = 1.5$ K. Excitation at 1.653 eV with 50 μW for the two above band spectra (red and blue). Excitation at 1.593 with 50 μW for resonant spectrum (black), as shown by the red arrow. (c) Optical pumping trace for CdTe at 3.5 T, 1.5 K. Power 50 μW. Laser pulse lasts 100 μs. (d) T_1 measurement for CdTe at 3.5 T, 1.5 K. Power 50 μW. $T_1 = (12.0 \pm 0.2)$ μs. (e) Energy level diagram for donor system in GaAs. (f) Photoluminescence spectrum of GaAs at 7 T, 1.5 K. Excitation at 1.530 eV with 18 μW for the two above band spectra (red and blue). Excitation at 1.517 with 10 μW for resonant spectrum (black), as shown by the red arrow. (g) Optical pumping trace for GaAs at 7 T, 1.5 K. Power 10 μW. Laser pulse lasts 50 μs. (d) T_1 measurement for GaAs at 7 T, 1.5 K. Power 10 μW. $T_1 = (313 \pm 5)$ μs. All data are taken with an excitation spot size ~ 30 μm.

Representative energy diagrams, spectra, optical pumping traces, and T_1 recovery traces for CdTe and GaAs are shown in Fig. 3.3. For GaAs and InP, the lower energy Zeeman pair transition was used for optical pumping. Although this results in a weaker signal due to the lower thermal population in the higher electron spin level, the lower energy transition is clearly resolved from all other D^0X transitions enabling efficient optical pumping. For CdTe, there is significant inhomogeneous optical broadening of the D^0X lines. This can be observed by comparing the non-resonant and resonant excitation spectral linewidths in Fig. 3.3(b). Optical pumping visibility is thus significantly smaller in this sample relative to GaAs and InP. Empirically we find the best signal-to-noise is obtained by pumping the high-energy Zeeman pair transition due to the significantly larger thermal population in the lower energy spin state. Due to the large g-factor in CdTe, the thermal population in the

high energy state at 7 T and 1.5 K is only 0.6%.

3.5 Experimental Results

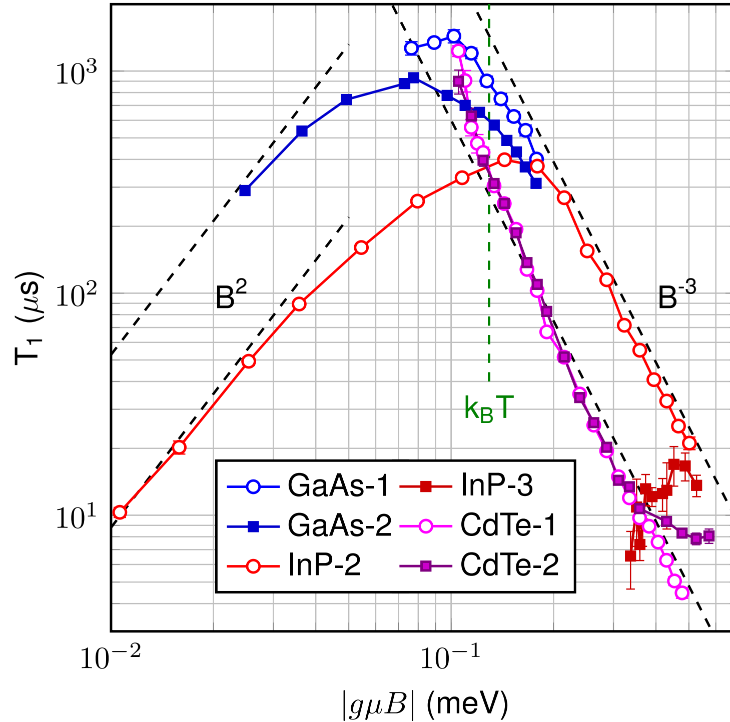

Figure 3.4: T_1 as a function of Zeeman splitting for the six different samples at 1.5 K. The absolute values of the electron g-factors used to convert from B to the Zeeman splitting for GaAs, InP and CdTe are 0.44, 1.3, and 1.65, respectively. Sample descriptions are given in Table 3.1. The black dashed lines in the high energy (low energy) side denote a B^{-3} (B^2) dependence for reference. They are offset from the experimental data for clarity. The green dashed line denotes the thermal energy $k_B T$ for reference.

The longitudinal spin relaxation times T_1 as a function of the electron Zeeman splitting $\Delta E = |g\mu B|$ for InP, GaAs and CdTe are shown in Fig 3.4. Here, g is the effective electron g-factor and μ is the Bohr magneton. The data show several notable features. First, all samples approach a $T_1 \sim B^{-\nu}$ dependence, with $3 \lesssim \nu \lesssim 4$, at high magnetic fields. The proportionality constant depends on the semiconductor sample. A B^{-3} dependence, included in Fig. 3.4, fits all curves well, however we note that higher-field data would be

desirable for GaAs because the small electron g-factor prevents us from accessing the high-Zeeman-splitting limit, where $|g\mu B| \gg k_B T$. Also, a B^{-4} power-law is reasonable for CdTe, as the magnetic field dependence becomes steeper in CdTe with decreasing field, see also Fig. 3.6. The high-field T_1 process appears to be independent of donor concentration. Even the T_1 curve for the high-density InP-2 sample approaches the InP-1 curve at the highest fields. At low fields, T_1 in InP and GaAs approaches a B^2 dependence with a donor-concentration-dependent pre-factor. This is extremely pronounced for the InP samples in which the donor-bound electron density N_e, the difference between the donor and acceptor densities in the sample, $N_D - N_A$, differs by a factor of 4. The effect is also present in GaAs in which N_e differs by a factor of 1.7. Finally, the maximum T_1 observed in all three

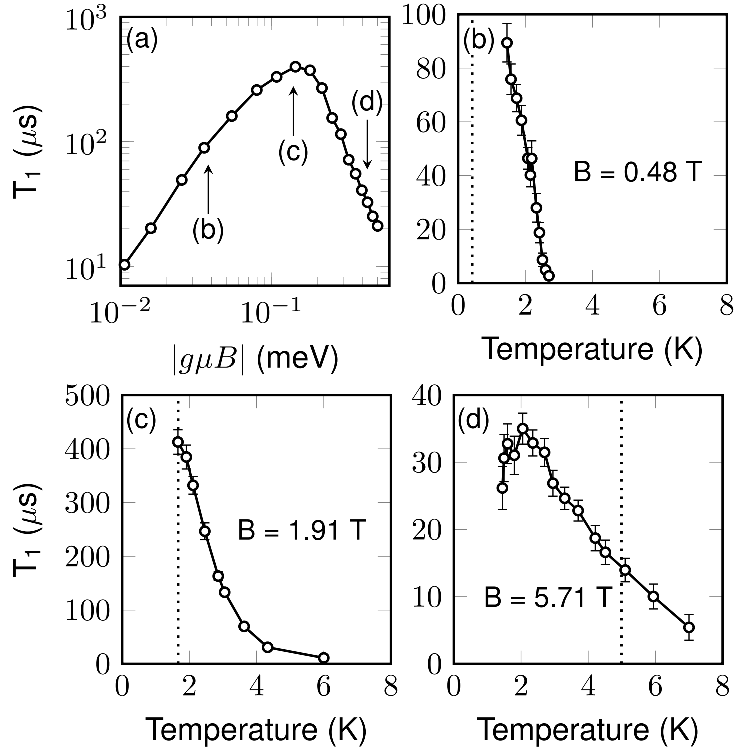

Figure 3.5: (a) T_1 as a function of the Zeeman splitting for InP-2 at 1.5 K. The arrows show the magnetic field values at which the temperature dependence study was performed. (b-d) Temperature dependence of T_1 at (b) $B = 0.48$ T, (c) 1.9 T, and (d) 5.7 T. The dotted line denotes $|g\mu B|/k_B$.

materials is similar: $T_1 = 1.4$, 0.4, and 1.2 ms for GaAs, InP, and CdTe respectively.

Measurements of the temperature T effect on T_1 are also performed. In InP-2, the sample in which T_1 can be obtained for the largest range of Zeeman energies, $T_1(T)$ was measured at 0.5 T (low field regime), 1.9 T (peak T_1), and 5.7 T (high-field regime) with the results depicted in Fig. 3.5. In the low-field regime, an extremely-steep inverse dependence of T_1 on temperature is observed indicative of a strong phonon-assisted process. In the high-field regime, the relaxation time is almost independent of temperature at the lowest temperatures in our experiments, and drops with an increase in T. This high-field behavior is consistent with a model in which T_1 is inversely dependent on the phonon factor $F_{ph} = 2N_{ph} + 1$, in which $N_{ph} = [\exp(|g\mu B|/k_B T) - 1]^{-1}$ is the phonon occupation number. A comparison of magnetic-field-dependent measurements at 1.5 K and 5 K for CdTe-1 also support a high-field single-phonon mechanism. The ratio of the two curves in Fig. 3.6 is given by $F_{ph}(5\text{ K})/F_{ph}(1.5\text{ K})$.

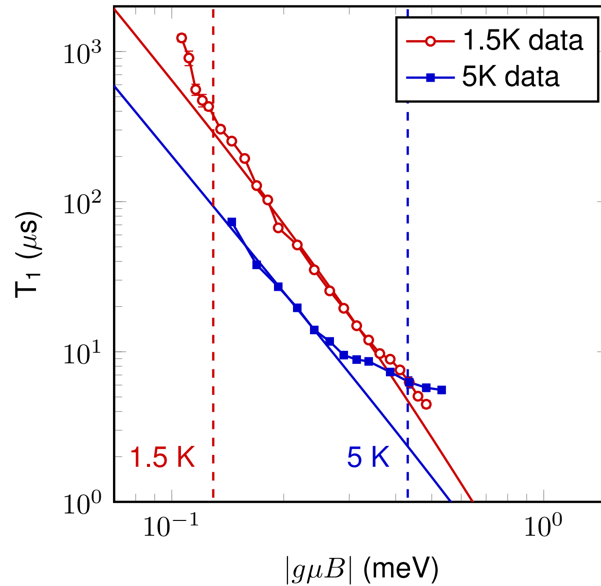

Figure 3.6: T_1 as a function of Zeeman splitting for CdTe-1 at $T = 1.5$ K and $T = 5$ K. The red and blue lines are mutually fitted by an empirical formula $T_1 = bB^4/F_{ph}$, where $b = 2000\ \mu s/\mathrm{T}^4$. The red and blue dashed lines denote the energy at 1.5 K and 5 K.

3.6 Theory

Here we consider the mechanisms resulting in spin relaxation of donor-bound electrons. We start with the limit of relatively-low magnetic fields, where spin relaxation is controlled by the hyperfine coupling of the electron and nuclear spins. Next, we turn to the regime of high enough magnetic fields where the nuclei-induced spin relaxation is unimportant and the spin-flip processes caused by the joint effects of the electron-phonon and the spin-orbit interactions play the major role.

3.6.1 Low-field spin-relaxation

At low temperatures and low donor densities, the electrons in bulk semiconductors are localized. At low and moderate magnetic fields, the electron spin relaxation is controlled by the hyperfine interaction with the host lattice nuclei [64, 73]. The spin dynamics of the electron in the ensemble of donors obey the set of kinetic equations [74, 75]

$$\frac{d\boldsymbol{S}_i}{dt} + \boldsymbol{S}_i \times \boldsymbol{\Omega}_i = \boldsymbol{\mathcal{Q}}_i, \tag{3.1}$$

where $\boldsymbol{S}_i$ is the electron spin at the site i, $\boldsymbol{\Omega}_i = \boldsymbol{\Omega}_{i,\text{nucl}} + \boldsymbol{\Omega}_B$ is the electron spin precession frequency caused by the hyperfine interaction with nuclear spins, $\boldsymbol{\Omega}_{i,\text{nucl}}$, and by the Larmor precession in the external field, $\boldsymbol{\Omega}_B$. The collision integral $\boldsymbol{\mathcal{Q}}_i$ describes the variations of the spins due to the electron hopping between sites, processes of ionization and recombination, exchange diffusion, etc. [64, 76]. The schematic illustration of the spin dynamics of localized electrons is presented in Fig. 3.7(a). Here we employ the simplest model of the collision integral by introducing a single correlation time τ_c, disregarding the spread of the transition probabilities [64, 74]. We assume that the nuclear fluctuations are frozen on the timescale of τ_c and that the Zeeman splitting in the external field is negligible as compared with the thermal energy. Hence, we obtain a simple analytical formula for the relaxation time of the spin component parallel to the magnetic field $\mathbf{B} \parallel z$ [74]:

$$T_{1,hf} = \frac{\tau_c \mathcal{A}}{1 - \mathcal{A}}, \tag{3.2}$$

where

$$\mathcal{A} = \left\langle \frac{1+\Omega_{i,z}^2\tau_c^2}{1+\Omega_i^2\tau_c^2} \right\rangle, \tag{3.3}$$

and the angular brackets denote the averaging over the distribution of random nuclear fields.

Equation (3.2) is valid for an arbitrary relationship between the spin precession frequency and τ_c. In the experimentally relevant range of magnetic field, $\Omega_B = |g\mu B|/\hbar$ exceeds by far the spin precession frequency in the field of nuclear fluctuations and the inverse correlation time. It follows then from Eqs. (3.2), (3.3) that

$$T_{1,hf} = \frac{3\tau_c\Omega_B^2}{2\langle\Omega_{\text{nucl}}^2\rangle} \propto \tau_c B^2, \tag{3.4}$$

where $\langle\Omega_{\text{nucl}}^2\rangle$ is the mean square fluctuation of the nuclear field averaged over the ensemble of donors. This expression shows the B^2 power law which is observed in experiment, Fig. 3.4.

This increase in spin-relaxation time with increasing field is related to the suppression of the relaxation by the magnetic field: At $\Omega_B \gg \tau_c^{-1}, \langle\Omega_{\text{nucl}}^2\rangle^{1/2}$, the electron spin precesses around the total field $\boldsymbol{\Omega}_B + \boldsymbol{\Omega}_{i,\text{nucl}}$ during the correlation time. Its precession axis is almost parallel to $\boldsymbol{\Omega}_B$ and its orientation changes by a small random angle $\sim \Omega_{i,\text{nucl}}/\Omega_B$ when the electron hops between the localization sites. Such a random process results in the spin relaxation rate $\sim \tau_c^{-1}(\Omega_{i,\text{nucl}}/\Omega_B)^2 \propto 1/(\tau_c B^2)$ in agreement with Eq. (3.4). For known mechanisms of electron correlation time at a donor, such as electron hopping and the exchange diffusion, see Ref. [76] for review, an exponential sensitivity to the donor density (and, in the former case, to the temperature) is expected [76, 77]. Correspondingly, for these mechanisms T_1 should be strongly affected by these parameters. Such trends are clearly seen in the experiment, Fig. 3.4 and Fig. 3.5(b).

The developed model enables quantitative comparison with the experiment. To that end, we evaluate the mean square of the donor-bound electron spin precession frequency in the nuclear field as [78]

$$\langle\Omega_{\text{nucl}}^2\rangle = \frac{V_0}{8\pi(a_B^*)^3\hbar^2}\sum_\alpha \left(A_\alpha^{hf}\right)^2 I_\alpha(I_\alpha+1), \tag{3.5}$$

where $a_B^* = \varepsilon\hbar^2/(m^*e^2)$ is the donor Bohr radius, $V_0 = a_0^3$ is the unit lattice volume, I_α is

the spin of αth nucleus in a unit cell, A_α is the hyperfine interaction constant. Taking for GaAs $A_{^{69}\text{Ga}} = 38.2$ μeV, $A_{^{71}\text{Ga}} = 48.5$ μeV and $A_{^{75}\text{As}} = 46$ μeV [79] we obtain $\sqrt{\langle\Omega^2_{\text{nucl}}\rangle} = 0.47 \times 10^8$ s^{-1}. Fitting the experimental data with Eq. (3.4), we determine a correlation time $\tau_c \approx 25$ ns for the GaAs-2 sample. Such a value of the correlation time is consistent with previous studies of GaAs samples with similar donor densities [65, 66]. A somewhat longer τ_c of ~ 40 ns is determined for the InP-2 sample, where the hyperfine interaction is dominated by ^{115}In isotopes with $I_{\text{In}} = 9/2$. The estimate for A_{In} comes from Ref. [80] where the Overhauser effect for InSb was measured. The literature reports a spread of A_{In}: 47 μeV [81], 56 μeV [82] and 84 μeV [79]. Here we use the middle value of $A_{\text{In}} = 56$ μeV, which yields $\sqrt{\langle\Omega^2_{\text{nucl}}\rangle} = 1.6 \times 10^9$ s^{-1}.

Although the experimental sensitivity of T_1 to temperature and carrier density are consistent with the known mechanisms contributing to the donor electron correlation time, the magnitude of τ_c is orders of magnitude shorter than these mechanisms predict for the low donor densities used in this study. Our result is consistent with prior works [65, 66] and suggests additional, unknown mechanisms may be at play, such as an inhomogeneous donor distribution resulting in the formation of clusters with a relatively high donor density, and short τ_c.

According to Eq. (3.4), the electron spin relaxation time associated with the hyperfine interaction strongly increases with an increase in field. Hence, at sufficiently strong magnetic fields this mechanism becomes inefficient as compared with mechanisms caused by the combination of the electron-phonon and spin-orbit interactions described below. By contrast, T_1 due to these processes decreases with an increase in B.

3.6.2 High-field spin-relaxation

While the spin-orbit interaction alone is not sufficient to cause a spin-flip of a localized charge carrier, a combination of the electron-phonon interaction and spin-orbit coupling serves as a main source of localized electron spin relaxation at high magnetic fields [83, 84, 85]. Phonons can also modulate the hyperfine coupling of the electron and the lattice-nuclei spins giving rise to $T_1 \propto B^{-3}$ dependence [83]. Similar to the quantum dot case, this effect is negligible

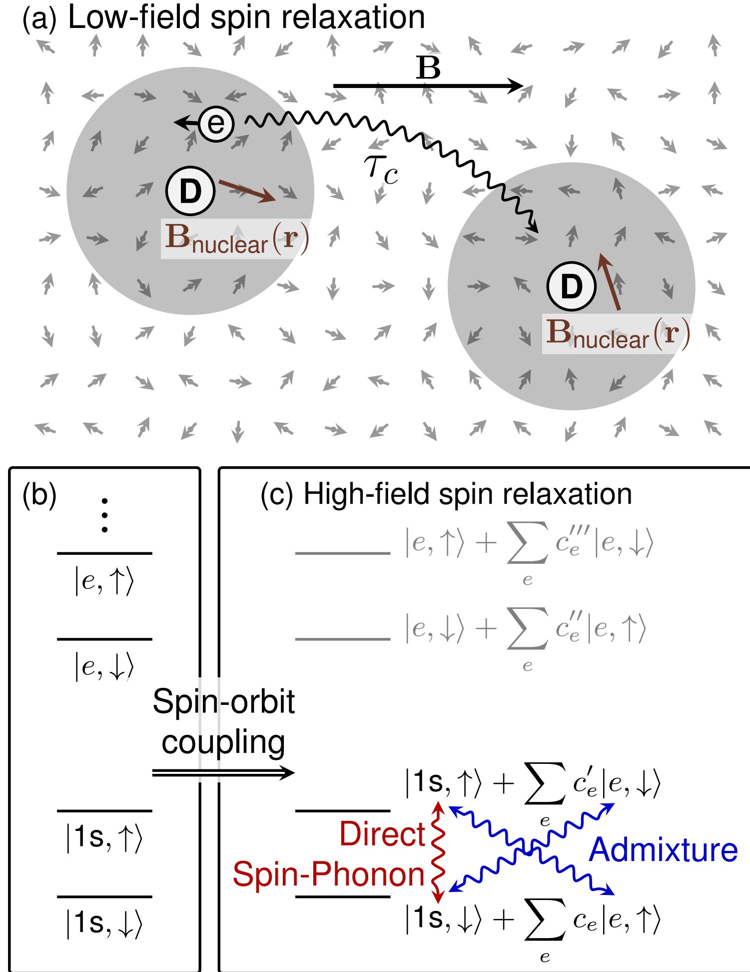

Figure 3.7: Schematic of spin-relaxation mechanisms. (a) At low magnetic fields, spin-relaxation is dominated by the interaction of the electron spin with lattice nuclear spins. Panels (b,c) are relevant for the high-field spin relaxation mechanism. (b) Energy level structure for unperturbed donor-bound electron in magnetic field, described by zero-field quantum numbers. (c) Dresselhaus spin-orbit coupling mixes states with opposite spin and different angular momentum components. In the admixture mechanism, phonons cause relaxation between the two eigenstates via the components with like spin. The direct spin-phonon interaction causes spin-relaxation via the components with opposite spin.

for donor-bound electrons. Two-phonon processes [84] are also very weak for the range of temperatures and fields studied here.

An exhaustive theoretical investigation of the spin-flip mechanisms has been performed for the related GaAs quantum dot system [50, 86, 87]. In GaAs quantum dots, all re-

ported spin-orbit related mechanisms exhibit a $T_1 \propto B^{-\nu}$ dependence with $\nu \geq 5$. For bulk GaAs-like semiconductors, such a study has not been performed before to the best of our knowledge. The orbitals for the donor-bound electron differ from those for quantum dots, leading to the use of a different approximation for the Dresselhaus spin-orbit Hamiltonian and different selection rules.

Experimentally we observe that the high-field spin relaxation is consistent with a single phonon process. This limits us to mechanisms that combine Dresselhaus spin-orbit coupling and spin-conserving phonon-induced relaxation, and direct spin-phonon mechanisms. In this section, we present the detailed calculation for the high-field T_1 due to both mechanisms and compare our theoretical results to the experimental data.

Admixture mechanism caused by Dresselhaus spin-orbit coupling

We are first interested in the spin relaxation between the Zeeman sublevels of the donor-bound electron ground state mediated by spin-orbit and electron-phonon coupling (admixture mechanism). This is the dominant relaxation mechanism for III-V quantum dots [50, 86] and naively may also be expected to play the dominant role in the similar donor system. For this mechanism, the spin-orbit interaction modifies the ground-state Zeeman sublevels by the admixture of the excited sublevels with the opposite spin component. Hence, the spin-independent electron-phonon coupling causes spin-relaxation through the components of the states with the same spin, as depicted in Fig. 3.7(b)-(c).

The interaction Hamiltonian for the admixture mechanism is

$$H_{adm} = U_{ph} + H_{so}, \tag{3.6}$$

where U_{ph} is the spin-conserving electron-phonon interaction Hamiltonian and H_{so} is the spin-orbit Hamiltonian. In the high-field limit, the Zeeman splitting can be comparable or even exceed the thermal energy. In such a case, the transition rates from the Zeeman sublevel $\downarrow$ to $\uparrow$, $\Gamma_{\uparrow\downarrow}$, and back, $\Gamma_{\downarrow\uparrow}$, differ. The observed longitudinal spin relaxation time satisfies

$$T_1 = (\Gamma_{\uparrow\downarrow} + \Gamma_{\downarrow\uparrow})^{-1}.$$

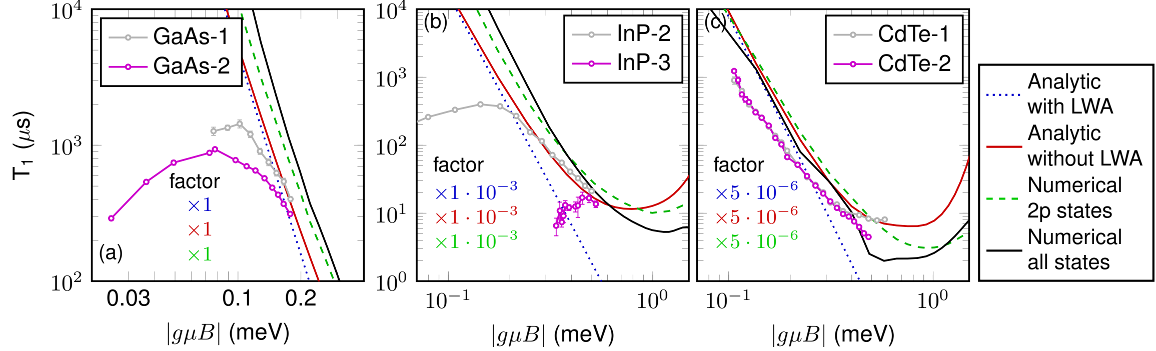

Figure 3.8: Theoretical results for spin-relaxation time T_1 via the admixture mechanism, using both analytic and numerical wave functions. Pink and grey dots show the experimental data. For GaAs [panel (a)], the theory matches the data reasonably well with no fit parameters. For InP (b) and CdTe (c), the calculated values are multiplied by the factor specified in the figure for ease of comparison. $T = 1.5$ K. We note that the numerically calculated T_1 which includes only the 2p states is slightly shorter than the full numerical solution. This is due to destructive interference between the orbital states in Eq. (3.8).

The individual rates are found using Fermi's golden rule, e.g.,

$$\Gamma_{\downarrow\uparrow} = \frac{2\pi}{\hbar} \sum_{\mathbf{q},\alpha} |M_{\downarrow\uparrow}|^2 \delta(\hbar q s_\alpha - |g\mu B|), \tag{3.7}$$

where $\mathbf{q}$ is the phonon wavevector, s_α is the speed of sound in phonon branch α and $\alpha = t, l$ for the transverse and longitudinal modes, respectively. Hereafter we assume for convenience that the spin-up state has higher energy than the spin-down one, hence, $g\mu B > 0$, as illustrated in Fig. 3.7, so that the rate in Eq. (3.7) corresponds to the phonon emission process. Electron spin-relaxation occurs via a second order process due to the quantum interference of U_{ph} and H_{so} in the Hamiltonian (3.6), see Ref. [50] for details,

$$\begin{aligned} M_{\downarrow\uparrow,adm} = -\sum_e \Bigg[&\frac{\langle 1\mathrm{s}, \downarrow | U_{ph} | e, \downarrow\rangle\langle e, \downarrow | H_{so} | 1\mathrm{s}, \uparrow\rangle}{E_e - E_{1\mathrm{s}} + g\mu B} \\ &+ \frac{\langle 1\mathrm{s}, \downarrow | H_{so} | e, \uparrow\rangle\langle e, \uparrow | U_{ph} | 1\mathrm{s}, \uparrow\rangle}{E_e - E_{1\mathrm{s}} - g\mu B} \Bigg], \end{aligned} \tag{3.8}$$

where $|1\mathrm{s}\rangle$ is the ground orbital state of the donor-bound electron, $|e\rangle$ denotes the excited orbital states, and E_e, $E_{1\mathrm{s}}$ are the energies of the corresponding orbitals.

	GaAs	InP	CdTe
g	-0.44	1.3	-1.67
m^*	$0.067m_0$	$0.08\,m_0$	$0.106m_0$ [88]
h_{14} (V/m)	14.5×10^8 [89]	7.4×10^8 [90]	3.94×10^8 [88]
γ (eV·Å^3)	23.7 [91]	10.1 [91]	11.74 [88]
ρ (kg/m^3)	5.32×10^3 [92]	4.81×10^3 [92]	4.85×10^3 [88]
s_l (m/s)	4.73×10^3 [92]	4.58×10^3 [92]	3.08×10^3 [88]
s_t (m/s)	3.35×10^3 [92]	3.08×10^3 [92]	1.85×10^3 [88]
ε	12.56	12.5 [92]	~ 10.3 [93]
v_0 (m/s)	8×10^5 [94]	4×10^5 [94]	unknown
D (eV)	-5.55 [95]	-4.4 [95]	-5.45 [95]

Table 3.2: Material parameters relevant to the donor-bound electron spin-relaxation in GaAs, InP, and CdTe. g is the effective electron g-factor, m^* is the electron effective mass (m_0 is the free electron mass), h_{14} is the piezoelectric constant, γ is the Dresselhaus spin-orbit coupling constant, ρ is the mass-density, s_l is the longitudinal sound velocity, s_t is the transverse sound velocity, ε is the relative permittivity of the material, v_0 characterizes the strength of the direct spin-phonon coupling interaction, and D is the deformation potential interaction constant.

Due to the small localization energy of the donor-bound electron ($\lesssim$ 10 meV), the electron wave function in a magnetic field is well described with effective mass theory using the hydrogenic Hamiltonian

$$H_0 = \frac{\hbar^2}{2m^*}\left(\mathbf{k} - \frac{e}{\hbar}\mathbf{A}\right)^2 - \frac{1}{4\pi\varepsilon_0}\frac{e^2}{\varepsilon r} + \frac{1}{2}g\mu\boldsymbol{\sigma}\cdot\mathbf{B}, \tag{3.9}$$

where m^* is the electron effective mass, e is the electron charge, $\mathbf{A}$ is the vector potential of the magnetic field $\mathbf{B}$, $\mathbf{r}$ is the position vector, $r = |\mathbf{r}|$, $\mathbf{k} = -i\partial/\partial\mathbf{r}$ is the wavevector, ε is the relative dielectric constant of the material, and $\boldsymbol{\sigma}$ is the vector composed of the Pauli matrices. In the presence of the magnetic field, the Hamiltonian, Eq. (3.9), possesses an axial symmetry and its eigenstates are characterized by four quantum numbers: principal quantum number ν, angular momentum z-projection m, z-parity π_z and spin z-projection m_s. To establish a link with the hydrogen-like series of donor-bound electron states at $B = 0$, we will label the orbitals by their zero-field quantum numbers nlm, where n is the principal quantum number and l is the angular momentum quantum number, when

appropriate.

The energy of a phonon involved in the spin-flip transition is the Zeeman splitting between the spin sublevels. Therefore, the phonon wavevector $q_\alpha = g\mu B/(\hbar s_\alpha) \to 0$ as $B \to 0$. Thus, at moderate magnetic fields in piezoelectric crystals such as GaAs, InP and CdTe studied here, we found that the piezoelectric electron-phonon interaction with $U_{ph}^{(pz)} \propto q^{-1/2}$ dominates over the deformation potential interaction, where $U_{ph}^{(dp)} \propto q^{1/2}$ [96], see Appendix A.3. The piezoelectric electron-phonon interaction reads

$$U_{ph}^{(pz)} = \sqrt{\frac{\hbar}{2\rho\omega_{\mathbf{q},\alpha}}} e^{i(\mathbf{qr}-\omega_{\mathbf{q},\alpha}t)}(eA_{\mathbf{q},\alpha})b_{\mathbf{q},\alpha}^\dagger + \text{c.c.}, \tag{3.10}$$

where

$$A_{\mathbf{q},\alpha} = h_{14}\sum_{ijk}\beta_{ijk}\xi_i\xi_j\hat{e}_k^{(\mathbf{q},\alpha)}, \tag{3.11}$$

ρ is the mass density of the material, $\omega_{\mathbf{q},\alpha}$ is the phonon frequency, $b_{\mathbf{q},\alpha}^\dagger$ is the creation operator for a phonon, $\boldsymbol{\xi} = \mathbf{q}/q$ is the unit vector along the phonon wavevector, $\hat{\boldsymbol{e}}$ is the phonon polarization vector, the only nonzero components of β_{ijk} are those with different subscripts, $\beta_{xyz} = \ldots = \beta_{zyx} = 1$, and h_{14} is the piezoelectric constant [96].

Since all the samples studied here are bulk semiconductors characterized by the T_d point symmetry group, the only relevant spin-orbit coupling comes from the cubic-in-the-electron-wavevector Dresselhaus spin-orbit term, H_{so}. It arises from the lack of inversion symmetry in zinc-blende crystals and has the form

$$H_{so} = \gamma\sum_i \sigma_i k_i(k_{i+1}^2 - k_{i+2}^2), \tag{3.12}$$

where γ is the Dresselhaus spin-orbit coupling constant and the subscript i cycles through x, y, z.

In the limit of $|g\mu B|a_B^*/(\hbar s_\alpha) \ll 1$ (a_B^* is the effective Bohr radius), the long wavelength approximation (LWA) is used to simplify the T_1 calculation, i.e. the approximation of $e^{i\mathbf{qr}} = 1 + i\mathbf{qr}$. This is used in previous literature [50] but we find it does not work well at the high fields for InP and CdTe. Therefore, we have performed the full numerical

evaluation of the spin relaxation time according to Eqs. (3.7) and (3.8) using the numerical solutions to Eq. (3.9) [97] and the material parameters from Table 3.2. Additional details on the numerical calculation can be found in Appendix A.2. These results, which include 18 excited state orbitals, are given by the black curves in Fig. 3.8. We numerically find that the first excited state which evolves from $2\mathrm{p}_-$ makes the dominant contribution to the spin relaxation rate, as shown by the dashed green curves in Fig. 3.8.

This numerical result, together with the analysis of the wavefunctions in Appendix A.3, motivates using Gaussian shapes of the ground and excited state wave functions, Eqs. (A.9), to obtain an analytic solution for further insight into the intermediate field behavior. The magnetic field induced shrinking is taken into account by assuming different characteristic lengths $l_{z,1\mathrm{s}} = a_B^*$ and $l_{\rho,1\mathrm{s}} = [1/(a_B^*)^2 + 1/(2l_b^2)]^{-1/2}$ for the motion along and perpendicular to the field. After some transformations, we obtain (see Appendix A.3 for details):

$$\frac{1}{T_{1,adm}} = \frac{256\chi^{10}}{35(1+\chi^2)^{12}} \frac{\gamma^2 e^4 h_{14}^2 |g\mu|^3 B^5}{\pi\rho\hbar^6} \times \\ \times \left(\frac{1}{\Delta E} - \frac{1}{\Delta E + \hbar\omega_c}\right)^2 \left(\frac{f_l}{s_l^5} + \frac{4f_t}{3s_t^5}\right) F_{ph} \,. \quad (3.13)$$

Here, $\Delta E = E_{2\mathrm{p}_-} - E_{1\mathrm{s}}$ is the energy difference between the hydrogen-like ground 1s and excited $2\mathrm{p}_-$ state. The factors $f_\alpha = \exp\{-(\chi g\mu B l_\rho)^2/[(1+\chi^2)\hbar^2 s_\alpha^2]\}$ take into account that the phonon wavelength can be comparable with the donor-bound electron state size. These factors are particularly sensitive to the wavefunction shape. Finally, the parameter χ is a parameter of the wave functions which characterizes the ratio of the effective radii for the excited and the ground states, see Eqs. (A.9). By comparing the trial wavefunction to the numerical 2p wavefunction, we find reasonable choices for χ of 1.5, 1.7 and 2.2 for GaAs, InP and CdTe over the experimental range of magnetic field, as shown in Fig. A.3. The magnitude of $T_{1,adm}$ calculated according to Eq. (3.13) is quite sensitive to the choice of χ.

A comparison between the experimental, numerical, and analytic results for T_1 is shown in Fig. 3.8. We stress that these calculations contain no fitting parameters. Qualitatively we observe similar behavior between the analytic and numerical calculations. At sufficiently

strong magnetic fields, we find the LWA fails for InP and CdTe due to their relatively large electron g-factors as compared with GaAs. This effect is taken into account by factors f_l and f_t in Eq. (3.13). It softens the exponent in B-dependence giving approximately $3 \lesssim \nu \lesssim 4$ in the accessible field range. Further increase in B results in a minimum in $T_1(B)$. It is noteworthy that at such magnetic fields, the deformation potential interaction may become important, see [98] and Appendix A.3 for details; moreover, in such fields the result could be quite sensitive to the shape of the wave functions. Hence, for sufficiently high fields, Eq. (3.13) provides only an indication of the trend.

We find that the numerically calculated values of T_1 for InP and CdTe are orders of magnitude longer than the experimentally observed spin relaxation times in these samples, which indicates the importance of other spin-flip mechanisms in the materials, see below. By contrast, in GaAs the calculated magnitude of T_1 is quite close to the experimental values, demonstrating that the admixture mechanism is significant in this material.

Direct spin-phonon interaction

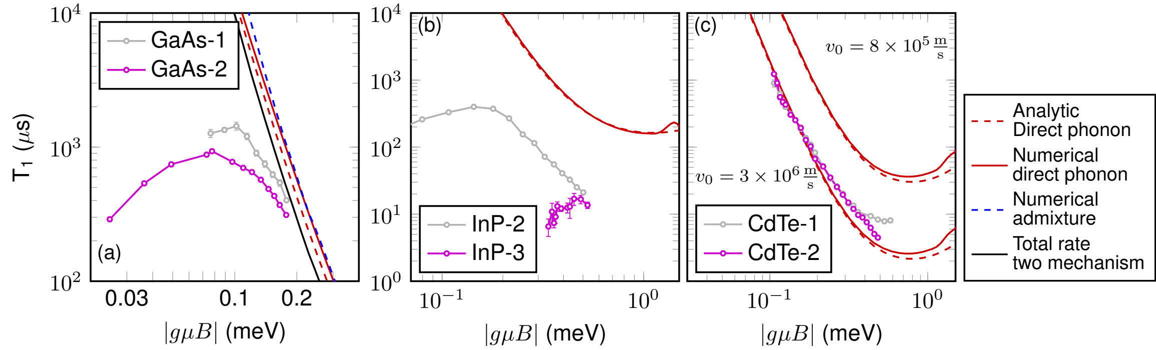

Figure 3.9: Theoretical results for the spin-relaxation time T_1 via the direct spin-phonon mechanism for GaAs (a), InP (b) and CdTe (c). Pink and grey dots show the experimental data. $T = 1.5$ K. The two dashed lines and two solid lines in (c) represent the analytic and numerical calculation results of T_1 using $v_0 = 8 \times 10^5$ m/s (upper curves) and $v_0 = 3 \times 10^6$ m/s (lower curves)

Although the direct spin-phonon interaction was not found to be a dominant relaxation mechanism for electrons in semiconductor quantum dots [50], we demonstrate here that

it contributes significantly to donor-bound electron spin relaxation. To some extent, this is because the role of the admixture mechanism is diminished due to the cubic-in-the-wavevector spin-orbit splitting in the bulk material, as compared with **k**-linear terms used for quantum dot systems [50]. The direct spin-phonon interaction Hamiltonian is [94]

$$U_{dir} = \frac{\hbar v_0}{2}[\sigma_x(u_{xy}k_y - u_{xz}k_z) + \sigma_y(u_{yz}k_z - u_{yx}k_x) + \sigma_z(u_{zx}k_x - u_{zy}k_y)], \quad (3.14)$$

Here $u_{ij} = u_{ji}$ is the deformation tensor, and, as above, $\mathbf{k} = -i\boldsymbol{\nabla} - (e/\hbar)\mathbf{A}$. The coupling constant v_0 has the dimension of velocity. It has been determined by experiment for GaAs and InP but is unknown for CdTe (see Table 3.2). For numerical evaluation for CdTe, we use a spread of values, 8×10^5 m/s $< v_0^{\mathrm{CdTe}} < 3 \times 10^6$ m/s with the lower (upper) bound corresponding to v_0^{GaAs} $\left(v_0^{\mathrm{InSb}}\right)$ [94].

The relaxation rates $\Gamma_{\uparrow\downarrow}$ are calculated using Eq. (3.7) with the first-order matrix element $M_{\uparrow\downarrow} = \langle 1\mathrm{s}, \uparrow |U_{dir}| 1\mathrm{s}, \downarrow\rangle$, as depicted in Fig. 3.7(c). We use an approximate exponential wave function with a characteristic length $l = [(a_B^*)^{-2} + 1/(2l_b^2)]^{-1/2}$ to obtain analytic expressions for $\Gamma_{\uparrow\downarrow}$ and, correspondingly, for the associated longitudinal spin relaxation time $T_{1,dir}$. The choice of the wave function is motivated by the fact that only the 1s orbital state is involved, which is not significantly perturbed at the experimentally accessible magnetic fields. Moreover, the precise symmetry of the wave function for the direct phonon mechanism is not critical. The evaluation of Eq. (3.7) yields (see Appendix A.4):

$$\frac{1}{T_{1,dir}} = \frac{(ev_0 l^2)^2 |g\mu|^5 |B|^7}{560\pi\rho\hbar^6} F_{ph} \times \left(\frac{1}{s_l^7} \frac{1}{(1+Q_l^2)^6} + \frac{4}{3s_t^7} \frac{1}{(1+Q_t^2)^6} \right), \quad (3.15)$$

where $Q_\alpha = |g\mu B| l/(2\hbar s_\alpha)$. Equation (3.15) demonstrates that the spin-flip time is proportional to B^{-7} at weak magnetic fields. An increase in the field results in a softening of the B-field dependence due to decrease of the efficiency of the electron-phonon interaction (breakdown of the LWA) described by the factors $(1 + Q_\alpha^2)^{-6}$. In addition to the analytic approximation, we performed the full calculation using the numerically-obtained ground-state donor wave function. The very good agreement between the analytic and numerical calculations, seen in Fig. 3.9, can be attributed to the minor effect of the magnetic field on

the ground-orbital-state wave functions at the experimental fields.

A comparison between the theoretical calculations with no fit parameters and the experimental data is also provided in Fig. 3.9. For GaAs, we find that the magnitude of the direct-phonon mechanism is approximately the same as the admixture mechanism. Also included in Fig. 3.9(a) is the sum of these two mechanisms. Accounting for both mechanisms results in a difference between the theory and the data of approximately a factor of 2, which can be easily attributed to the uncertainties in the system parameters in Table 3.2.

For InP and CdTe, the direct spin-phonon mechanism is found to be significantly stronger than the admixture mechanism. For CdTe, the agreement between theory and experiment is extremely good if the direct spin-phonon interaction strength in CdTe is similar to that of InSb. This may be reasonable given the similar valence band spin-orbit splitting in the two materials, 0.8 eV in InSb [99] and 0.9 eV in CdTe [100, 101, 102]. Here, an independent measurement of v_0, like those performed in Ref. [94] for GaAs and InP, or its independent first-principles calculation, is needed to corroborate our result.

There is still a significant discrepancy between theory and experiment for InP, where the experimental spin-relaxation time is 15 to 30 times shorter than the predicted value from the direct spin-phonon coupling. Its origin is not clear and further studies, both experimental and theoretical, are needed to resolve this discrepancy.

3.7 Conclusion

In this work we measure the longitudinal spin relaxation time as a function of magnetic field for electrons bound to donors in three different high-purity direct bandgap semiconductors. We observe for the first time the crossover between low-field spin relaxation resulting from a hyperfine coupling of the electron and lattice nuclear spins and high-field single-phonon-mediated spin relaxation. From a fundamental perspective, the existence of both regimes is expected. However, the comparison of the data with the developed theory in terms of the magnitude of the relaxation raises new questions. Low field measurements indicate a tens of nanoseconds electron spin correlation time of so far unknown origin. High-field measurements strongly suggest the admixture mechanism is important in GaAs, while the direct spin-phonon interaction is important in both CdTe and GaAs. However for InP, the

discrepancy between theory and experiment calls for further investigation.

In the context of possible applications, the high-field $B^{-\nu}$ dependence of T_1, combined with the density and temperature dependent low-field B^2 behavior, has practical implications. If the crossover point can be pushed to lower fields, extremely-long spin-relaxation times may be possible. This could be realized with lower impurity density, lower temperature, larger binding energies, and a nuclear-spin-free matrix. In support of this, we note that no crossover is observed in CdTe even when $k_B T > |g\mu B|$. This may reflect the role of the higher donor binding energy and/or the reduced nuclear-spin environment in CdTe. In this context, isotope purification, which is known to significantly affect spin dephasing, may also significantly increase the maximum achievable T_1 for electrons bound to shallow donors.

Chapter 4

COHERENCE PROPERTIES OF DONORS IN ZNO

4.1 Introduction

In the last chapter, we study the longitudinal spin relaxation in three different materials: GaAs, InP and CdTe. The T_1 of them are all at ms-scale which is not really long. The theoretical model shows the spin relaxation is limited by electron-phonon interaction mediated by spin-orbit coupling. This theory study indicates the T_1 can be longer in a material with smaller spin-orbit coupling. This leads to our study of donors in ZnO. The electron g-factor of ZnO is about 2, really close to the g-factor of a free electron, which is an indication of small spin-orbit coupling and longer T_1. In this chapter, we perform a systematic study of the coherence properties for donors in ZnO.

Defect centers in crystals have attracted significant attention as qubit candidates for quantum communication [103, 104] and computation [105] due to the ability to realize spin-photon entanglement and scalable device integration. A two-node network, the fundamental building block for measurement-based quantum computation [4, 106, 107] and long-range quantum communication [7, 8], can be generated via a single photon measurement on two non-interacting, spatially separated qubits. The quantum link efficiency, i.e. the ratio between the entanglement generation and the decoherence rates, determines the scalability of a network. Finding a system which combines homogeneous and efficient optical properties with a long spin coherence time is still an outstanding challenge. The negatively charged nitrogen-vacancy (NV) center [108, 109] in diamond is one of the leading candidates for the photon based protocols and two-node networks have been demonstrated [17]. However, the entanglement generation rate is typically low, limited by nonideal optical properties such as optical inhomogeneity, spectral diffusion, and low zero-phonon radiative efficiency. Whilst numerous efforts are focused on overcoming these challenges in diamond [110] and

This chapter is a slightly modified version of a published paper written by the author of this thesis [14].

related SiC systems [111, 112], searching for new defect centers with better properties is an alternative solution. Donors in isotope purified ^{28}Si have shown promising features such as ultra-long coherence times [1, 2] and high fidelity qubit control [3]. However, the indirect band gap of Si makes photon-mediated entanglement and therefore the development of scalable quantum networks challenging [4, 5, 6]. While there are photon emitting defects in Si [113, 114, 115], the radiative efficiency is typically low. Studies of defect systems in direct band-gap III-V materials, such as quantum dots and donors, have demonstrated efficient optical transitions, spin control and spin readout [9, 10, 11, 116, 117]. A two-node network with a kHz generation rate has been realized in the positively-charged quantum dot system [20]. However, due to the lack of a spin-free host matrix, the spin coherence times in III-V systems are limited by hyperfine interactions with the host nuclear spins [20, 12]. Donors in direct band-gap II-VI semiconductors similarly boast efficient optical transitions [118] and, as we show here in ZnO, can exhibit long coherence times. Critical for long-term qubit viability is the compatibility of ZnO with microfabrication processing [119, 120] and the possibility of entanglement generation between the ZnO donor electron and donor/lattice nuclei based on the hyperfine interaction [121]. This electron-nucleus register, demonstrated in both P:Si [122] and NV:diamond systems [123], enables deterministic network scaling in the presence of large photon loss [4, 124].

In this charpter, we measure the relaxation and coherence properties of an ensemble of Ga donors in ZnO. Ensemble spin initialization is demonstrated using resonant continuous-wave (cw) excitation. The longitudinal spin relaxation time T_1 shows a $B^{-3.5}$ relationship, dominated by a spin-orbit mediated phonon interaction. The longest T_1 observed in the experiment is $\sim$0.1 s at 2.25 T, with T_1 increasing with decreasing field. Coherent spin control of donor electrons is achieved with ultra fast optical pulses, red-detuned from the neutral donor (D^0) to donor-bound exciton (D^0X) resonance. The D^0 coherence is then probed via all-optical Ramsey interferometry and spin-echo measurements [11]. The inhomogeneous dephasing time T_2^* is measured to be 17 ± 2 ns which is consistent with the theoretical estimates of inhomogeneous electron-nuclear hyperfine interaction in natural ZnO. The effect of the inhomogeneous nuclear field is suppressed by a spin echo sequence with a measured spin-echo time T_2 of 50 ± 13 μs at 5 T. Possible mechanisms limiting T_2 include spectral

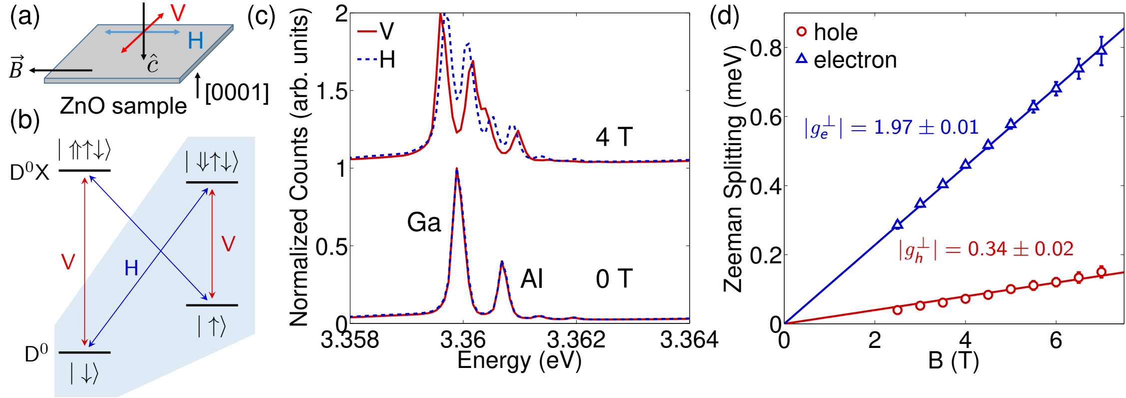

Figure 4.1: (a) Experimental geometry. $\hat{c}$ is the optical propagation axis. $\vec{B}$ is the magnetic field. V and H represent vertical polarization ($\hat{\varepsilon} \perp \vec{B}$) and horizontal polarization ($\hat{\varepsilon} \parallel \vec{B}$), respectively. (b) Energy diagram of the donor system at magnetic field in the Voigt geometry. $|\Uparrow\rangle(|\uparrow\rangle)$ denotes the hole (electron) spin. The shaded area shows the Λ system used for the spin initialization and readout. (c) Spectra at 0 T and 4 T with V and H polarized collection. The excitation laser is at 3.446 eV with vertical polarization. Temperature is 5.5 K. Both the Ga and Al donor peaks split into 4 different peaks with applied magnetic field. (d) Electron and hole Zeeman splitting of the Ga donor as function of magnetic fields. The red and blue lines are linear fits of the Zeeman splitting. For these data, both the excitation and collection spot sizes are ∼1 µm.

diffusion due to flip-flops of ^{67}Zn nuclear spin pairs [125] and instantaneous diffusion due to the rephasing pulse in the spin echo sequence [126].

4.2 Setup and Photoluminescence spectrum

The ZnO sample studied in this chapter is a 360 µm thick Tokyo Denpa ZnO crystal. The sample included a 0.7 µm high-purity ZnO epilayer grown by molecular beam epitaxy [127], however the measurement signal was dominated by substrate donor emission. The total donor concentration is on the order 10^{17} cm^{-3}, determined by capacitance-voltage measurements [128]. The sample is mounted in a continuous flow cryostat with a superconducting magnet in Voigt geometry, i.e. $\hat{c} \perp \vec{B}$, where $\hat{c}$ is the optical propagation axis, as shown in Fig. 4.1(a). $\hat{c}$ is parallel to the [0001] direction of the ZnO crystal. All measurements are performed at temperatures between 1.5 and 5.5 K.

The energy diagram of the shallow donor in a magnetic field is shown in Fig. 4.1(b).

The D^0 spin states split due to the electron Zeeman effect. The Zeeman splitting of the D^0X state is solely determined by the hole spin, as the two bound electrons form a spin singlet. The two ground spin states $|\uparrow\rangle$, $|\downarrow\rangle$ and the excited state $|\Downarrow\uparrow\downarrow\rangle$ form the Λ system which is used for spin initialization and readout. Typical spectra at 0 T and 4 T are shown in Fig. 4.1(c). At 0 T, the two main peaks correspond to Al donors (3.3607 eV) and Ga donors (3.3599 eV) [129]. To further confirm the two peaks are from donors, PL spectra with resonant excitation are taken to demonstrate the correlation between the main donor peaks and the corresponding two electron satellite (TES) transitions, as shown in Fig. 4.2. The TES transitions are transitions from the D^0X to the $2s$ and $2p$ D^0 orbital states. Enhancement of the TES transitions are observed with resonant excitation of the main D^0X lines for both the Ga and Al donors. At 4 T, the Al and Ga peaks each split into 4 peaks due to the electron and hole Zeeman splitting. The polarization dependence of the 4 peaks confirms the Γ_7 valence band symmetry assignment [130]. The measured in-plane g-factors for the Ga donors are $|g_e^{\perp}| = 1.97 \pm 0.01$ and $|g_h^{\perp}| = 0.34 \pm 0.02$, determined by linear fits of the electron and hole Zeeman splitting at different fields, as shown in Fig 4.1(d). For the remainder of the chapter, we will focus on the Ga donor.

D^0X centers (Al, Ga and In) in ZnO exhibit short radiative lifetimes of $\sim$1 ns [118] and Huang-Rhys parameters $<$0.1 [118] which indicate high radiative efficiency in the zero-phonon line. This provides a natural Λ system for Raman-based photon-heralded entanglement schemes [131]. The ability to utilize other valence-band D^0X transitions [129, 132, 133] to realize highly desirable cycling transitions and "L"-shaped systems will be investigated in future work.

4.3 Spin initialization and T_1 measurement

Spin initialization, the first step to utilize the spin as a qubit, is performed by optical pumping. A cw pump pulse is resonantly applied on either the $|\uparrow\rangle \Leftrightarrow |\Downarrow\uparrow\downarrow\rangle$ or $|\downarrow\rangle \Leftrightarrow |\Downarrow\uparrow\downarrow\rangle$ transition to initialize to $|\downarrow\rangle$ or $|\uparrow\rangle$, respectively. To visualize the optical pumping, the spins are first prepared using a scrambling pulse, i.e. a series of high power laser pulses with photon energy higher than the donor transitions. Then a cw pump pulse is applied resonantly on the $|\uparrow\rangle \Leftrightarrow |\Downarrow\uparrow\downarrow\rangle$ transition to initialize to $|\downarrow\rangle$. PL from the $|\downarrow\rangle \Leftrightarrow |\Downarrow\uparrow\downarrow\rangle$

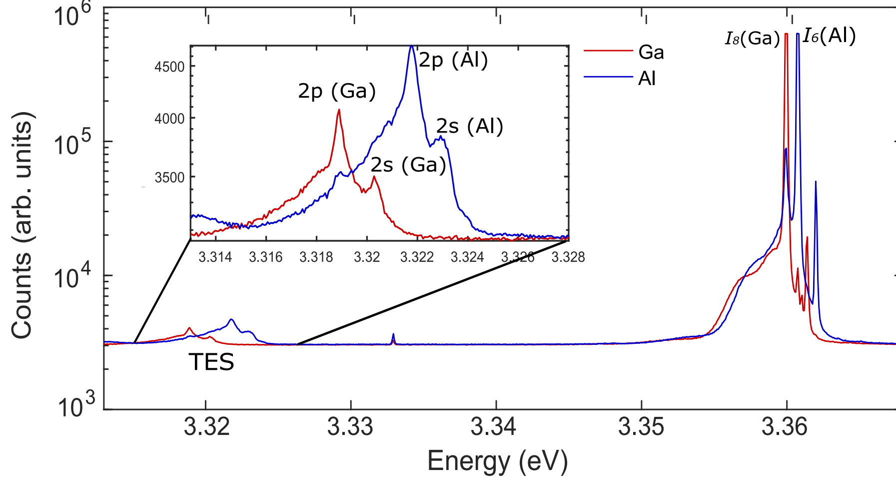

Figure 4.2: Log-scale resonant photoluminescence spectra of the ZnO sample at 0 T, 1.5 K. Excitation laser is resonantly exciting the Ga (red) or Al (blue) main donor-bound exciton transition. The inset shows the enhancement of the two-electron satellite peaks.

transition is collected during the pump pulse. A typical optical pumping curve is shown in Fig. 4.3(a). An estimate of the pumping efficiency using the contrast ratio of the optical pumping curve [123] yields a fidelity of 95% at 1.5 K and 5 T. This estimate assumes that the scrambling pulse prepares the spins with equal population in $|\uparrow\rangle$ and $|\downarrow\rangle$. The efficiency of the optical pumping decreases with decreasing magnetic field. At low field, the Zeeman energy becomes comparable to the optical linewidth of the D^0X transitions. In this case, population in $|\downarrow\rangle$ can be simultaneously pumped back to $|\uparrow\rangle$. For this reason, we are only able to observe an optical pumping signal at fields larger than 2.25 T.

T_1 is measured by recording the population recovery to thermal equilibrium after spin initialization. The spin is initialized to $|\uparrow\rangle$ using a 50 μs cw pulse on resonance with the $|\downarrow\rangle \Leftrightarrow |\Downarrow\uparrow\downarrow\rangle$ transition. Then after waiting for a variable time τ, another 50 μs cw pulse is applied and the PL of the $|\uparrow\rangle \Leftrightarrow |\Downarrow\uparrow\downarrow\rangle$ transition is collected in the first 1 μs window of the cw pulse. The collected PL signal is proportional to the $|\downarrow\rangle$ population. By changing

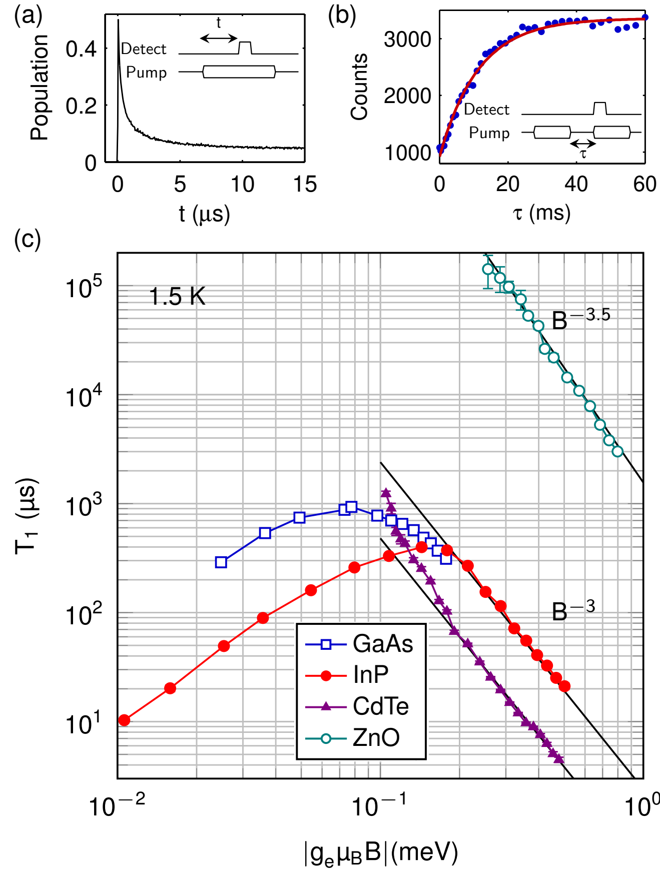

Figure 4.3: (a) Optical pumping curve at 5 T, 1.5 K. The inset shows the laser sequence. The PL is detected by an avalanche photodiode with a 50 ns timing resolution. (b) The population recovery curve at 5 T, 1.5 K. The inset shows the corresponding laser sequence. The exponential fit of the recovery curve gives $T_1 = 11.4 \pm 0.5$ ms. (c) The longitudinal spin relaxation time T_1 as a function of the Zeeman energy for donors in GaAs, InP, CdTe and ZnO. The data for GaAs, InP and CdTe is reproduced from a prior work [134]. For the ZnO data, both the excitation and collection spot sizes are ∼1 µm.

τ, a population recovery curve is measured and T_1 is extracted using an exponential fit (Fig. 4.3(b)).

T_1 at 1.5 K as function of magnetic field is shown in Fig. 4.3(c), with previous measurement results in GaAs, InP and CdTe [134] included for comparison. In the high-field region, the strong inverse power dependence on B indicates that relaxation is induced by phonon interactions, mediated by electron spin-orbit coupling [135]. The high B-field dependence in ZnO is similar to what is observed in the other three semiconductors. However, $T_{1,\mathrm{ZnO}}$ is over two orders of magnitude longer as a result of lower spin-orbit coupling. The longest observed T_1 is 0.14 ± 0.05 s at 2.25 T. This is 10^5 times longer than previously reported results in ZnO epilayers [132].

At low field, a positive B-field dependence of T_1 is observed in GaAs and InP due to the inhomogeneous static hyperfine field and the short electron correlation time at the donor sites [134]. In ZnO, this mechanism is expected to be weaker because of the small electron Bohr radius and thus longer correlation time. The high B-field dependence, together with the small Bohr radius, suggest T_1 can approach and possibly exceed seconds at lower magnetic fields. Control of the spin at lower fields will require a high-purity sample with narrow optical linewidth, as optical pumping can only be efficient if the linewidth is much smaller than the Zeeman splitting.

4.4 Calibration of Spin Population

For data in Fig. 4.3(a) and Fig. 4.5, the spin population is detected by applying a cw pulse resonantly on transition $|\uparrow\rangle \Leftrightarrow |\Downarrow\uparrow\downarrow\rangle$ and collecting PL from transition $|\downarrow\rangle \Leftrightarrow |\Downarrow\uparrow\downarrow\rangle$. Typical data of collected PL as function of time is shown in Fig. 4.4. The pump-down counts are normalized to 1. The peak count is I_m and is proportional to the spin $|\uparrow\rangle$ population $P_\uparrow$.

$$P_\uparrow = \beta I_m. \tag{4.1}$$

β can be calibrated by measuring peak count $I_m(P_\uparrow = 1/2)$ of the half $|\uparrow\rangle$ half $|\downarrow\rangle$ state, generated by a series of high power laser pulses with photon energy much higher than the

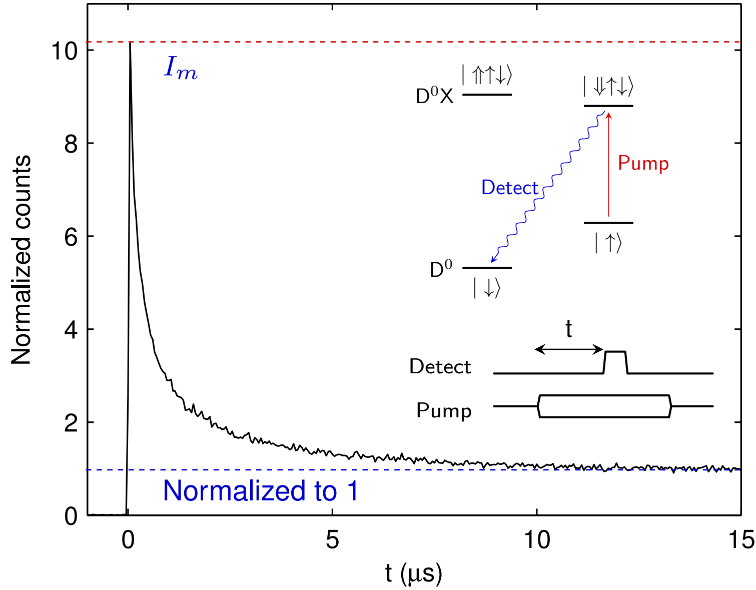

Figure 4.4: Typical curve of collected PL as function of t after applying a cw pumping pulse. The insets are the laser sequence and energy diagram showing the transitions of detection and pumping.

donor transitions.

$$\beta = \frac{1/2}{I_m(\mathrm{P}_\uparrow = 1/2)}. \tag{4.2}$$

In the measurement of T_2^* and T_2 (Sec. 4.6), to have a better signal to noise ratio, the excitation spot is reduced to have the same size as the collection spot allowing all PL in the excitation spot to be collected. Though this increases the PL collection efficiency, different donors in the excitation spot experience different excitation powers and thus different spin rotation angles. Therefore, this calibration procedure is not accurate and the data shown in Fig. 4.6 is the fringe amplitude of the normalized counts.

4.5 Optical spin coherent control

In the next series of measurements we use ultrafast optical pulses to create and probe the electron spin coherence. To obtain both strong optical pumping efficiency and long T_1, we choose an intermediate magnetic field to study, i.e. 5 T. At 5 T, the large electron Zeeman

splitting (138 GHz) makes direct microwave control of the electron spin challenging. An alternative is to use a detuned ultra-fast optical pulse to coherently rotate the spins [136, 116], which can be understood using a 4-level density matrix model. For the 4-level donor system, the Hamiltonian in the interaction picture with the rotating wave approximation is

$$H = \begin{pmatrix} 0 & 0 & -\frac{\Omega_{13}(t)}{2} & -\frac{\Omega_{14}(t)}{2} \\ 0 & \omega_e & -\frac{\Omega_{23}(t)}{2} & -\frac{\Omega_{24}(t)}{2} \\ -\frac{\Omega_{13}^*(t)}{2} & -\frac{\Omega_{23}^*(t)}{2} & \Delta & 0 \\ -\frac{\Omega_{14}^*(t)}{2} & -\frac{\Omega_{24}^*(t)}{2} & 0 & \Delta+\omega_h \end{pmatrix}, \tag{4.3}$$

where $\omega_e(\omega_h)$ is the energy of the electron (hole) Zeeman splitting, Δ is the red detuning between the ultra-fast laser and the transition $|\downarrow\rangle \Leftrightarrow |\Downarrow\uparrow\downarrow\rangle$, $\Omega_{ij}(t) = \overrightarrow{\mu_{ij}} \cdot \overrightarrow{E}(t)/\hbar$ is the product of the electric field and the dipole matrix element of transition $|i\rangle \Leftrightarrow |j\rangle$ ($i = 1, 2, 3, 4$ corresponding to states $|\downarrow\rangle$, $|\uparrow\rangle$, $|\Downarrow\uparrow\downarrow\rangle$, $|\Uparrow\uparrow\downarrow\rangle$).

4.5.1 effective 2-level Hamiltonian

In the far-detuned limit ($\Delta \gg$ the optical pulse width), the populations of the two excited states can be adiabatically eliminated [137] and Eq. 4.3 reduces to an effective 2-level Hamiltonian describing coherent rotations of the electron spin.

A state $|\Psi(t)\rangle = a_1(t)|\downarrow\rangle + a_2(t)|\uparrow\rangle + a_3(t)|\Downarrow\uparrow\downarrow\rangle + a_4(t)|\Uparrow\uparrow\downarrow\rangle$ evolves according to

$$\frac{d|\Psi(t)\rangle}{dt} = -iH(t)|\Psi(t)\rangle. \tag{4.4}$$

The equations of motion for the coefficients can be written as

$$ia_3\Omega_{13} + ia_4\ \Omega_{14} = \dot{a_1} \tag{4.5}$$

$$-ia_2 w_e + ia_3\Omega_{23} + ia_4\Omega_{24} = \dot{a_2} \tag{4.6}$$

$$ia_1\Omega_{13}^* + ia_2\ \Omega_{23}^* - ia_3\Delta = \dot{a_3} \tag{4.7}$$

$$ia_1\Omega_{14}^* + ia_2\Omega_{24}^* - ia_4(\Delta + w_h) = \dot{a_4} \tag{4.8}$$

in which $\Omega_{ij}(t)$ and $a_i(t)$ are time dependent.

If the pulse is far detuned from the donor-bound exciton transition energy , then $\dot{a_3} \ll a_3\Delta$ and $\dot{a_4} \ll a_4\Delta$. By setting $\dot{a_3}$ and $\dot{a_4}$ to zero in Eqs. 4.7 and 4.8, we find

$$a_3 = \frac{\Omega_{13}^*}{\Delta}a_1 + \frac{\Omega_{23}^*}{\Delta}a_2 \tag{4.9}$$

$$a_4 = \frac{\Omega_{14}^*}{w_h + \Delta}a_1 + \frac{\Omega_{24}^*}{w_h + \Delta}a_2 \tag{4.10}$$

Inserting Eqs. 4.9 and 4.10 back into Eqs. 4.5 and 4.6 yields the effective 2-level Hamiltonian

$$H_{\text{eff}}(t) = \begin{pmatrix} -\frac{|\Omega_{31}(t)|^2}{4\Delta} - \frac{|\Omega_{41}(t)|^2}{4(\Delta+\omega_h)} & 0 \\ 0 & -\frac{|\Omega_{32}(t)|^2}{4\Delta} - \frac{|\Omega_{42}(t)|^2}{4(\Delta+\omega_h)} + \omega_e \end{pmatrix} + \begin{pmatrix} 0 & \frac{-\Omega_{\text{eff}}(t)}{2} \\ \frac{-\Omega_{\text{eff}}^*(t)}{2} & 0 \end{pmatrix} \tag{4.11}$$

where $\Omega_{\text{eff}}(t) = \frac{\Omega_{13}(t)\Omega_{23}^*(t)}{2\Delta} + \frac{\Omega_{14}(t)\Omega_{24}^*(t)}{2(\Delta+\omega_h)}$ is the effective Rabi frequency.

In our experiment, the polarization of the laser is adjusted so that $\Omega_{13} = \Omega_{23} = \Omega_{14} = \Omega_{24} = \Omega_R$. In the rotation frame of the electron spin (frequency ω_e), the ZnO donor effective Hamiltonian is then given by

$$H_{\text{eff}}(t) = \begin{pmatrix} 0 & \frac{\Omega_{\text{eff}}(t)}{2}e^{-i\omega_e t} \\ \frac{\Omega_{\text{eff}}^*(t)}{2}e^{i\omega_e t} & 0 \end{pmatrix}, \tag{4.12}$$

where $\Omega_{\text{eff}} = \frac{|\Omega_R|^2}{2}(\frac{1}{\Delta} + \frac{1}{\Delta+\omega_h})$ is the effective Rabi frequency. The axis of the rotation is determined by the timing of the pulse due to the $e^{\pm i\omega_e t}$ terms in H_{eff}. However, this model does not account for dephasing nor relaxation. Therefore for quantitative analysis, a 4-level model needs to be used.

4.5.2 Master equation of 4-level density matrix model

While the 2-level model provides intuition for how a single optical pulse coherently rotates the spin, it does not consider decoherence or relaxation. To analyze the dynamics of the density matrix in a more accurate way, we use the full 4-level master equation with decoherence and relaxation taken into consideration, i.e. $\partial\rho/\partial t = -i[H, \rho] + L(\rho)$, where $L(\rho)$ is the Lindblad operator.

$$L(\rho) = \begin{pmatrix} -\Gamma_{12}\rho_{11} + \Gamma_{21}\rho_{22} + \Gamma_{31}\rho_{33} + \Gamma_{41}\rho_{44} & -(\frac{\Gamma_{12}+\Gamma_{21}}{2} + \gamma_{12})\rho_{12} & -(\frac{\Gamma_{12}+\Gamma_{31}+\Gamma_{32}+\Gamma_{34}}{2} + \gamma_{13})\rho_{13} & -(\frac{\Gamma_{12}+\Gamma_{41}+\Gamma_{42}+\Gamma_{43}}{2} + \gamma_{14})\rho_{14} \\ -(\frac{\Gamma_{21}+\Gamma_{12}}{2} + \gamma_{12})\rho_{21} & \Gamma_{12}\rho_{11} - \Gamma_{21}\rho_{22} + \Gamma_{32}\rho_{33} + \Gamma_{42}\rho_{44} & -(\frac{\Gamma_{21}+\Gamma_{31}+\Gamma_{32}+\Gamma_{34}}{2} + \gamma_{23})\rho_{23} & -(\frac{\Gamma_{21}+\Gamma_{41}+\Gamma_{42}+\Gamma_{43}}{2} + \gamma_{24})\rho_{24} \\ -(\frac{\Gamma_{31}+\Gamma_{32}+\Gamma_{34}+\Gamma_{12}}{2} + \gamma_{13})\rho_{31} & -(\frac{\Gamma_{31}+\Gamma_{32}+\Gamma_{34}+\Gamma_{21}}{2} + \gamma_{23})\rho_{32} & -(\Gamma_{31} + \Gamma_{32} + \Gamma_{34})\rho_{33} + \Gamma_{43}\rho_{44} & -(\frac{\Gamma_{31}+\Gamma_{32}+\Gamma_{34}+\Gamma_{41}+\Gamma_{42}+\Gamma_{43}}{2})\rho_{34} \\ -(\frac{\Gamma_{41}+\Gamma_{42}+\Gamma_{43}+\Gamma_{12}}{2} + \gamma_{14})\rho_{41} & -(\frac{\Gamma_{41}+\Gamma_{42}+\Gamma_{43}+\Gamma_{21}}{2} + \gamma_{24})\rho_{42} & -(\frac{\Gamma_{41}+\Gamma_{42}+\Gamma_{43}+\Gamma_{31}+\Gamma_{32}+\Gamma_{34}}{2})\rho_{43} & -(\Gamma_{41} + \Gamma_{42} + \Gamma_{43})\rho_{44} + \Gamma_{34}\rho_{33} \end{pmatrix} \tag{4.13}$$

Γ_{ij} is the population relaxation rate from $|i\rangle \to |j\rangle$ and γ_{ij} is the rate of dephasing between $|i\rangle \leftrightarrow |j\rangle$.

We fit for the relationship between $\Omega_{\mathrm{R}}(t)$ and pulse energy using $P = \alpha \cdot \max|\Omega_{\mathrm{R}}(t)|^2$, where P is the pulse energy, α is a fit parameter, and $\max|\Omega_{\mathrm{R}}(t)|^2$ is the peak value of $|\Omega_{\mathrm{R}}(t)|^2$ where we have assumed a Gaussian time dependence. Autocorrelation measurements of the infrared laser pulse find a pulse width of 1.9 ps; however, after second harmonic generation where $I_{\mathrm{UV}}(2\omega) \propto I_{\mathrm{IR}}^2(\omega)$, we estimate that the ultra violet laser pulse is compressed to $1.9/\sqrt{2}$ ps.

$\gamma_{13} = \gamma_{23} = \gamma_{14} = \gamma_{24} = \gamma$ is the dephasing between the excited states and the ground states. Due to laser-induced dephasing, we fit for $\gamma = \beta_1\Omega_R(t) + \beta_2\Omega_R^2(t)$ where β_1 and β_2 are fit parameters. $\Gamma_{31} = \Gamma_{42} = 0.5\Gamma_{\mathrm{rad}}$ and $\Gamma_{32} = \Gamma_{41} = 0.5\Gamma_{\mathrm{rad}}$ are the radiative decay rates from the excited states to the ground states. We let $\Gamma_{12} = \Gamma_{21} = \Gamma_{34} = \Gamma_{43} = 0$, because these decay rates are slow compared to the other time scales in this system. Parameters used for the fit of experimental data in Fig. 4.5 are given in Table 4.1.

4.5.3 Experimental data

To generate a coherent superposition of the ground spin states, we first optically pump the donors to $|\downarrow\rangle$. We next apply an ultra-fast control pulse obtained by frequency doubling an 1.9 ps pulse generated from a mode-locked Ti:Sapphire laser. The population $\mathrm{P}_\uparrow$ is

Parameter	Value	Description
ω_e	$2\pi \times 138$ GHz[a]	ground state frequency splitting, $\omega_e = g_e \mu_B B/\hbar$
ω_h	$2\pi \times 24$ GHz[a]	excited state frequency splitting, $\omega_h = g_h \mu_B B/\hbar$
Δ	$2\pi \times 3570$ GHz[b]	detuning between pulsed laser and $\vert\downarrow\rangle \Leftrightarrow \vert\Downarrow\uparrow\downarrow\rangle$
Γ_{rad}	1 GHz [118]	$1/T_{\mathrm{rad}}$, T_{rad} is the radiative lifetime
γ_{12}	5×10^{-5} GHz[c]	$1/T_2$
α	7.2×10^{-6} pJ GHz^{-2} [d]	$\mathrm{P} = \alpha \cdot \max\vert\Omega_{\mathrm{R}}(t)\vert^2$
β_1	6.6 [d]	$\gamma = \beta_1 \Omega_R + \beta_2 \Omega_R^2$
β_2	3.3×10^{-3} GHz^{-1} [d]	$\gamma = \beta_1 \Omega_R + \beta_2 \Omega_R^2$

Table 4.1: Parameters used for the simulation.

[a] Derived from the electron and hole g-factors, g_e and g_h respectively, measured using the data in Fig. 4.1(c)
[b] Experimental parameter
[c] T_2 measured from the data in Fig. 4.6
[d] Fit from the data in Fig. 4.5

measured by the subsequence cw pumping pulse. Figure 4.5(a) shows the dependence of $|\uparrow\rangle$ population after the ultrafast pulse as a function of the pulse energy. We attribute the saturation of the population transfer at high pulse powers to laser-induced dephasing between the D^0X states and the D^0 states. At high power, the coherence between the excited states and the ground states decays much faster than the pulse duration. In this high power regime, the ultra-fast pulse can no longer coherently drive the transition between the two spin states and a saturation in the population curve is observed. While the mechanism for this dephasing is unknown, one possibility is the unintentional excitation of real carriers.

Due to the laser-induced dephasing, coherent rotations are only expected at low pulse energy. The coherence of the small-angle rotation can be probed via Ramsey interferometry. Standard Ramsey experiments are done by measuring the spin population after two $\pi/2$ pulses with variable delay between them. An oscillation of the spin population as a function of the delay time can be observed due to the Larmor precession of the electron spin. Though only small-angle rotations are accessible in our system, they can also produce Ramsey interference, albeit with smaller oscillation amplitude. A representative Ramsey fringe using small-angle rotations is shown in Fig. 4.5(b). The fit oscillation frequency in Fig. 4.5(b) is 136 ± 3 GHz at 5 T, which matches the predicted 137.9 ± 0.7 GHz using the measured

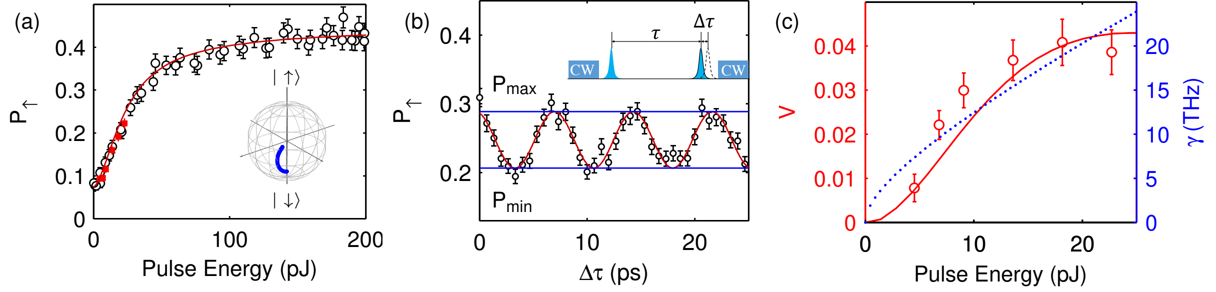

Figure 4.5: (a) $P_\uparrow$ (population of $|\uparrow\rangle$) as a function of the single-pulse energy with spin initialized to $|\downarrow\rangle$ and then excited by the ultra-fast pulse. Error bars show the 1σ uncertainty from the Poisson noise in PL collection. Data points represented by red squares at low powers are taken at the same power as data points in **c**. The red curve is a simultaneous least squares fit for data in **a** and **c**. The inset shows how the state changes in the Bloch sphere using the simulated results. (b) A typical Ramsey interference pattern with 18 pJ pulse energy. The inset shows the laser sequence, where τ is the delay between the two pulses ($\tau = 0.8$ ns in this data). The first cw pulse initializes the spin and the second cw pulse is to used to read out. (c) The Ramsey fringe amplitude V = $(P_{\max}$ - $P_{\min})/2$ as a function of the single pulse energy. Error bars show the 1σ uncertainty from the sinusoid fit of the Ramsey oscillation. The red line is the simulation result from the simultaneous fit. The blue dotted line shows the fit parameter γ (excited state dephasing rate) as a function of pulse energy. For these data, the excitation spot size is ∼2 µm, the collection spot size is ∼0.6 µm. The temperature is at 1.5 K and the magnetic field is at 5 T. The ultra-fast pulses are detuned by $\Delta/2\pi = 3.57$ THz from the transition $|\downarrow\rangle \Leftrightarrow |\Downarrow\uparrow\downarrow\rangle$.

electron g-factor. The Ramsey fringe amplitude as a function of the pulse energy is shown in Fig. 4.5(c). A least squares fit based on the 4-level density matrix model is used to fit the data in Fig. 4.5(a) and (c) simultaneously. An empirical relationship between $\Omega_R(t)$ and the laser-induced dephasing rate γ is used in the fit, i.e. $\gamma = \beta_1\Omega_R(t) + \beta_2\Omega_R^2(t)$, where $\beta_{1,2}$ are the fitting parameters. The other fit parameter is α which relates the optical Rabi frequency $\Omega_R(t)$ and physical pulse energy $\mathrm{P} = \alpha \cdot \max|\Omega_\mathrm{R}(t)|^2$.

Ultra-fast optical spin-control is a powerful tool to probe the coherence of the electron spins and measure the coherence time, however long-term it will be necessary to achieve high fidelity full-angle control for quantum applications. A possible solution is to utilize spin-resonant microwave fields, which has been successfully demonstrated in NV centers and donors in Si. For practical devices in ZnO, we must decrease our magnetic field such that

the electron Zeeman splitting of the ground states is less than 10 GHz. This is difficult in our current sample due to the large inhomogeneous optical linewidth which makes optical pumping inefficient at lower magnetic fields. This challenge can be overcome with higher purity samples or single donor isolation.

4.6 T_2^* and T_2 measurement

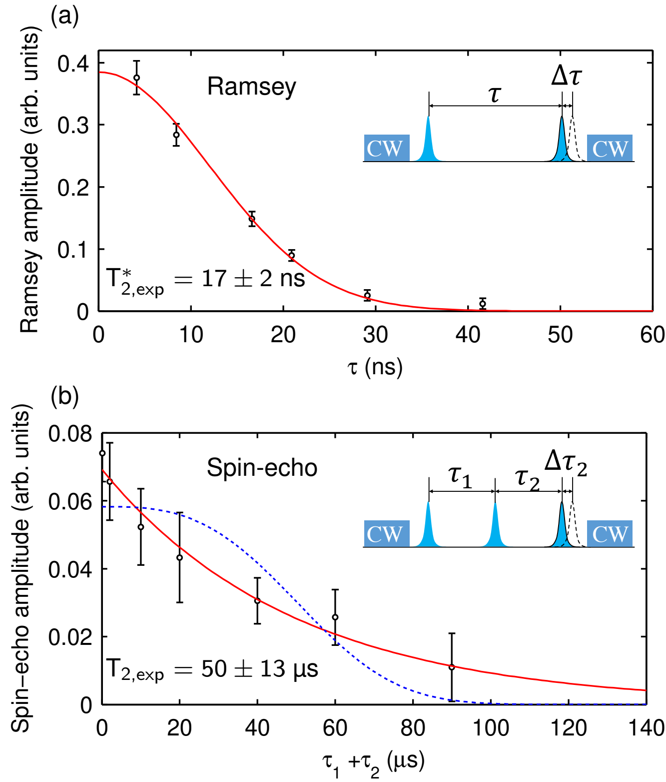

Figure 4.6: (a) The Ramsey fringe amplitude as a function of delay time τ. The red curve shows a fit to $\exp(-(\tau/T_2^*)^2)$, giving $T^*_{2,\text{exp}} = 17 \pm 2$ ns. (b) Spin-echo measurement of the dephasing time T_2. The delay $\tau_1 \simeq \tau_2$. Oscillations are observed by changing $\Delta\tau_2$. The oscillation amplitude is measured as a function of $\tau_1 + \tau_2$. The red curve shows a fit to $\exp(-\frac{\tau_1+\tau_2}{T_2})$, giving $T_{2,\text{exp}} = 50 \pm 13$ μs. For comparison, the blue dashed line shows a fit to $\exp(-(\frac{\tau_1+\tau_2}{T_2})^3)$, the expected form for spectral diffusion. For these data, both the excitation and collection spot sizes are ~0.6 μm. The temperature is at 5.5 K and the magnetic field is at 5 T. The ultra-fast pulses are detuned by $\Delta/2\pi = 0.9$ THz from the transition $|\downarrow\rangle \Leftrightarrow |\Downarrow\uparrow\downarrow\rangle$.

T_2^* is extracted from the decay of the Ramsey fringe amplitude as a function of the pulse delay time, as shown in Fig. 4.6(a). A fit for data in Fig. 4.6(a) using $\exp(-(\tau/T_2^*)^2)$ gives $T_{2,\mathrm{exp}}^* = 17 \pm 2$ ns, which is consistent with prior studies [138, 139]. This dephasing time originates from the inhomogeneous nuclear field due to the hyperfine interaction between electrons and lattice nuclear spins. For the Ga donors in ZnO, this includes the hyperfine interaction from both the Ga nucleus and the ^{67}Zn nuclei. T_2^* can be estimated from the dispersion of the hyperfine field Δ_B with $T_2^* = \hbar/g_e\mu_B\Delta_B$ [140]. As only one Ga nucleus is in the effective wave function of the electron bound to the donor, the effective field from Ga has 4 different values due to 3/2 nuclear spin of Ga:

$$B_{\mathrm{Ga}} = \frac{2\mu_0}{3g_e}\frac{\mu_{\mathrm{Ga}}}{I_{\mathrm{Ga}}}|u_{\mathrm{Zn}}|^2|\psi(0)|^2 \times \{\frac{3}{2}, \frac{1}{2}, -\frac{1}{2}, -\frac{3}{2}\}. \tag{4.14}$$

The hyperfine field due to numerous ^{67}Zn nuclei is estimated to have a Gaussian distribution $\exp(-B^2/\Delta_{B,\mathrm{Zn}}^2)$, where $\Delta_{B,\mathrm{Zn}}$ is calculated in Ref. [140]:

$$\Delta_{B,\mathrm{Zn}} = \frac{\mu_0\mu_{\mathrm{Zn}}}{g_e}\sqrt{\frac{32}{27}}\sqrt{\frac{I_{\mathrm{Zn}}+1}{I_{\mathrm{Zn}}}}|u_{\mathrm{Zn}}|^2\sqrt{f\sum_j|\psi(\vec{R}_j)|^4}, \tag{4.15}$$

In Eqs. 4.14 and 4.15, μ_B is the Bohr magneton, g_e is the electron g-factor, μ_0 is the vacuum permeability. $I_{\mathrm{Zn}} = 5/2$ ($I_{\mathrm{Ga}} = 3/2$) is the nuclear spin of ^{67}Zn (Ga), $\mu_{\mathrm{Zn}} = 0.874\mu_N$ ($\mu_{\mathrm{Ga}} = 2.24\mu_N$) is the nuclear magnetic moment of ^{67}Zn (Ga) and μ_N is the nuclear magneton. $f = 4.1\%$ is the natural abundance of ^{67}Zn. $\psi(\vec{R}_j)$ ($\psi(0)$) is the hydrogenic effective-mass envelope wave function of electron at the jth Zn (Ga) lattice site. $|u_{\mathrm{Zn}}|^2$ is the ratio of Bloch function density at the Zn site to the average Bloch function density. From electron spin resonance measurements in ZnO [121], $|u_{\mathrm{Zn}}|^2 \simeq 1120$. Using the effective mass Bohr radius $a_{\mathrm{B}} \simeq 1.7$ nm and by combining the hyperfine interactions from both Ga and ^{67}Zn, we find $T_{2,\mathrm{theory}}^* \simeq 9$ ns, as shown in Fig. 4.7. This estimation is close to our experimental result. Moving to isolated single donors in isotope-purified ZnO can eliminate this dephasing mechanism.

We next apply a spin echo sequence to suppress the effect of the inhomogeneous nuclear field. A standard spin echo includes two $\pi/2$ pulses separated by one π pulse. It has

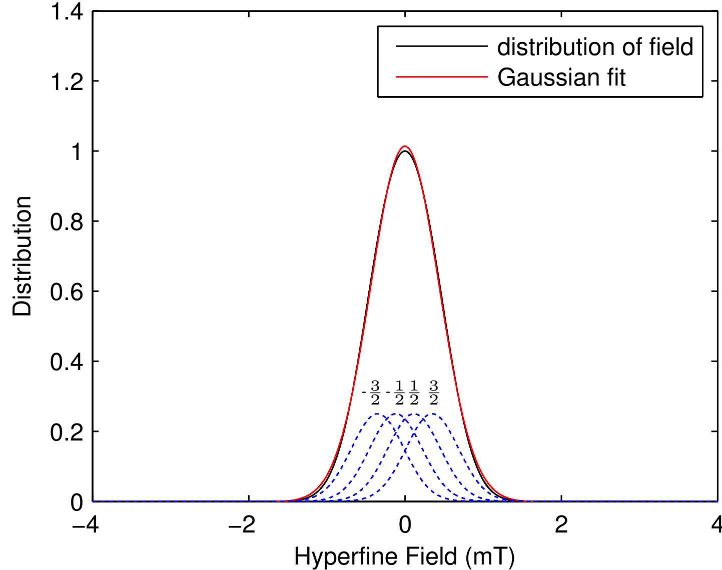

Figure 4.7: The 4 dashed curves show the distribution of the hyperfine field with Ga in the four different nuclear spin states, i.e. $m_{Ga} = \{\frac{3}{2}, \frac{1}{2}, -\frac{1}{2}, -\frac{3}{2}\}$. The black line is the distribution of the hyperfine field combining the contributions from both Ga and ^{67}Zn. In the combination, the nuclear spin states are assumed to be equally distributed in the 4 spin states as the nuclear splitting is much smaller than the thermal energy. The red curve is a fit using a Gassian form e^{-B^2/Δ_B^2}, where the dispersion Δ_B is used to estimate T_2^* with $T_2^* = \hbar/g_e\mu_B\Delta_B$.

been shown that three small angle rotations have a similar effect but with a smaller echo signal [11]. The measured spin-echo decoherence time is $T_{2,\text{exp}} = 50 \pm 13$ μs using an exponential fit, as shown in Fig. 4.6(b). Possible mechanisms limiting T_2 are instantaneous diffusion and spectral diffusion.

Instantaneous diffusion (ID) is the decoherence caused by the refocusing pulse in the spin-echo sequence. During the refocusing pulse, the dipole-coupled electron spins bound to different donors all rotate with the same angle. Therefore, the energy of this dipole-dipole interaction doesn't flip sign after the refocusing pulse and the phase cannot be corrected.

The decay of the signal follows an $\exp(-t/\mathrm{T}_{2,\mathrm{ID}})$ with $\mathrm{T}_{2,\mathrm{ID}}$ given by [141, 142]

$$1/\mathrm{T}_{2,\mathrm{ID}} = \frac{\mu_0 (g_e \mu_B)^2 N_{\mathrm{Ga}}}{9\sqrt{3}\pi\hbar} \sin^2 \frac{\theta_2}{2} \tag{4.16}$$

where N_{Ga} is the density of Ga donors and θ_2 is the rotation angle of the refocusing pulse. Due to the comparable excitation and collection spot sizes in the experiment, the rotation angle varies across the collection spot making an accurate estimation of θ_2 challenging. A reasonable range of θ_2 is $\pi/5 \sim \pi/2$. While the Ga concentration is uncertain, ESR measurements of a similar substrate indicate a shallow donor concentration of $\simeq 10^{16}$ cm^{-3} [143]. Using this estimate, $\mathrm{T}_{2,\mathrm{ID}}$ ranges from 240 µs to 1.27 ms. It is also possible that the refocusing pulse incoherently alters the local spin environment due to charge transfer between deeper paramagnetic centers (e.g. Li) [143] causing additional dephasing.

Spectral diffusion (SD) of the electron spin energy can occur due to flip-flops of dipole-coupled ^{67}Zn nuclear spins. The measured $\mathrm{T}_{2,\mathrm{exp}}^{\mathrm{ZnO}}$ is of similar magnitude to T_2 measured for phosphorous donors in natural Si [144, 145], which is limited by this spectral diffusion mechanism. Considering the similar isotope composition between ZnO and Si, we expect spectral diffusion to also be significant in ZnO. We estimate $\mathrm{T}_{2,\mathrm{SD}}$ with a stochastic model developed for phosphorous donors in Si [146]. Assuming a Gaussian diffusion kernel, the decay of the signal exhibits an $\exp(-(t/\mathrm{T}_{2,\mathrm{SD}})^3)$ dependence with $\mathrm{T}_{2,\mathrm{SD}}$ given by

$$1/\mathrm{T}_{2,\mathrm{SD}} \simeq \left[\frac{8\pi}{27\sqrt{3}\hbar} \mu_0 \mu_{\mathrm{Zn}} g_e \mu_B n \Sigma_j b_j^2\right]^{1/3}, \tag{4.17}$$

$$\Sigma_j b_j^2 = f \frac{\mu_0^2}{16\pi^2} \frac{\mu_{\mathrm{Zn}}^4}{\hbar^2} \Sigma_j \frac{(1 - 3\cos^2\theta_j)^2}{r_j^6}, \tag{4.18}$$

where n is the density of ^{67}Zn. For a given ^{67}Zn nucleus, b_j is the dipole-dipole interaction between it and the jth ^{67}Zn. r_j is the distance between the two nuclei and θ_j is the angle between $\vec{r}_j$ and the B-field. Using Eq. 4.17, we estimate $\mathrm{T}_{2,\mathrm{SD}} \simeq 200$ µs.

The magnitude of T_2 estimated by both mechanisms is in reasonable agreement with $\mathrm{T}_{2,\mathrm{exp}}$. While we find better agreement in the experimental decay shape with the instantaneous diffusion mechanism, as shown in Fig. 4.6(b), it is still hard to confirm the dominant

mechanism considering the low signal-to-noise ratio and since the dependence of T_2 on different parameters has not been measured. To rigorously determine the mechanism, future experiments will be conducted to measure the dependence of T_2 on the abundance of ^{67}Zn [147], donor density [126], rotation angle of the rephasing pulse [142] and magnetic field direction [144]. The determination of the mechanism is important as this can be generalized to other II-VI materials, thus aiding in the search for superior defect-based qubit candidates. Regardless of which mechanism dominates T_2 in ZnO, practical devices will require both isotope purification and lower donor densities.

4.7 Conclusions

In summary, we demonstrate optical spin control and read-out of Ga donor qubits in a bulk ZnO crystal. Long spin relaxation times (100 ms) and coherence times (50 µs) are observed. These promising results motivate future work on the challenges toward making a practical quantum network out of optically-active donor qubits. In the ZnO donor platform, these challenges include chemical and isotope purification of the sample, high fidelity microwave control of the spin state, and single donor isolation. Thin films grown by molecular beam epitaxy have shown orders of magnitude lower impurity concentration than commercial ZnO substrates [127]. Devices incorporating such high-purity layers will be essential for addressing all three challenges. In the near-term, single donor isolation for fundamental studies can be achieved in nanostructures fabricated by focused ion beam milling [148] or utilizing single nanowires [149]. In the long term, scalable device integration will require pushing ZnO fabrication techniques beyond the standard micro-fabrication techniques currently developed for ZnO [120, 150].

Chapter 5

PROGRESS TOWARDS SINGLE DONOR ISOLATION WITH FOCUSED ION BEAM IN ZNO

5.1 Introduction

All the measurements done in the last chapter are on ensemble of donors. The studied sample is a Tokyo Denpa substrate with a 0.7 µm ZnO epitaxial layer on the top surface. The Tokyo Denpa substrate has a Ga donor density of $\sim 10^{16}$ cm^{-3} and the donor density in the epitaxial layer is $\sim 10^{15}$ cm^{-3}. Most of the PL signal comes from the substrate. For ~ 1 µm spot size (the optical resolution of the microscope setup), there are about 2×10^4 Ga donors in the optical spot. However, to utilize the photon-based entanglement protocol, it is necessary to use single donors. Single donor isolation can be achieved in an ultra-pure ZnO crystal with small donor density ($\sim 10^{12}$ cm^{-3}) but we are not able to get such high-purity sample at this moment. To isolate single donors in our current sample, there are two possible methods: using optical techniques and using physical isolation.

Super-resolution techniques such as ground state depletion (GSD) [151] can possibly be adopted in the donor system to reduce the optical resolution and isolate single donors. In GSD, the super-resolution is achieved by first using a donut-shaped beam to pump the donors inside the donut beam into a different spin state. For the donors in the middle of the donut, they remains at the initial spin state. Then, a Gaussian-shaped beam is applied to the sample and the laser energy is tuned to only excite those donors in the middle of the donut. Depending on the power of the laser, nm-resolution can be achieved. For the donor density of 10^{16} cm^{-3}, a spot size of 100 nm is needed to isolate a single donor which can be achieved by the GSD technique. However, this method requires near perfect optical pumping efficiency and we are not able to achieve that in our ZnO sample especially at high power. Another possible optical technique to isolate single donor is utilizing the inhomogeneous broadening of donors. The optical transition of different donors has different

energy so potentially we can selectively excite a single donor with a narrow-linewidth laser. This idea can be used in quantum dots which could have large inhomogenous broadening up to thousands of GHz [152]. However, in the donor system, the inhomogenous linewidth is only about 20 GHz and the homogeneous linewidth is about 0.2 GHz. With 2×10^4 donors in the optical spot, it is hard to isolate single donors by energy selectivity.

The idea of physical isolation is to isolate single donors by reducing the volume of the ZnO crystal. This can be accomplished by growing thin ZnO nanowires [153, 149] or fabricating thin ZnO films with focused ion beam (FIB) [148, 154]. Compared to the nanowire method, FIB provides higher flexibility on controlling the dimension and shape of the structures. In this chapter, we fabricate multiple ZnO thin films with FIB and perform PL measurements on them. The ZnO thin films are milled from three different samples: Tokyo Denpa substrate with 0.7 µm ZnO epitaxial layer, Tokyo Denpa substrate with 3 µm ZnO epitaxial layer, and bare Tokyo Denpa substrate. We have made four different FIB thin films from the three samples. From the 0.7 µm epilayer sample, we make a FIB thin film that contains both the 0.7 µm epilayer and the Tokyo Denpa substrate. From the 3 µm epilayer sample, we make two FIB thin films that are purely from the epilayer. These two thin films allow us to directly look at the PL from the epilayer, which we are not able to achieve in the two bulk epilayer samples. For the bare Tokyo Denpa substrate, we make a FIB thin film that is purely from the substrate. Though single donor isolation is not achieved in the thin films, the measurements show how FIB modify the PL compared with the bulk crystal. This PL study can give a guide on the future research to utilize FIB on single donor isolation. In the PL study, a PL quenching effect is observed in all of the four FIB thin films. The origin of this effect is still unknown and needs to be studied in the future.

5.2 Thin film fabrication with FIB

We utilize the FEI XL830 Dual Beam FIB/SEM for the FIB fabrication. This dual beam workstation uses 30 keV Ga ions for nano-milling. We have developed two different routines to fabricate the thin film: top milling and side milling (see Appendix B for details). We have made four different ZnO thin films with FIB, as shown in Fig. 5.1.

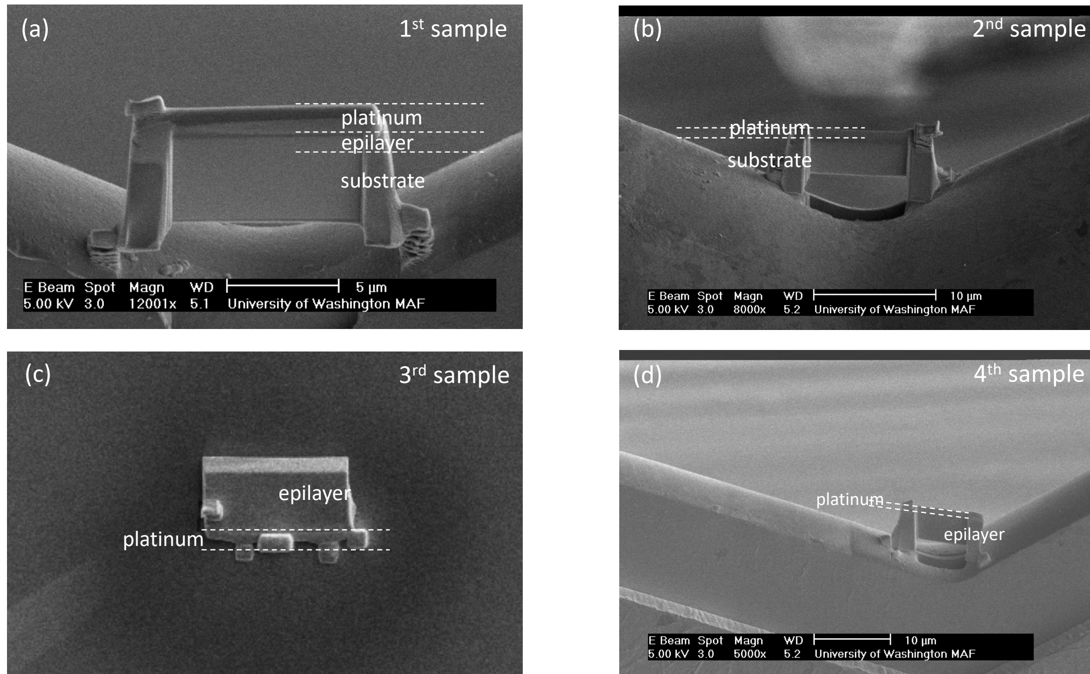

Figure 5.1: SEM images of the four FIB ZnO thin films. The constitution of the thin films is labeled in the images. For the SEM image on the 3rd sample, though the scale bar was not saved, the sample size is ∼10 µm, similar to the other three.

- The 1st thin film: The thin film is made from the Tokyo Denpa substrate with 0.7 µm epilayer using the top milling method. The thin film is transferred to a metal grid at the end of the fabrication. In the thin film, at the top side, there are an ∼1 µm platinum layer and 0.7 µm epilayer. The other part is from the Tokyo Denpa substrate. The thickness of this thin film is around 0.8 µm.
- The 2nd thin film: The thin film is made from a bare Tokyo Denpa substrate using the top milling method. The thin film is transferred to a metal grid at the end of the fabrication. In the thin film, there is an ∼1 µm platinum layer at the top side and the other part is from the Tokyo Denpa substrate. The thickness of this thin film is around 0.4 µm.
- The 3rd thin film: The thin film is made from the Tokyo Denpa substrate with 3 µm epilayer using the side milling method. The thin film is transferred to a Si substrate at the end of the fabrication. In the thin film, at one side, there is an ∼1 µm platinum

layer. The other part is from the epitaxial layer. The thickness of this thin film is around 1 µm.

- The 4th thin film: The thin film is made from the Tokyo Denpa substrate with 3 µm epilayer using the side milling method. The thin film is transferred to a metal grid at the end of the fabrication. In the thin film, at the top side, there is an ∼1 µm platinum layer. The other part is from the epitaxial layer. The thickness of this thin film is around 0.4 µm.

5.3 PL measurements on the four FIB thin films

In this section, we show the results of the PL measurements on the four FIB thin films. The PL of the thin films are studied using a home-built confocal microscope with a ∼0.7 µm resolution. Because of the high donor density in both the Tokyo Denpa substrate ($\sim 10^{16}$ cm^{-3}) and the epitaxial layer ($\sim 10^{15}$ cm^{-3}), to isolate single donors, the thickness of the thin film needs to be less than 10 nm. As the thickness of the four FIB thin films is 0.4 to 1 µm, we are not able to observe single donors. Even though single donor isolation is not achieved, this PL study shows how the ion beams affect the PL properties in the thin films and can guide the future research that utilizes FIB on ZnO crystals.

5.3.1 PL measurements on the 1st thin film

Figure 5.2 shows the PL measurements on the 1st thin film. This thin film contains a ∼1 µm platinum layer and 0.7 µm epilayer at the top side and the other part is from the Tokyo Denpa substrate. As shown in Fig. 5.2(b), in the top ∼1.5 µm region of the sample, the PL is completely quenched, i.e. zero PL signal in this region. Because of this quenching effect, we are not able to get the PL spectra from the epilayer in this sample but we note that we can see signals from the epilayers in the 3rd and 4th samples, as shown in Sec. 5.3.3 and Sec. 5.3.4. In the other regions, the PL spectra are different at different spots. Figure 5.2(c) shows the comparison between the PL spectrum from the bulk sample and the PL spectra at two spots on the FIB thin film. At the red spot (spot 1), the PL spectrum has two sharp peaks from the Ga and Al donors, similar to the bulk sample. There is a shift of the energy and the ratio between the two peaks is also different from the bulk sample. The

broad bands between 367 nm and 368.7 nm in the bulk sample are not observed in the FIB sample. The origin of those broad bands is still unclear. At the blue spot (spot 2), the peak is broader, and the Ga and Al peaks cannot be resolved. The location dependence of the PL spectra could be due to inhomogeneous strain across the sample.

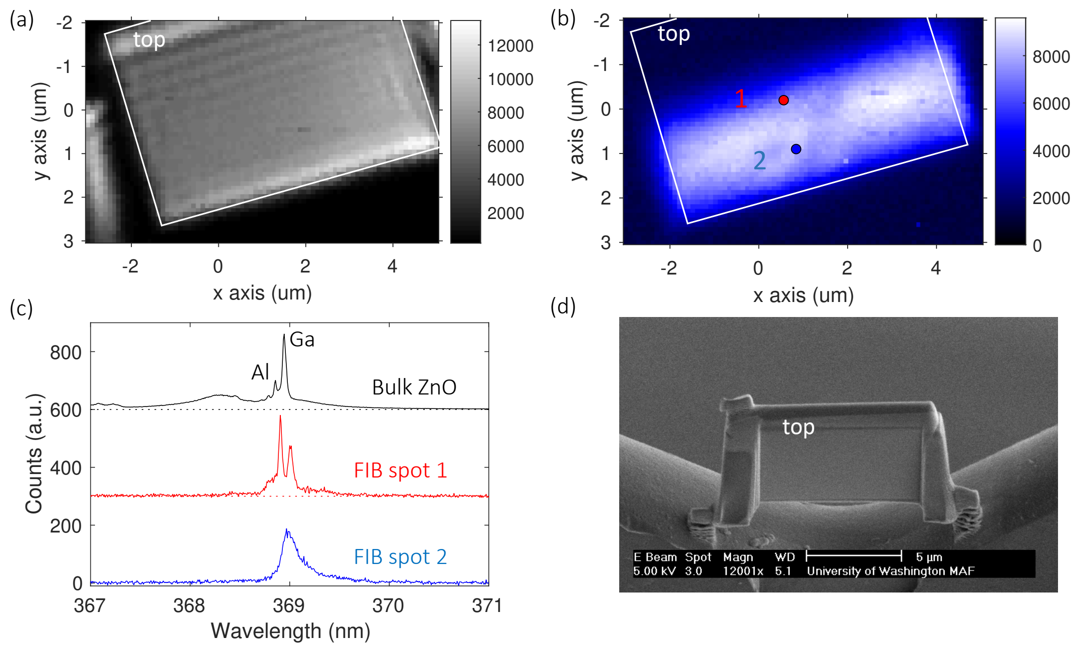

Figure 5.2: PL measurements on the 1st FIB thin film. (a) Confocal scan collecting the laser reflection. The white frame shows where the thin film is. (b) PL confocal scan at 8 K and 0 T. The white frame shows where the thin film is. (c) The spectra at the two spots marked in **b** with red and blue circles. A spectrum from the bulk sample (black curve) is plotted as a comparison. Excitation at ∼360 nm. The bulk sample is at ∼11 K with 90 nW excitation power. The FIB thin film is at ∼8 K with 250 nW excitation power. The intensity of the bulk spectrum is scaled to match with the spectra from the FIB sample. (d) The SEM image of the thin film. The top side of the sample is marked as “top” in **a**, **b** and **d**.

5.3.2 PL measurements on the 2nd thin film

Figure 5.3 shows the PL measurements on the 2nd thin film. This thin film contains a ∼1 µm platinum layer at the top side and the other part is from the Tokyo Denpa substrate. Similar to the 1st sample, in the top ∼2 µm region, the PL is quenched. In the other regions, the PL spectra also have a location dependence. Figure 5.2(c) shows the comparison between the PL spectrum from the bulk sample and the PL spectra at three different spots on the FIB thin film. At the yellow spot (spot 1), the Ga and Al donor peaks can be identified but they are broader than the bulk sample, and there is also a shift in the energy. At the other two spots, the peaks are much broader, and the Ga and Al peaks cannot be resolved. We are not able to observe spectra with sharp peaks similar to the spot 1 in the 1st thin film. The broader linewidth in this thin film might be due to the smaller thickness thus larger inhomogeneous strain. The thickness of this thin film is ∼0.4 µm while the thickness of the 1st thin film is ∼0.8 µm.

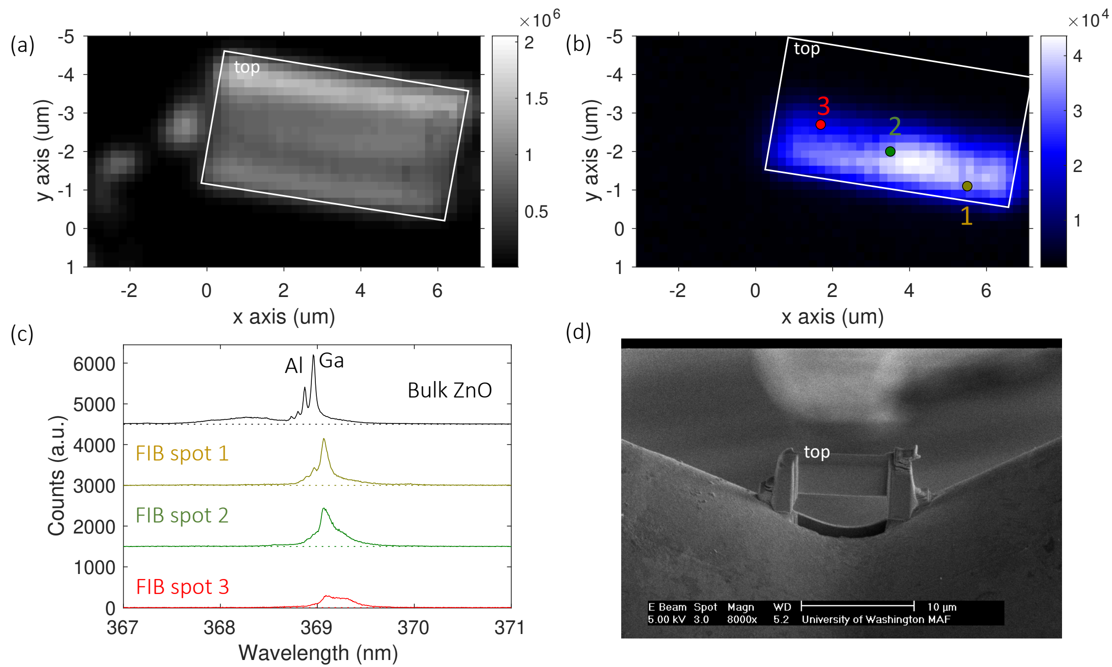

Figure 5.3: PL measurements on the 2nd FIB thin film. (a) Confocal scan collecting the laser reflection. The white frame shows where the thin film is. (b) PL confocal scan at 7.8 K and 0 T. The white frame shows where the thin film is. (c) The spectra at the three spots marked in **b** with yellow, green, and red circles. A spectrum from the bulk sample (black curve) is plotted as a comparison. Excitation at ∼360 nm. The bulk sample is at ∼6 K with 90 nW excitation power. The FIB thin film is at ∼7.8 K with 5.6 µW excitation power. The intensity of the bulk spectrum is scaled to match with the spectra from the FIB sample. (d) The SEM image of the thin film. The top side of the ZnO thin film is marked as “top” in **a**, **b** and **d**.

5.3.3 PL measurements on the 3rd thin film

Figure 5.4 shows the PL measurements on the 3rd thin film. This thin film contains a ∼1 µm platinum layer at one side and the other part is from the epilayer. The thin film is transferred to a Si substrate, shown in Fig. 5.4(d). As shown in Fig. 5.4(b), the PL is only observed at the edge of the sample, probably because we are not able to do a final polishing in the fabrication process to remove the ion damage. The edge of the sample is the only region that is not directly exposed to ions. The spectra at different spots also have a large variance, as shown in Fig. 5.4(c). They all have a red shift compared to the PL from the bulk sample and the magnitude of the shift depends on the locations. The PL peaks are also much broader than the bulk sample and also the two other FIB thin films. The sharp Ga or Al donor peaks can not be resolved in this thin film.

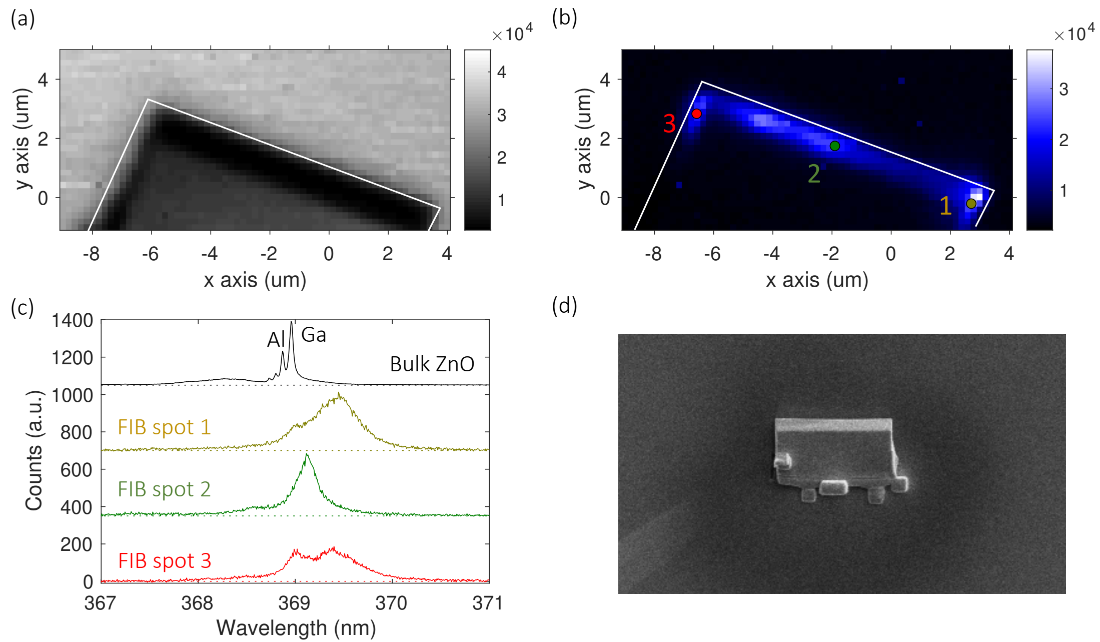

Figure 5.4: PL measurements on the 3rd FIB thin film. (a) Confocal scan collecting the laser reflection. The white frame shows where the ZnO thin film is. (b) PL confocal scan at 12 K and 0 T. The white frame shows where the ZnO thin film is. (c) The spectra at the three spots marked in **b** with yellow, green, and red circles. A spectrum from the bulk sample (black curve) is plotted as a comparison. Excitation at ∼360 nm. The Bulk sample is at ∼6 K with 90 nW excitation power. The FIB thin film is at ∼12 K with 4.5 µW excitation power. The intensity of the bulk spectrum is scaled to match with the spectra from the FIB thin film. (d) The SEM image of the thin film. The sample size is ∼1 µm.

5.3.4 PL measurements on the 4th thin film

Figure 5.5 shows the PL measurements on the 4th thin film. This thin film contains a ∼1 µm platinum layer at the top side and the other part is from the epilayer. The thin film is transferred to a metal grid, as shown in Fig. 5.5(d). Similar to the 1st and 2nd samples, in the top ∼2 µm region, the PL is quenched, as shown in Fig. 5.5(b). In the other regions, the PL spectra also have a location dependence. The spectra at different spots also have a large variance, as shown in Fig. 5.5(c). Their energy is similar to the bulk sample but the linewidth is much broader. The sharp Ga or Al donor peaks can not be resolved in this thin film.

Both the 3rd and 4th thin films are epilayer-only thin film. The PL intensity on these two samples is about 10 times weaker than the 1st and 2nd thin films in which the PL is from the Tokyo Denpa substrate. This intensity difference matches with the difference in donor density: the Ga donor density of the Tokyo Denpa substrate is about 10^{16} cm^{-3} while the donor density of the epilayer is about 10^{15} cm^{-3}.

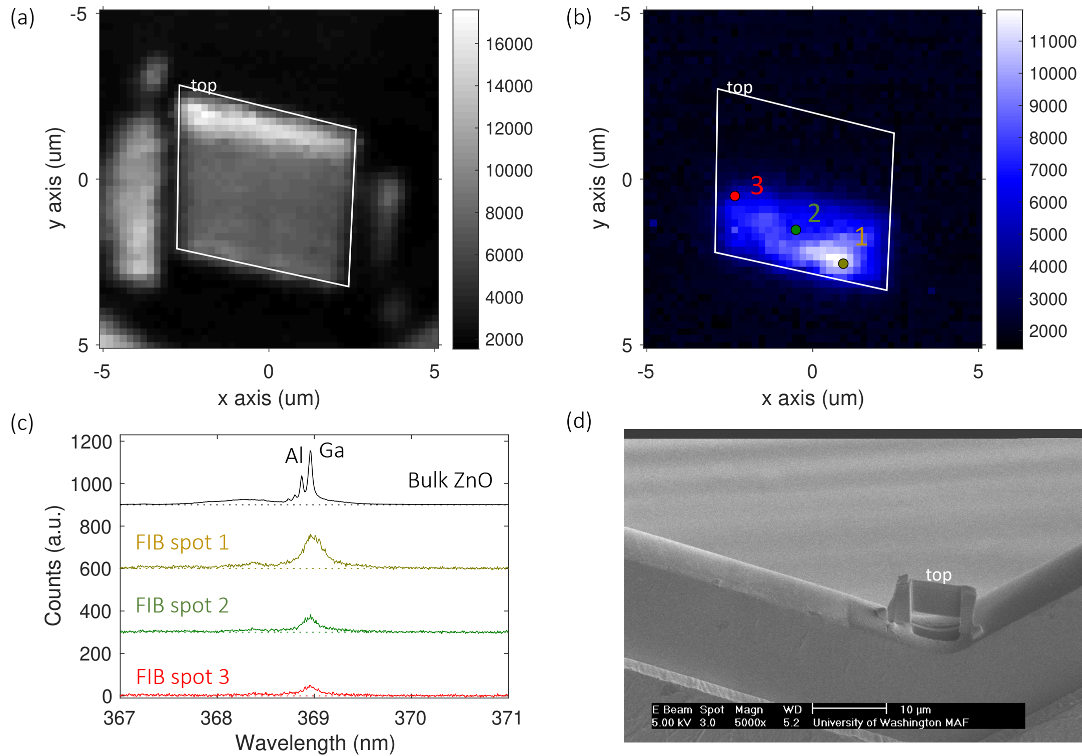

Figure 5.5: PL measurements on the 4th FIB thin film. (a) Confocal scan collecting the laser reflection. The white frame shows where the thin film is. (b) PL confocal scan at 10 K and 0 T. The white frame shows where the thin film is. (c) The spectra at the three spots marked in **b** with yellow, green, and red circles. A spectrum from the bulk sample (black curve) is plotted as a comparison. Excitation at ∼360 nm. The bulk sample is at ∼6 K with 90 nW excitation power. The FIB sample is at ∼10 K with 6 µW excitation power. The intensity of the bulk spectrum is scaled to match with the spectra from the FIB thin film. (d) The SEM image of the thin film. The top side of the ZnO thin film is marked as “top” in **a**, **b** and **d**.

5.4 PL quenching effect

From all four samples, there is a µm-scale region where the PL gets completely quenched due to the direct exposure to ion beams. For the 1st, 2nd and 4th samples, the direct exposure to ions is at the top part of the thin film. The penetration depth of 30 keV ions in ZnO is about ∼20 nm [155]. But the region with PL quenching has a depth of 1-2 µm. This indicates the ions can have a significant influence on the PL emission without actually reaching the effected region. This quenching effect has also been reported in experiments on ZnO nanorods and CdS nanobelts [156, 157]. The origin of the quenching is still unclear. Possible reasons can be ion induced crystal damage or Fermi level pinning at the surface. Further study on this quenching effect needs to be done in the future to better understand the mechanism and how to quantitatively control the quenching.

This PL quenching effect can potentially be utilized to isolate single donors, as shown in Fig. 5.6. The idea is to pattern circle-shaped e-beam resist on top of the surface, and then expose the sample to ion beams at different angles. Those regions that are directly exposed to ions would have the PL quenching effect while the small nanocone region protected by the e-beam resist can still emit PL. With a 100 nm diameter nanocone, the estimated donor number in the nanocone is about 1 (calculated using donor density of 10^{16} cm^{-3}). A more systematic study on the PL quenching effect is needed to further determine whether this idea would work or not.

5.5 Conclusion

In this chapter, we fabricate four ZnO thin films using FIB. We have developed two routines for the fabrication: one with top milling and one with side milling. PL properties of the fabricated thin films are investigated at low temperature. The PL has a large inhomogeneity across the thin films. Sharp donor lines can only be observed at certain spots in the 1st and 2nd thin films. Another important finding is the PL quenching effect due to direct ion exposure. This effect can potentially be used for single donor isolation but still needs to be investigated further to understand the quenching mechanism.

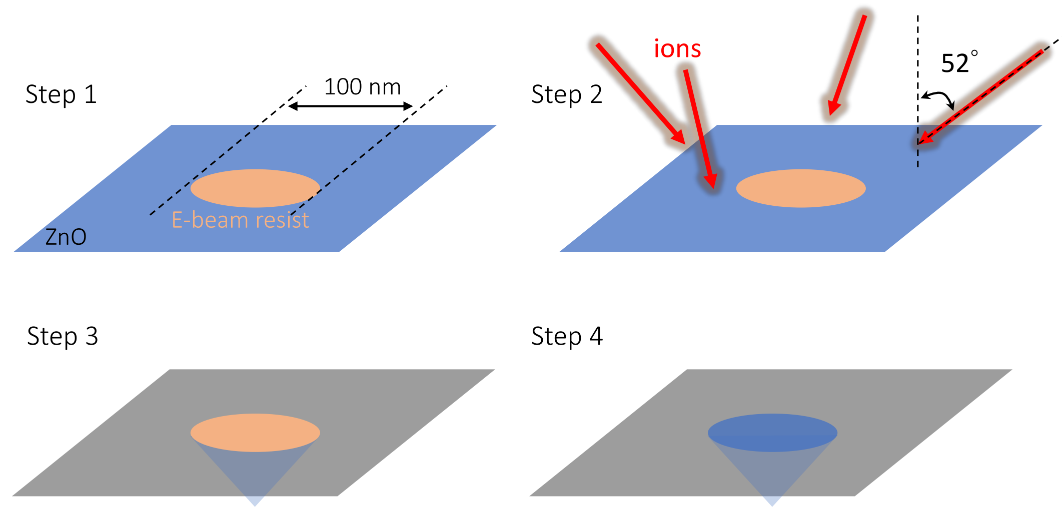

Figure 5.6: Proposed protocol for single donor isolation with FIB.

Chapter 6

PROGRESS TOWARDS HIGH-FIDELITY SPIN CONTROL WITH MICROWAVE PULSES IN ZNO

6.1 Introduction

High-fidelity control of qubit states is critical for most quantum applications. For the experiments in Chapter 4, the spin control is realized through stimulated Raman transitions using a detuned ultra-fast laser pulse. This method has been successfully used in trapped ions with high gate fidelity [158, 159]. However, for donors in ZnO, due to a laser induced dephasing effect, only small angle rotations can be achieved and the fidelity is low. An alternative control method is to use microwave pulses on resonance with the spin splitting.

There are two challenges associated with utilizing this technique for donors in ZnO. The first challenge is how to get efficient optical pumping at magnetic fields which are low enough to implement direct microwave spin control. The optical linewidth of the donor transitions is around 20 GHz. In order to achieve efficient optical pumping, the magnetic fields need to be large enough so that the spin splitting is several times the optical linewidth. In Voigt geometry ($B \perp \hat{c}$), we find that optical pumping is not observable below 2.25 T. This corresponds to an electron spin splitting of 62 GHz, which is high for microwave control. In this chapter, we first show this issue can be solved in Faraday geometry ($B \parallel \hat{c}$) by selectively exciting the spin transition with circular polarization. Optical pumping can be observed at fields down to 0.3 T, corresponding to a frequency of 8.3 GHz. This frequency is accessible with standard microwave generator.

The second challenge is attaining the needed microwave field amplitude. The inhomogeneous dephasing time T_2^* in our sample is ∼17 ns. The microwaves need to drive the spins at a GHz-scale Rabi frequency in order to have a π-rotation within the dephasing time. For donors in ZnO, the microwave pulses are coupled to the spin magnetically through electron spin resonance. With this weak magnetic coupling, the Rabi frequency is typically limited to

MHz-scale [160, 161]. In this chapter, we design and test a microwave resonator to enhance the microwave field amplitude. With this resonator, a 10 ns π-pulse should be achievable with $\sim$2 W microwave input power.

6.2 Selection rules in Voigt geometry and Faraday geometry

The top valence band of ZnO has a Γ_7 symmetry. The eigenstates of holes at zero magnetic field can be written as [162]:

$$\begin{cases} |\Downarrow\rangle_{B=0} & = ia\left|\frac{X+iY}{\sqrt{2}},\downarrow_z\right\rangle - ib\left|Z,\uparrow_z\right\rangle, \\ |\Uparrow\rangle_{B=0} & = a\left|\frac{X-iY}{\sqrt{2}},\uparrow_z\right\rangle + b\left|Z,\downarrow_z\right\rangle, \end{cases} \tag{6.1}$$

where the notation of the hole denotes the unoccupied electron with an opposite angular momentum in the valence band. $\left|\frac{X\pm iY}{\sqrt{2}}\right\rangle$ and $|Z\rangle$ are the orbital basis functions. From first-principles calculations, the parameters a and b are determined to be 0.9950 and -0.0999 [162]. The z direction is parallel to the c-axis of the crystal. As the conduction band has an s-orbital nature, the eigenstates of electrons at zero magnetic field are [163]

$$\begin{cases} |\uparrow\rangle_{B=0} & = \left|S,\uparrow_z\right\rangle, \\ |\downarrow\rangle_{B=0} & = i\left|S,\downarrow_z\right\rangle. \end{cases} \tag{6.2}$$

6.2.1 Selection rules in Voigt geometry

In the Voigt geometry shown in Fig. 6.1 (a), with a nonzero in-plane magnetic field ($B \parallel x$), the Zeeman Hamiltonian is $g^{\perp}_{e(h)}\mu_B B_x \sigma_x$ for electrons (holes). The eigenstates of electron and hole change to

$$\begin{cases} |\Downarrow\rangle_{B>0} & = \frac{1}{\sqrt{2}}\left(ia\left|\frac{X+iY}{\sqrt{2}},\downarrow_z\right\rangle - ib\left|Z,\uparrow_z\right\rangle\right) + \frac{1}{\sqrt{2}}\left(a\left|\frac{X-iY}{\sqrt{2}},\uparrow_z\right\rangle + b\left|Z,\downarrow_z\right\rangle\right), \\ |\Uparrow\rangle_{B>0} & = \frac{1}{\sqrt{2}}\left(ia\left|\frac{X+iY}{\sqrt{2}},\downarrow_z\right\rangle - ib\left|Z,\uparrow_z\right\rangle\right) - \frac{1}{\sqrt{2}}\left(a\left|\frac{X-iY}{\sqrt{2}},\uparrow_z\right\rangle + b\left|Z,\downarrow_z\right\rangle\right), \end{cases} \tag{6.3}$$

$$\begin{cases} |\uparrow\rangle_{B>0} &= \frac{1}{\sqrt{2}}\left|S,\uparrow_z\right\rangle + \frac{i}{\sqrt{2}}\left|S,\downarrow_z\right\rangle, \\ |\downarrow\rangle_{B<0} &= \frac{1}{\sqrt{2}}\left|S,\uparrow_z\right\rangle - \frac{i}{\sqrt{2}}\left|S,\downarrow_z\right\rangle. \end{cases} \tag{6.4}$$

The dipole matrix element for the recombination of electron state $|i\rangle$ and hole state $|j\rangle$ is $\boldsymbol{p}_{ij} = \langle j|\boldsymbol{\mu}|i\rangle$. The dipole operator is $\boldsymbol{\mu} = e\boldsymbol{r}$, where e is the electron charge and $\boldsymbol{r} = x\hat{\boldsymbol{x}} + y\hat{\boldsymbol{y}} + z\hat{\boldsymbol{z}}$ is the space vector. The calculated results of the four $\boldsymbol{p}_{ij}$ are shown below:

$$\begin{cases} \langle\Uparrow|\boldsymbol{\mu}|\uparrow\rangle = \mu_0 \cdot (i\frac{a}{\sqrt{2}}\hat{\boldsymbol{y}}), \\ \langle\Uparrow|\boldsymbol{\mu}|\downarrow\rangle = \mu_0 \cdot (-\frac{a}{\sqrt{2}}\hat{\boldsymbol{x}} + ib\hat{\boldsymbol{z}}), \\ \langle\Downarrow|\boldsymbol{\mu}|\uparrow\rangle = \mu_0 \cdot (\frac{a}{\sqrt{2}}\hat{\boldsymbol{x}} + ib\hat{\boldsymbol{z}}), \\ \langle\Downarrow|\boldsymbol{\mu}|\downarrow\rangle = \mu_0 \cdot (-i\frac{a}{\sqrt{2}}\hat{\boldsymbol{y}}), \end{cases} \tag{6.5}$$

where $\mu_0 = \langle S|e \cdot x|X\rangle = \langle S|e \cdot y|Y\rangle = \langle S|e \cdot z|Z\rangle$, and we use spin combination rules $\langle\uparrow|\downarrow\rangle = \langle\downarrow|\uparrow\rangle = 0$ and $\langle\uparrow|\uparrow\rangle = \langle\downarrow|\downarrow\rangle = 1$. The intensity of the optical transition between electron state $|i\rangle$ and hole state $|j\rangle$ is proportional to $|\boldsymbol{\varepsilon} \cdot \boldsymbol{p}_{ij}|^2$ [27], where $\boldsymbol{\varepsilon}$ is the electric field vector of the excitation laser. In the Voigt geometry, $\hat{\boldsymbol{x}}$ and $\hat{\boldsymbol{y}}$ correspond to horizontal (H) and vertical (V) polarizations. The light with polarization $\hat{\boldsymbol{z}}$ can't be detected in this geometry as light with $\hat{\boldsymbol{z}}$ polarization can only propagate in the x-y plane. Therefore, for the four transitions in this geometry, we expect the two transitions with highest and lowest energy to have V polarization, and the other two transitions to have H polarization. The collected PL intensity of the four transitions is the same. This is consistent with our experimental observation shown in Fig. 6.1(c) and also with the results in the literature [130].

We note that this theory uses single particle wave functions of electrons and holes and the exchange interaction between electrons and holes [164, 165] is not taken into consideration. In the donor system, due to the spin-singlet nature of the two electrons, the exchange interaction between the electron and hole is expected to be weak [164]. In the measured PL spectra, no exchange splitting is observed within the ~80 μeV spectrometer limited resolution. The exchange interaction is also not observed for donor systems in other

materials [166, 167].

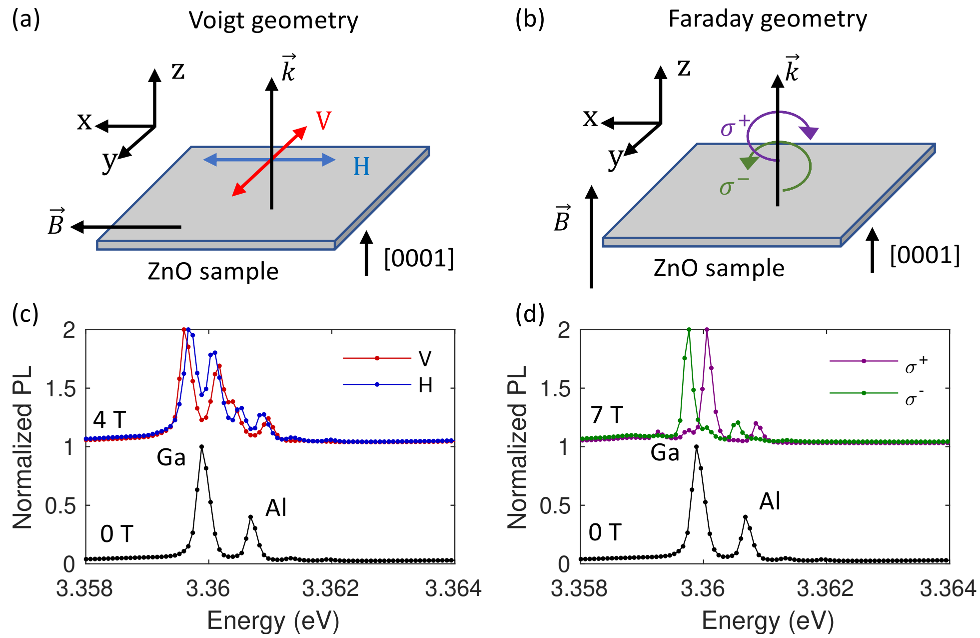

Figure 6.1: (a-b) The experimental geometry and PL spectra in the Voigt and Faraday geometry. $\vec{k}$ is the optical propagation axis. $\vec{B}$ shows the magnetic field direction. V and H represent vertical polarization ($\hat{\varepsilon} \perp \vec{B}$) and horizontal polarization ($\hat{\varepsilon} \parallel \vec{B}$), respectively. σ^+ and σ^- represent left-hand and right-hand circular polarization. (c-d) PL spectra at a magnetic field in the Voigt geometry and Faraday geometry. Spectrum at 0 T is plotted for comparison. The temperature is at 1.5 to 5 K. The excitation is at $\sim$360 nm with 20 to 100 nW. All spectra are normalized to have a maximum intensity of 1.

6.2.2 Selection rules in Faraday geometry

In the Faraday geometry shown in Fig. 6.1 (b), the Zeeman Hamiltonian is $g^{\parallel}_{e(h)}\mu_B B_z \sigma_z$ for electrons (holes). As the magnetic field is parallel to $\hat{\boldsymbol{z}}$, the eigenstates are the same as the states at zero fields:

$$\begin{cases} |\Downarrow\rangle_{B_z>0} &= ia\left|\frac{X+iY}{\sqrt{2}}, \downarrow_z\right\rangle - ib\left|Z, \uparrow_z\right\rangle, \\ |\Uparrow\rangle_{B_z>0} &= a\left|\frac{X-iY}{\sqrt{2}}, \uparrow_z\right\rangle + b\left|Z, \downarrow_z\right\rangle, \end{cases} \tag{6.6}$$

$$\begin{cases} |\uparrow\rangle_{B_z>0} &= \left|S, \uparrow_z\right\rangle, \\ |\downarrow\rangle_{B_z>0} &= i\left|S, \downarrow_z\right\rangle. \end{cases} \tag{6.7}$$

Similar as the calculation done in the Voigt geometry, we calculate the dipole matrix element $\boldsymbol{p}_{ij} = \langle j|\boldsymbol{\mu}|i\rangle$. The calculated results of the four $\boldsymbol{p}_{ij}$ are:

$$\begin{cases} \langle\Uparrow|\boldsymbol{\mu}|\uparrow\rangle = \mu_0 \cdot a\frac{\hat{\boldsymbol{x}}+i\hat{\boldsymbol{y}}}{\sqrt{2}}, \\ \langle\Uparrow|\boldsymbol{\mu}|\downarrow\rangle = \mu_0 \cdot ib\hat{\boldsymbol{z}}, \\ \langle\Downarrow|\boldsymbol{\mu}|\uparrow\rangle = \mu_0 \cdot ib\hat{\boldsymbol{z}}, \\ \langle\Downarrow|\boldsymbol{\mu}|\downarrow\rangle = \mu_0 \cdot a\frac{\hat{\boldsymbol{x}}-i\hat{\boldsymbol{y}}}{\sqrt{2}}, \end{cases} \tag{6.8}$$

where $\mu_0 = \langle S|e \cdot x|X\rangle = \langle S|e \cdot y|Y\rangle = \langle S|e \cdot z|Z\rangle$. In the Faraday geometry, $\hat{\boldsymbol{x}} + i\hat{\boldsymbol{y}}$ and $\hat{\boldsymbol{x}} - i\hat{\boldsymbol{y}}$ correspond to σ^+ and σ^- polarization. The light with polarization $\hat{\boldsymbol{z}}$ can not be detected in this geometry as light with $\hat{\boldsymbol{z}}$ polarization can only propagate in the x-y plane. Also, as $b \ll a$, the intensity of the two $\hat{\boldsymbol{z}}$ polarized transitions are much weaker than the two circularly polarized transitions. Due to this selection rule, we can only see two equal-intensity transitions in the PL spectrum, one with σ^+ polarization and one with σ^- polarization. This is consistent with the observed PL spectra, as shown in Fig. 6.1(d). It is also consistent with the results in the literature [130].

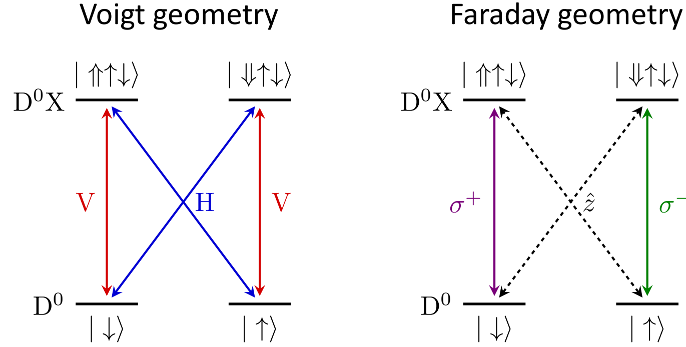

Figure 6.2: Energy diagram of the donor system at small magnetic fields in the Voigt geometry and Faraday geometry. Note that we use the convention that the transition $|\Uparrow\uparrow\downarrow\rangle \leftrightarrow |\downarrow\rangle$ corresponds to recombination of $|\Uparrow\rangle$ hole and $|\uparrow\rangle$ electron.

6.2.3 Energy diagram at low fields

Figure 6.2 shows the energy diagram of the donor system at small magnetic fields in Voigt and Faraday geometries. The diagrams are plotted based on the derived selection rules. The magnetic field is in the scale that the Zeeman energy is smaller than the optical linewidth. In the Voigt geometry, no matter what polarization is chosen for the excitation, both $|\downarrow\rangle$ and $|\uparrow\rangle$ states would be optically pumped, so the electron cannot be initialized to a certain spin state. However, in Faraday geometry, the spin can be selectively pumped with σ^+ or σ^- polarized light. For example, if excited by a σ^+ polarized laser, the spin can be pumped to spin $|\uparrow\rangle$.

6.3 Optical pumping in the Faraday geometry

For the optical pumping measurements done in the Voigt geometry, the excitation is resonant with the transition $|\Downarrow\uparrow\downarrow\rangle \Leftrightarrow |\uparrow\rangle$ using vertical polarization and the signal is collected from transition $|\Downarrow\uparrow\downarrow\rangle \Leftrightarrow |\downarrow\rangle$ with horizontal polarization. Because of the orthogonal polarization between excitation and collection, the laser reflection from the sample surface can be eliminated through cross polarization. However, this does not work for Faraday geometry as there is only one transition accessible for each spin state, e.g. only the σ^+ transition is accessible for the spin $|\downarrow\rangle$ state. In the Faraday geometry, it is necessary to both excite and

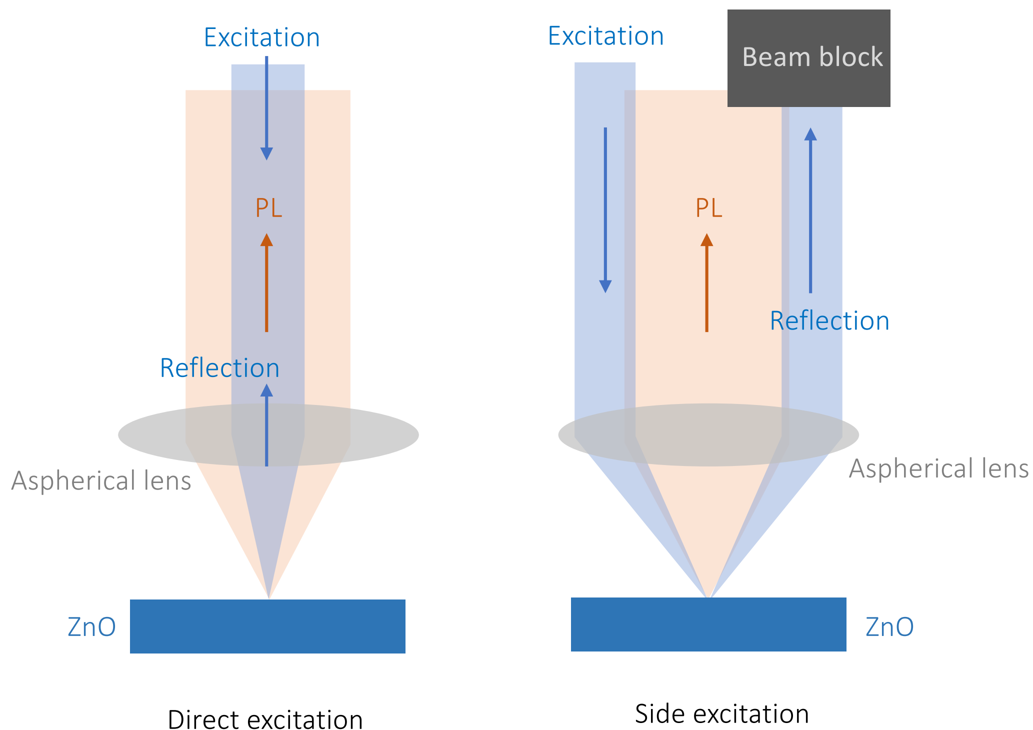

Figure 6.3: Illustration of the direct-excitation setup and side-excitation setup. The blue beams are the excitation laser or laser reflection from the sample surface. The orange beams are the PL from the ZnO donors. The beam block in the side excitation setup can block the reflected laser beam.

collect the same transition in order to monitor the optical pumping process. Therefore, the cross polarization technique can not be used to eliminate the laser reflection.

An alternative method is to use the side excitation technique, as shown in Fig. 6.3. For a direct-excitation setup, the laser is incident on the the center of the aspheric lens (or objective lens). The reflected laser from the sample surface and the PL emitted by the sample are in the same path. For the side-excitation setup, the excitation laser is incident on the edge of the aspheric lens while the direction is still parallel to the optical axis of the lens. With this alignment, the laser reflection and the PL are separated. A small beam block can selectively block the laser reflection but still let the PL pass through. Using this

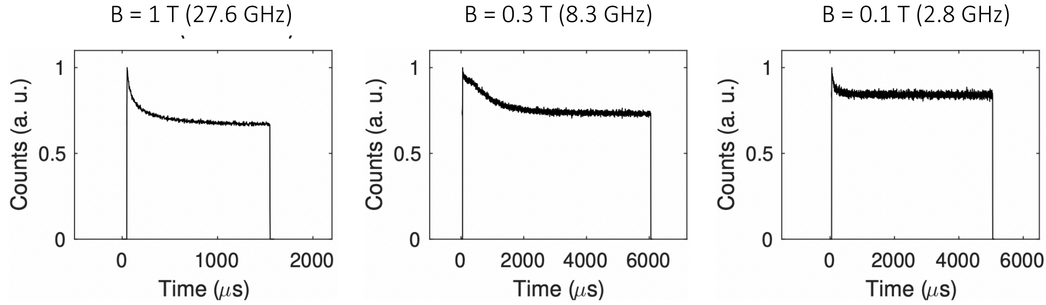

Figure 6.4: Optical pumping curves at 3 different fields in Faraday geometry. The magnetic field and the corresponding electron Zeeman splitting in units of GHz are labeled on top of each figure. The temperature is at 1.5 K. At the beginning of the optical pumping pulse, the spin population is initialized to 50% $|\uparrow\rangle$ and 50% $|\downarrow\rangle$ by using laser pulses at energy much higher than the donor transition ($\sim$ 360 nm). The cw laser used for optical pumping has a power of 5 to 13 nW.

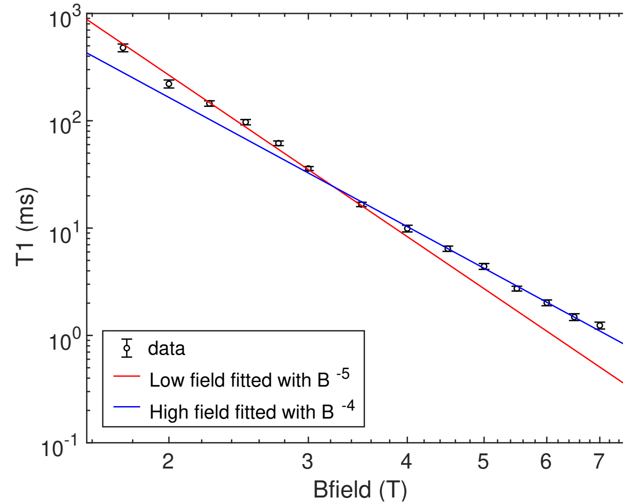

Figure 6.5: T_1 measurements in the Faraday geometry. Temperature is at 1.5 K.

side-excitation setup, the PL signal can be collected without the strong background from laser scattering.

Figure 6.4 shows the optical pumping curve at 1 T, 0.3 T and 0.1 T. Optical pumping signal is clearly observed for the 1 T and 0.3 T data. There is also a small signal for the 0.1 T data. The pump-down time is hundreds of µs, much longer than the several µs pump-

down time in the Voigt geometry. This is due to the weak dipole moments of the two $\hat{\boldsymbol{z}}$ transitions. Reasonably good optical pumping can be obtained at 0.3 T which corresponds to an electron Zeeman splitting of 8.3 GHz. The fidelity of the optical pumping is about 60%. The measured low fidelity is possibly due to imperfect circular polarization and diffuse laser reflection that cannot be blocked by the side-excitation setup. Even though the fidelity is not really high, the signal should be strong enough to test the microwave spin control. A T_1 study is performed in this geometry [168], as shown in Fig. 6.5. In this measurement, we show a maximum of $\sim$0.5 s T_1 at 1.75 T.

6.4 *Microwave strength needed for GHz-scale Rabi frequency*

The Hamiltonian of the electron spin is

$$H_0 = \begin{pmatrix} 0 & 0 \\ 0 & \hbar\omega_e \end{pmatrix} \begin{matrix} |\downarrow\rangle \\ |\uparrow\rangle \end{matrix}, \tag{6.9}$$

where $\hbar\omega_e = g_e\mu_B B$ is the electron spin splitting and B is the external magnetic field. The spin is coupled to the microwave magnetically. The magnetic field in the microwave can be written as $B_0\cos(\omega t + \phi)$, where B_0 is the amplitude of the magnetic field, ω is the microwave frequency, and ϕ is the phase of the microwave. By setting the microwave field perpendicular to the spin orientation, the interaction between the spin and the microwave is

$$U = \begin{pmatrix} 0 & \frac{1}{2}g_e\mu_B B_0\cos(\omega t + \phi) \\ \frac{1}{2}g_e\mu_B B_0\cos(\omega t + \phi) & 0 \end{pmatrix} \tag{6.10}$$

In the interaction picture, this Hamiltonian changes to

$$\begin{aligned} H' &= e^{iH_0 t/\hbar} \cdot U \cdot e^{-iH_0 t/\hbar} \\ &= \begin{pmatrix} 0 & \frac{1}{2}g_e\mu_B B_0 e^{-i\omega_e t}\cos(\omega t + \phi) \\ \frac{1}{2}g_e\mu_B B_0 e^{i\omega_e t}\cos(\omega t + \phi) & 0 \end{pmatrix}. \end{aligned} \tag{6.11}$$

As $\cos(x) = (e^{ix} + e^{-ix})/2$, we obtain

$$e^{-i\omega_e t}\cos(\omega t + \phi) = \frac{1}{2}e^{-i(\omega_e-\omega)t}e^{i\phi} + \frac{1}{2}e^{-i(\omega_e+\omega)t}e^{-i\phi}. \tag{6.12}$$

In the experiment, ω is set on resonance with the spin splitting, i.e. $\omega = \omega_e$. In the rotating wave approximation, we can drop the second term as this fast oscillation time averages to zero. Under this approximation, the Hamiltonian changes to

$$H' = \begin{pmatrix} 0 & \frac{1}{4}g_e\mu_B B_0 e^{i\phi} \\ \frac{1}{4}g_e\mu_B B_0 e^{-i\phi} & 0 \end{pmatrix}. \tag{6.13}$$

With the microwave on, the spin state has a Rabi oscillation between $|\uparrow\rangle$ and $|\downarrow\rangle$ with a Rabi frequency

$$\Omega = \frac{g_e\mu_B B_0}{4\pi\hbar}. \tag{6.14}$$

The phase ϕ controls the rotation axis in the Bloch sphere. To achieve a 10 ns π-pulse (0.1 GHz Rabi frequency), the required field strength in the microwave needs to be $B_0 =$ 7.25 mT. This is a pretty strong field. To demonstrate how strong this is, we use the field generated by a simple circular coil as an example. We assume the coil has a 1 cm radius and its impedance is matched with 50 Ω coaxial cables so that microwave signals do not reflect back. To create the required field strength in the middle of the coil, the microwave power needs to be $\sim$300 kW, which is too high for a reasonable experiment. Therefore, a microwave resonator is necessary to get the mT-scale field strength with a reasonable microwave power.

6.5 Design of the microstrip resonator

A microstrip line consists of a metal strip and a ground metal plane on the two sides of the dielectric substrate, as shown in Fig. 6.6. It is used for transmitting microwave-frequency signal and can be easily fabricated with printed circuit board (PCB) techniques. The magnetic field above the strip line has an in-plane direction which is the direction needed for the spin rotation.

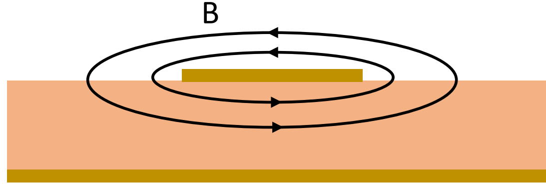

Figure 6.6: Schematic of a microstrip line.

The designed microstrip resonator consists of a short feed line with 50 Ohm characteristic impedance, a 140 µm gap for capacitive coupling and an Ω-shape resonator, as shown in Fig. 6.7(a). The dielectric substrate we use is the Rogers TMM4 laminate. The resonator structure is simulated with Ansys HFSS (high frequency structure simulator) software. Figure 6.8 shows the simulated reflection spectrum of the system, i.e. the scattering parameter S11 as function of the microwave frequency. The resonance frequency is at 8.48 Ghz and the Q-factor of structure is 46. As we want to use a ∼10 ns π-pulse, the bandwidth of the resonance needs to be large enough to cover frequency broadening of the pulse. With resonance frequency at 8.48 GHz and a 10 ns pulse, the Q-factor should be limited below 500. The designed structure meets this requirement.

The ZnO sample used for this experiment has a 50 µm thickness. The distribution of the in-plane magnetic field at 50 µm above the resonator surface is shown in Fig. 6.7(b-c). With 1 W microwave power, the maximum magnetic field strength is about 5 mT. To reach the required 7.25 mT, the input power is ∼2.1 W, which can be achieved with a relatively inexpensive microwave amplifier. This power can possibly be reduced by further optimization of the structure such as using different resonator shapes [169, 170, 171, 172] or changing the dielectric substrate, e.g. using Sapphire which has a large dielectric constant (∼10).

To verify the advantage of the resonator structure, a simple 50 Ω microstrip transmission line is simulated for comparison, as shown in Fig. 6.9. The field strength in this structure is about two orders of magnitude smaller than the resonator structure. To achieve the required 7.25 mT strength in this structure, the microwave power needs to be ∼8 kW.

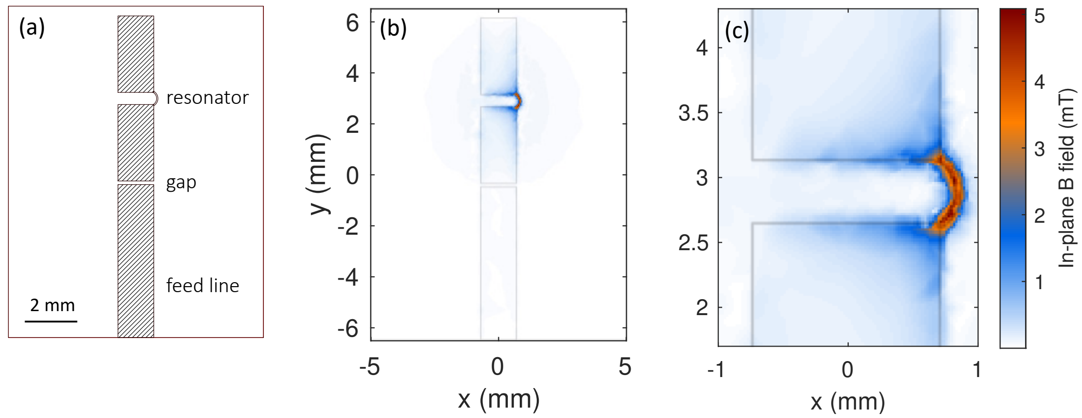

Figure 6.7: (a) The design of the resonator geometry. (b) Distribution of the in-plane magnetic field strength at 50 µm above the surface. The microwave frequency is set at the resonance of the resonator (8.48 GHz). The input power is 1 W. The grey lines show the outline of the resonator structure. (c) The distribution of the field strength near the small arc in the resonator. The grey lines show the outline of the resonator structure.

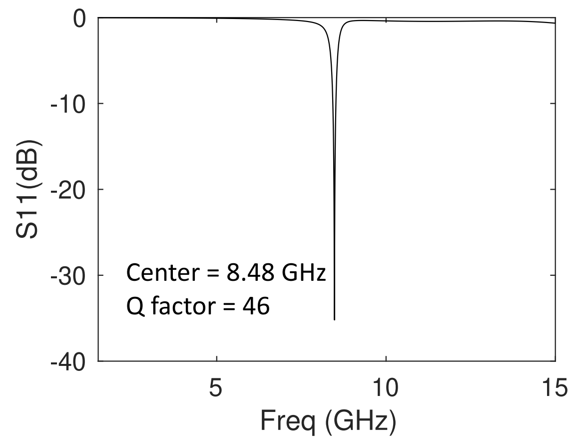

Figure 6.8: Simulated reflection spectrum of the resonator structure (S11 as function of frequency).

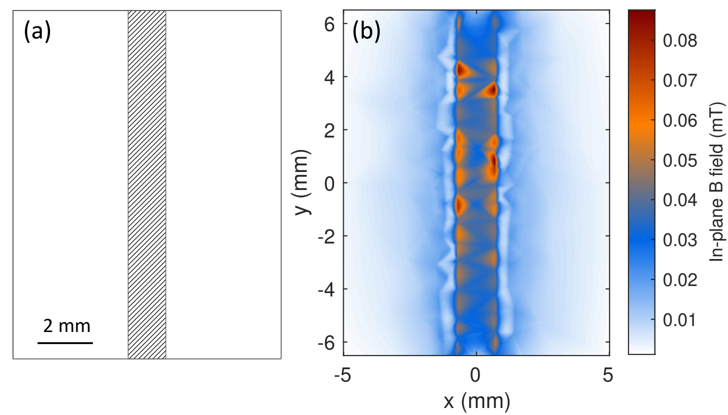

Figure 6.9: (a) The geometry of the transmission line. (b) Distribution of the in-plane magnetic field strength at 50 µm above the surface. The microwave frequency is set at 8.48 GHz. The input power is 1 W. The output of the transmission line is terminated with 50 Ω. The triangular features in the plot are because of the relatively large triangle-shaped mesh in the simulation.

6.6 Fabrication and characterization of the microstrip resonator

The resonator structure is fabricated on a Rogers TMM4 laminate using a LPKF Laser-based PCB-prototyping system. An image of the fabricated resonator is shown in Fig. 6.10(a). The resonator is soldered to an SMA connector for further experiments. The fabricated resonator is characterized by measuring the reflection spectrum. The measurements are carried with a home-built setup shown in Fig. 6.10(c). The red curve in Fig. 6.10(d) shows the reflection spectrum of the structure. A resonance is observed at 8.98 GHz which is 0.5 GHz different from the designed 8.48 GHz. The small oscillation at those off-resonance frequencies is due to reflection loss at different microwave electronics. The S11 at the resonance is only about -8.5 dB, much larger than the simulated -35 dB, which means the coupling strength between the feed line and the resonator is not as strong as the design. We attribute both the shift of the resonance frequency and the smaller resonance dip to the imperfection in the fabrication process. The resolution of the laser cutter is only about 15 μm while

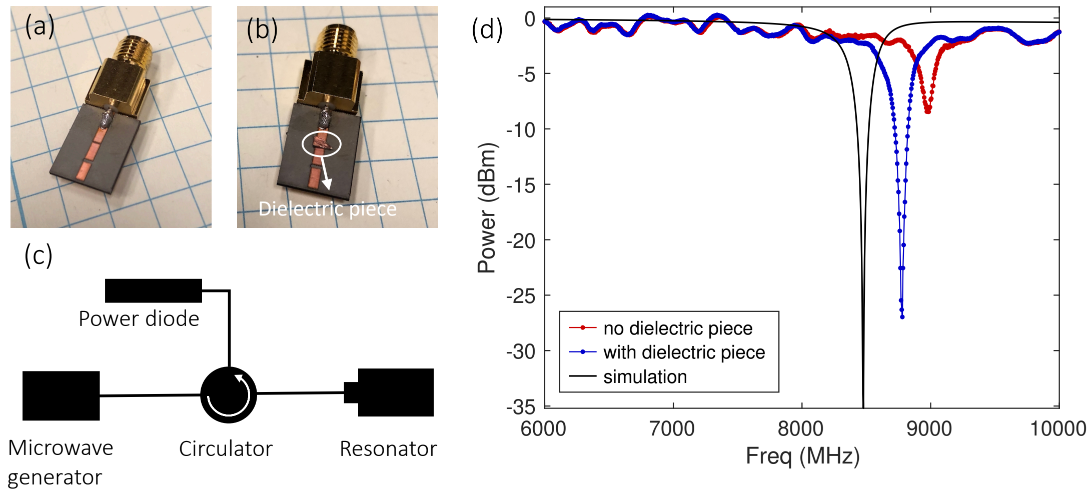

Figure 6.10: (a) Optical image of the resonator chip. (b) Optical image of the resonator chip with a small dielectric piece on top of the coupling gap. (c) Experimental setup for the reflection spectrum. (d) Reflection spectra of the resonator chips without and with the dielectric piece at room temperature. The simulated curve is plotted for comparison. The input power of the microwave generator is 0 dBm. S11 is the measured reflected power divided by the input microwave power.

the smallest feature on the resonator is about 50 µm. One trick to increase the coupling strength is to put a small dielectric piece on top of the coupling gap. Due to the larger dielectric constant than the air, the coupling can be enhanced. Figure 6.10(b) shows an image of the resonator with a small dielectric piece on top of the gap. The blue curve in Fig. 6.10(d) is the corresponding reflection spectrum. The depth of the resonance dip is $\sim$25 dB, which is greatly enhanced compared to the structure without a dielectric piece. The required microwave power to get 0.1 GHz Rabi frequency in this structure should be close to the simulated structure, i.e. 2 W.

6.7 Conclusion

In this chapter, we have shown our progress on the microwave spin control for donors in ZnO. The two main challenges of the experiments are how to get optical pumping at low field and how to get enough microwave strength. For the first challenge, we solve it by working in the Faraday geometry. Optical pumping down to 0.3 T (8.3 GHz) is observed with relatively good fidelity. For the second challenge, we have designed a microstrip resonator to enhance the magnetic field strength. From the simulation, to have a 10 ns π-pulse, $\sim$2 W input power is needed on the resonator. The resonator structure is fabricated with a laser-based PCB-prototyping system. Reflection spectrum at room temperature is measured and the result reasonably agrees with the simulation.

Chapter 7

SUMMARY AND OUTLOOK

This thesis focuses on the study of different dopant qubits in direct band gap materials. In this chapter, we summarize the work we have done and provide an outlook on using the dopant qubits for quantum networks.

We first study the acceptor system in strained GaAs. The strain lifts the HH-LH degeneracy, which prevents the fast spin relaxation between HH and LH. The coherence properties are measured through optical pumping and coherent population trapping. In the strained sample, µs-scale spin relaxation time T_1 and a $\sim$7 ns inhomogeneous dephasing time T_2^* are observed, which are not long enough for qubit applications. The magnitudes of both T_1 and T_2^* are limited by the HH-LH mixing due to the small shear strain in the sample. Improvement on the coherence times should be possible with other strain engineering techniques such as piezoelectric actuator.

Due to the poor coherence properties of the acceptors in our strained sample, we revisit donor systems and have done a systematic T_1 study on three different materials: GaAs, InP, and CdTe. The donor T_1 in all three materials is on the ms-scale, limited by phonon interaction mediated by spin-orbit coupling. We have built a theoretical model to quantitatively calculate the spin relaxation time and have found reasonable agreements with the experimental results in GaAs and CdTe. While 1 ms is long, these results suggest that an even longer T1 could be attained in materials with lower spin-orbit coupling. We note that for GaAs and InP, T_2^* will still be limited by hyperfine coupling due to nuclear spins however CdTe could be isotopically purified to serve as a nuclear spin-free host.

This T_1 work motivates our study of donors in ZnO, which has an electron g-factor close to the value of a free electron and a long-term potential for isotope purification. The electron g-factor for donors in ZnO indicates a small spin-orbit coupling thus long T_1. A complete study of optical and spin properties of ZnO donors is performed. The study shows

a T_1 up to 100 ms at 2.25 T and can possibly be longer at smaller magnetic fields. This is about two orders of magnitude higher than the other three materials we have studied. We have also demonstrated optical coherent control with a detuned ultra-fast laser pulse. With this technique, a 17 ns T_2^* and a 50 µs spin-echo T_2 are measured. This T_2^* is already much better than the values measured in GaAs. Furthermore, because only 4.1% of Zn and 0.038% of O have nuclear spins, it is to possible obtain nuclear-spin-free isotopically purified ZnO, which would greatly enhance the dephasing time.

The donor system in ZnO is the most promising system we have studied as a dopant qubit candidate so we decide to keep studying this system. Two important requirements for the remote entanglement protocol are single qubit isolation and high-fidelity coherent control. We show our current progress to reach these two requirements for donors in ZnO. For the single donor isolation, we use focused ion beam to fabricate submicrometer thin films and we perform a PL study on the fabricated thin films. Though single donor isolation is not achieved, the PL measurements could give a guide on future research that utilizes FIB to isolate single donors. For coherent spin control, we have demonstrated it with ultra-fast optical pulses but only small-angle and low-fidelity rotation can be achieved due to the effect of laser induced dephasing. Microwave is an alternative for spin control, and it could have much better fidelity and larger rotation angle. The two issues with microwave control for donors in ZnO are how to achieve optical pumping at low fields which are suitable for microwave experiments and how to obtain microwave magnetic field amplitudes which correspond to GHz-scale Rabi frequencies. We have demonstrated optical pumping in the Faraday geometry at 0.3 T, corresponding to an electron Zeeman splitting of 8.3 GHz, which is small enough for microwave control. A microstrip resonator is designed to provide GHz-scale Rabi frequency with reasonable microwave power. With the current design, a 10 ns π-pulse should be achievable with $\sim$2 W input power.

Potentially, donors in ZnO can satisfy all the qubit requirements listed in Chapter 1, i.e. single qubit isolation, identical qubits, high radiative efficiency in ZPL, high-fidelity spin control, and long coherence. ZnO has pretty high radiative efficiency and more than 90% of the photons are in the ZPL. We are still working on the single donor isolation and high-fidelity spin control, and it is promising to achieve these two goals in the next few years.

Identical qubits and long coherence times require high-quality sample growth with both chemical and isotope purification. With the help of nanofabrication techniques, structures such as on-chip waveguide, optical cavities, Stark or strain tuning can be integrated to the donor systems to enable better qubit controls.

Appendix A

SUPPLEMENTARY INFORMATION FOR LONGITUDINAL SPIN RELAXATION IN GAAS, INP AND CDTE

A.1 Surface depletion effects

In the GaAs and InP samples, a μs-scale time-dependent increase in luminescence was observed in all band edge PL after the start of an optical excitation pulse. The magnitude of this effect varied significantly between samples and depended on both the wavelength and intensity of the optical excitation. The effect was greater in InP than in GaAs and was greater in lower doped samples. It did not significantly depend on emission wavelength. Free exciton, D^+X, D^0X, and A^0X transitions all behaved similarly.

Figure A.1a depicts a representative example of this effect in sample InP-2. In two experiments at 0 T and 1.6 K, the D^0X emission is detected during an excitation pulse. In the first experiment, the sample is excited with a 5 μW excitation pulse resonant with the D^0X transition. During the application of this pulse a small increase in optical emission at the beginning of the pulse can be observed on the microsecond time-scale (blue trace). This effect decreases with increasing field and increases with excitation power intensity. In the second experiment, we use a 5 μW excitation pulse with energy greater than the bandgap. A significant emission increase is observed. Using a pulse sequence similar to the T_1 sequence [Fig. 3.1(e)], we find the sample relaxes to its initial state on the timescale of 50 microseconds. For all T_1 measurements reported in the main manuscript, the resonant excitation power is always kept low enough so that this emission enhancement effect is negligible.

Due to this effect, we are unable to obtain a T_1 measurement for donors in InP-1, the InP sample with the lowest donor concentration. Example optical pumping curves for this sample are shown in Fig. A.1(b) at 4 T and 1.6 K. The blue trace shows data corresponding to the standard optical pumping pulse sequence depicted in Fig. 3.1(c). The visibility is

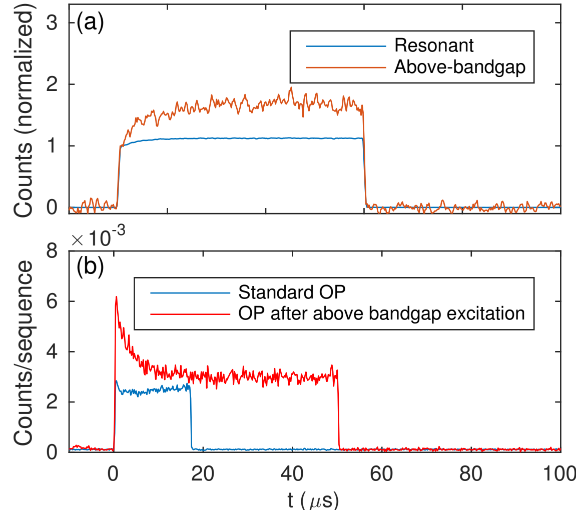

Figure A.1: Time-resolved photoluminescence during optical pulse. (a) Collection of D^0X emission during resonant D^0X excitation (blue curve) and above-bandgap excitation (red curve). A significant increase in emission intensity is observed for above-bandgap excitation. (b) Optical pumping traces for InP-1 at 4 T. Blue curve: Standard optical pumping experiment. Red curve: Prior to the optical pumping pulse, a 50 μs long above-bandgap pre-pulse is applied. The end of the pre-pulse is 5 μs before the start of the optical pumping pulse.

poor and in addition to the small optical pumping feature, we see an increase in the PL intensity after the initial optical pumping phase. For InP-1, this "brightening" effect is observed at all reasonable powers (i.e. powers for which we can obtain enough signal to reliably obtain a T_1 measurement) and the decay of this signal is the dominant contribution in T_1 pulse sequence measurements.

Additionally, we performed a two-pulse experiment where a 50 μs pulse with energy above the bandgap is applied to the sample until 5 μs before the the optical pumping pulse begins. The effect of the pre-pulse is dramatic (Fig. A.1): the larger visibility can be attributed to the pre-pulse depolarizing bound electron spins. However we also note that the intensity in the optically pumped steady-state, near the end of the pulse, is flat and significantly larger in the pre-pulse case. This indicates that in terms of emission intensity, the sample has reached steady-state during the application of the pre-pulse. We attribute the brightening effect to the elimination of near-surface fields in the GaAs and InP samples

under optical illumination [173]. The photogenerated carriers neutralize the surface states, resulting in an effective increase in the neutral region thickness and therefore the increase of photoluminescence intensity. There is evidence that very small fields, on the order of V/cm, can substantially quench fluorescence [174]. We do not observe this effect in CdTe, which is a true bulk sample rather than a few-micron-thick film, thus the surface field has a negligible effect.

A.2 Numerical solution of donor-bound electron in magnetic field

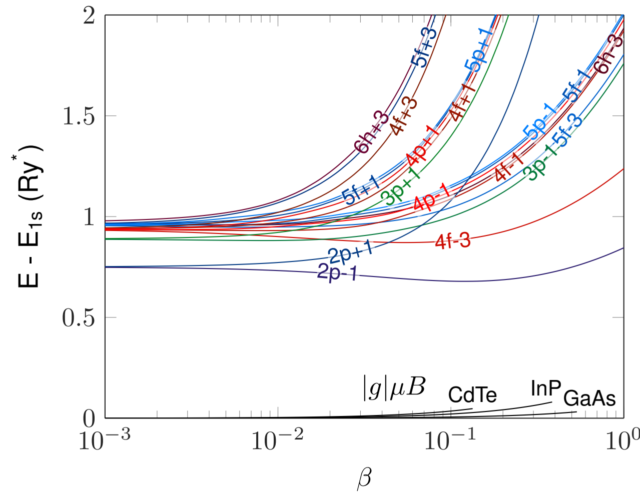

Figure A.2: Energies of excited state orbitals vs. dimensionless magnetic field β from numerical simulation of hydrogen atom in magnetic field. The plot shows the energy difference of 18 excited states from the ground state with the same spin projection. States are labeled by their zero-field quantum numbers. Also plotted is the Zeeman splitting energy $|g|\mu B$ in units of effective Rydberg, the maximum β of the plot being the maximum experimental β obtained for each material. The Zeeman energy can be ignored compared to the orbital energy.

The numerical solution of the hydrogen atom in a magnetic field is a nontrivial problem [175]. Of particular difficulty is the transition from the low-field to high-field regime, where the solutions cannot be conveniently expanded in hydrogen or Landau orbitals [176]. We have used a readily available finite element solver to find the energies and wave functions of hydrogen in a magnetic field of arbitrary strength [97]. These solutions can be mapped

onto the donor-bound electron problem by replacing the electron mass, Bohr radius, g-factor and other parameters by their effective values for the donor-bound electron. The magnetic field is measured by a dimensionless quantity $\beta = B/B_0$, where the reference magnetic field $B_0 = 2\hbar/[|e|(a_B^*)^2]$ is found by considering when the Larmor radius $\sqrt{2\hbar/|eB|}$ is equal to the donor Bohr radius. For GaAs, InP, and CdTe, B_0 is, 13.4 T, 19.3 T and 49.8 T respectively. In our experiment, the maximum applied field is 7 T, implying that the 1s wave function is a good approximation for the ground state. However, we note that for higher energy orbitals n, the magnetic field at which magnetic effects begin to dominate Coulomb ones occurs at B_0/n^3 [97]. Thus, higher energy orbitals are significantly perturbed even at small β. The energy difference between the excited states and the ground state are shown in Fig. A.2. The energy is scaled by the effective binding energy $\mathcal{E}_{Ry}^*$, which is 5.8, 7.0 and 13.6 meV for GaAs, InP and CdTe respectively.

A.3 Theory of spin-relaxation via the admixture mechanism

In this appendix, we calculate the spin-relaxation rate due to the admixture mechanism in several different ways. First we provide general simplifications that are common to all calculations. We then evaluate the expression for T_1 numerically at all fields and analytically at low and moderate fields.

A.3.1 General expression for the admixture spin-relaxation rate

It is convenient to represent the spin-relaxation rate, Eq. (3.7), in a simplified form. First, we investigate which excited states may contribute to spin relaxation by symmetry.

The Dresselhaus spin-orbit interaction Hamiltonian (3.12) is cubic in the electron wavevector. It can be conveniently decomposed in the spherical angular harmonics, $Y_l^m(\theta_k, \phi_k)$, where the subscripts $l = 0, 1, 2, \ldots$, $m = -l, -l+1, \ldots, l-1, l$, and θ_k, ϕ_k are the polar and azimuthal angles of the wavevector $\mathbf{k}$ in the spherical coordinate system

with z being the polar axis. Corresponding summands in Eq. (3.12) take the form:

$$\frac{k_x(k_y^2-k_z^2)}{k^3} = \sqrt{\pi}\left(\frac{Y_3^3-Y_3^{-3}}{\sqrt{35}}+\frac{Y_3^1-Y_3^{-1}}{\sqrt{21}}\right), \tag{A.1a}$$

$$\frac{k_y(k_z^2-k_x^2)}{k^3} = \sqrt{\pi}\left(\frac{Y_3^3+Y_3^{-3}}{i\sqrt{35}}-\frac{Y_3^1+Y_3^{-1}}{i\sqrt{21}}\right), \tag{A.1b}$$

$$\frac{k_z(k_x^2-k_y^2)}{k^3} = 2\sqrt{\frac{2\pi}{105}}\left(Y_3^2+Y_3^{-2}\right). \tag{A.1c}$$

Here the arguments of the spherical harmonics are omitted for brevity. In our frame of axes where $\mathbf{B} \parallel z$, the eigenstates of the donor-bound electron in the magnetic field are characterized by the angular momentum component m onto the z axis. Note that the term $\sigma_z k_z(k_x^2-k_y^2)$ in Eq. (3.12) does not play a role in the spin flip process. Hence, the intermediate states for the admixture mechanism, in agreement with the first two lines of Eq. (A.1), are those with $m=\pm 1$, $m=\pm 3$. In relatively weak fields where the magnetic field does not perturb the ground and excited stated wave functions, the donor-bound electron has spherical symmetry and Eq. (A.1) imposes a strict selection rule for the excited states: only $l=3$ (and $m=\pm 1$, $m=\pm 3$) can cause spin-relaxation.

As such, in the sum over excited states in Eq. (3.8), we only need to include $m=\pm 1$ and $m=\pm 3$ states. We also note that due to the azimuthal symmetry,

$$\langle \nu,\pi_z,m|k_x(k_y^2-k_z^2)|1\mathrm{s}\rangle = e^{-im\frac{\pi}{2}}\langle \nu,\pi_z,m|k_y(k_x^2-k_z^2)|1\mathrm{s}\rangle,$$

it is sufficient to calculate the contribution due to the $\sigma_x k_x(k_y^2-k_z^2)$ term in the Dresselhaus Hamiltonian. By combining positive and negative m terms and simplifying, we find

$$|M_{\uparrow\downarrow}|^2 = \frac{2\gamma^2\hbar}{\rho\omega_{\mathbf{q},\alpha}}|eA_{\mathbf{q},\alpha}|^2\left|\sum_{\substack{m=1,-3\\ \nu=1,2,\ldots\\ \pi_z=1}}\langle 1\mathrm{s}|e^{i\mathbf{qr}}|\nu,\pi_z,m\rangle\langle \nu,\pi_z,m|k_x(k_y^2-k_z^2)|1\mathrm{s}\rangle G_{\nu;m}\right|^2 \tag{A.2}$$

where $G_{\nu;m} = (\Delta E_{\nu,\pi_z,m} - g\mu B)^{-1} - (\Delta E_{\nu,\pi_z,-m} + g\mu B)^{-1}$ and $\pi_z = 1$ by symmetry. By

integrating over phonon modes, we find the general expression

$$\frac{1}{T_1} = F_{ph}\frac{\gamma^2}{2\pi^2\hbar^2\rho}\sum_{\alpha}\sum_{m=1,-3}\frac{|g\mu B|}{s_\alpha^3}\int d\Omega_q|eA_{\mathbf{q},\alpha}|^2 \cdot \\ \left|\sum_{\nu}\left[\langle 1\mathrm{s}|e^{i\mathbf{qr}}|\nu,\pi_z,m\rangle\right]_{q=q_\alpha}\langle\nu,\pi_z,m|k_x(k_y^2-k_z^2)|1\mathrm{s}\rangle G_{\nu;m}\right|^2, \tag{A.3}$$

where the phonon matrix element is evaluated at a wavevector q magnitude corresponding to the Zeeman energy $q = q_\alpha \equiv |g\mu B|/\hbar s_\alpha$. In the following sections, we will evaluate Eq. (A.3) using numerically calculated functions and an analytic approximation for the hydrogenic wavefunctions in a magnetic field.

A.3.2 Numerical calculation of admixture spin-relaxation rate

For the two matrix elements in Eq. (A.3), the integrals over the azimuthal angle of the position vector $\mathbf{r}$ can be performed analytically. This greatly speeds the evaluation time and improves the accuracy of the numerical calculation. The wave functions are written in cylindrical coordinates as $\langle\mathbf{r}|\nu,\pi_z,m\rangle = \Phi_{\nu,\pi_z,m}(\rho,z)e^{im\phi}$, where ρ is the radial coordinate, z the axial coordinate and ϕ the azimuthal angle. By transforming the differential operators into cylindrical coordinates and integrating over ϕ, we find

$$\langle\nu,\pi_z,\pm1|\,k_x(k_y^2-k_z^2)\,|1\mathrm{s}\rangle = -\frac{\pi}{4}\int\rho\,d\rho\,dz\,\Phi_{\nu,\pi_z,\pm1}\left[\frac{1}{\rho^2}\partial_\rho - \frac{1}{\rho}\partial_\rho^2 - \partial_\rho^3 + 4\partial_\rho\partial_z^2\right]\Phi_{1\mathrm{s}}, \\ \langle\nu,\pi_z,\pm3|\,k_x(k_y^2-k_z^2)\,|1\mathrm{s}\rangle = -\frac{\pi}{4}\int\rho\,d\rho\,dz\,\Phi_{\nu,\pi_z,\pm3}\left[\frac{3}{\rho^2}\partial_\rho - \frac{3}{\rho}\partial_\rho^2 + \partial_\rho^3\right]\Phi_{1\mathrm{s}}, \tag{A.4}$$

and that the matrix element is zero for any other excited state magnetic quantum number, as it must be by symmetry.

Similarly, for the matrix element $\langle\nu,\pi_z,m|e^{i\mathbf{qr}}|1\mathrm{s}\rangle$, we note that aligning the $\phi = 0$ plane along $\mathbf{q}$ results in multiplying the integrand by a phase $\exp(-im\phi_q)$, where ϕ_q is the azimuthal angle of the phonon wavevector $\mathbf{q}$. The ϕ integral can then be performed analytically with the help of a Bessel function identity. Using a few additional simplifications involving

the z-parity of the wave functions, the matrix element becomes

$$\langle \nu, \pi_z, m | e^{i\mathbf{qr}} | 1\mathrm{s} \rangle = 4\pi\, e^{-im\phi_q} \int_0^\infty \rho\, d\rho \int_0^\infty dz \cdot \\ \Phi_{\nu,\pi_z,m} \Phi_{1\mathrm{s}} \cos(z\, q \cos\theta_q) J_m(\rho\, q \sin\theta_q), \tag{A.5}$$

where θ_q is the polar angle of the wavevector $\mathbf{q}$, and J_m is the mth Bessel function of the first kind.

Lastly, we evaluate the integral over the phonon azimuthal angle ϕ_q in Eq. (A.3). We additionally note that $m = \pm 1$ states cannot interfere with $m = \pm 3$ states due to the $e^{-im\phi_q}$ factor in Eq. (A.5). We thus arrive at the expression for T_1 via the admixture mechanism,

$$\frac{1}{T_1} = F_{ph} \frac{\gamma^2 |g\mu B|}{2\pi\hbar^2\rho} \int \sin\theta_q d\theta_q \sum_\alpha \sum_{m=1,-3} \\ \left| \sum_{\nu=1}^{\infty} \left[\langle 1\mathrm{s} | e^{i\mathbf{qr}} | \nu, \pi_z, m \rangle \right]_{\phi_q=0}^{q=q_\alpha} \langle \nu, \pi_z, m | \, k_x (k_y^2 - k_z^2) \, | 1\mathrm{s} \rangle \right|^2 P_\alpha(\theta_q) \,, \tag{A.6}$$

where the phonon matrix element is evaluated at the wavevector corresponding to the Zeeman energy and at $\phi_q = 0$ [1]. The functions $P_\alpha(\theta_q)$ describe the contributions of different phonon modes and different electron-phonon interaction mechanisms. We take into account both the piezoelectric interaction with longitudinal and transverse modes, Eq. (3.10), as well as the deformation potential interaction. The latter is described by the Hamiltonian [96, 98]

$$U_{ph}^{(dp)}(\mathbf{r}) = \sqrt{\frac{\hbar}{2\rho\omega_{\mathbf{q}\alpha}}} e^{i\mathbf{qr}} q (\xi_i \hat{e}_i) D b_{\mathbf{q}\alpha}^\dagger + \text{c.c.}, \tag{A.7}$$

where D is the deformation potential constant and involves longitudinal phonons only. As a result, disregarding the interference of piezo and deformation potential interactions, we

[1] Since ϕ_q just adds a phase, the expression is valid for any choice of ϕ_q.

have

$$
\begin{aligned}
P_1(\theta_q) &= \frac{9e^2h_{14}^2}{s_l^3}\cos^2\theta_q\sin^4\theta_q\ , \\
P_2(\theta_q) &= \frac{e^2h_{14}^2}{8s_t^3}(27+28\cos 2\theta_q+9\cos 4\theta_q)\ , \\
P_3(\theta_q) &= \frac{2(g\mu B)^2D^2}{\hbar^2 s_l^5}.
\end{aligned}
\tag{A.8}
$$

The simplified matrix elements Eq. (A.4), (A.5) are calculated numerically using standard procedures. The scripts have been made readily available [2].

A.3.3 Admixture mechanism in moderate magnetic fields

In the regime of moderate fields, when $l_b \sim a_B^*$, we take into account the modification of the excited state wavefunctions by the magnetic field. In this regime, admixture with the lowest energy excited states (p-shell states) is allowed and we will further take into account only these two states assuming a Gaussian form of the wavefunctions:

$$
\begin{aligned}
\psi_{1\mathrm{s}} &= \frac{1}{\pi^{3/4}l_\rho\sqrt{l_z}}\ \exp\left(-\frac{x^2+y^2}{2(l_{\rho,1\mathrm{s}})^2}-\frac{z^2}{2(l_{z,1\mathrm{s}})^2}\right), \\
\psi_{2\mathrm{p}_\pm} &= \frac{(x\pm iy)}{\pi^{3/4}\chi^{5/2}l_\rho^2\sqrt{l_z}}\ \exp\left(-\frac{x^2+y^2}{2(l_{\rho,2\mathrm{p}})^2}-\frac{z^2}{2(l_{z,2\mathrm{p}})^2}\right).
\end{aligned}
\tag{A.9}
$$

Further, for simplicity, we will assume a proportionality $l_{\rho,2\mathrm{p}} = \chi l_{\rho,1\mathrm{s}}$ and $l_{z,2\mathrm{p}} = \chi l_{z,1\mathrm{s}}$ for the analytic wavefunctions. Here $l_{\rho,1\mathrm{s}} = [1/(a_B^*)^2 + 1/(2l_b^2)]^{-1/2}$ and $l_{z,1\mathrm{s}} = a_B^*$ are the wave function effective sizes in the (xy)-plane and the z-direction, respectively. At zero field, $l_{\rho,1\mathrm{s}}$ is just the Bohr radius and both lengths coincide. A non-zero magnetic field shrinks the wave function in the (xy)-plane leading to anisotropy of the 1s-state with $l_{\rho,1\mathrm{s}} < l_{z,1\mathrm{s}}$. In the limit of very strong fields $l_{\rho,1\mathrm{s}} = \sqrt{2}l_b$, in agreement with the free-electron wave function in a magnetic field in the symmetric gauge. The exact numerical wavefunctions (Appendix A.2) are used to determine the value of χ for the analytic wavefunctions, Eq. (A.9). To determine the best value of χ, we numerically optimized the overlap integral between the analytic wavefunctions, Eq. (A.9), and the numerical ones. The ratio of the wavefunction size for

[2] See supplemental materials at `https://link.aps.org/doi/10.1103/PhysRevB.94.125401` for analysis scripts.

the $2p_{-1}$ and 1s states are shown in Fig. A.3. In the figure we have also shown the limiting values of β for which the experimental high-field dependence is observed. By averaging over the ratio of lengths for ρ and z directions, we obtain a best-choice χ of 1.5, 1.7 and 2.2 for GaAs, InP, and CdTe respectively.

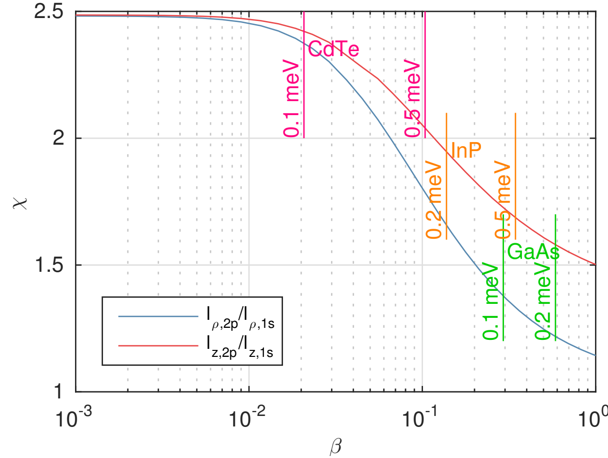

Figure A.3: The overlap integral between the Gaussian approximation for the wavefunction, Eq. (A.9), and the numerical solution was maximized as a function of β. The ratio of the radial and axial Gaussian sizes is plotted as a function of B. Also shown are the experimental limits of the "high-field" regime where T_1 goes as $B^{-\nu}$ for the three different materials. Using these limits, reasonable choices of χ are 1.5, 1.7 and 2.2 for GaAs, InP, and CdTe respectively.

To obtain the matrix element $M_{\downarrow\uparrow}$ given by Eq. (3.8), we need to calculate $\langle 2p_\pm|\partial_x(\partial_y^2-\partial_z^2)|1\mathrm{s}\rangle$ and $\langle 1\mathrm{s}|e^{i\mathbf{qr}}|2\mathrm{p}_\pm\rangle$. Utilizing the Gaussian wave functions we assumed, Eq. (A.9), the results for the integrals are

$$\langle 2\mathrm{p}_\pm|\partial_x(\partial_y^2-\partial_z^2)|1\mathrm{s}\rangle = \frac{\sqrt{2}\chi^{5/2}}{(1+\chi^2)^{7/2}l_b^2 l_\rho}\,, \tag{A.10a}$$

$$\langle 2\mathrm{p}_\pm|\partial_y(\partial_z^2-\partial_x^2)|1\mathrm{s}\rangle = \pm\frac{i\sqrt{2}\chi^{5/2}}{(1+\chi^2)^{7/2}l_b^2 l_\rho}\,. \tag{A.10b}$$

and

$$\langle 1\mathrm{s}|e^{i\mathbf{qr}}|2p_\pm\rangle \;=\; i2\sqrt{2}\left(\frac{\chi}{1+\chi^2}\right)^{5/2}(q_x \pm iq_y)l_\rho \cdot \exp\left(-\frac{\chi^2}{2(1+\chi^2)}[(q_x^2+q_y^2)l_\rho^2 + q_z^2 l_z^2]\right) . \tag{A.11}$$

Note that nonzero matrix elements in Eq. (A.10) are proportional to B, so that they vanish in the limit of low fields (this regime is considered below in Appendix **??**). As the magnetic fields in our experiments are not very strong, the change of the characteristic length is small and we can neglect the difference between l_ρ and l_z in the exponential part of Eq. (A.11) by setting $l_{z,1\mathrm{s}} = l_{\rho,1\mathrm{s}} = l$. In fact, the wavefunction size l is important only when the long-wavelength approximation for the electron-acoustic phonon interaction fails, in which case the result may be quite sensitive to the overall shape of the wave function, and, additionally, the deformation-potential interaction may be important.

Substituting these into Eqs. (3.7),(3.8), the relaxation rate is

$$\frac{1}{T_1} = \frac{32}{\pi\hbar\rho}\frac{\chi^{10}}{(1+\chi^2)^{12}}\frac{\gamma^2(eh_{14})^2}{l_b^4}\left(\frac{1}{\Delta E_R} - \frac{1}{\Delta E_R + \hbar\omega_c}\right)^2 \cdot F_{ph}\sum_\alpha \frac{q_\alpha^3}{s_\alpha^2}\exp\left(-\frac{\chi^2}{1+\chi^2}q_\alpha^2 l^2\right)\left\langle \sin^2\theta_q a_{\mathbf{q},\alpha}^2\right\rangle_\Omega . \tag{A.12}$$

The quantity $\Delta E = E_{2\mathrm{p}_} - E_{1\mathrm{s}}$. Numerically we find that $\Delta E = 3/4\mathcal{E}_{Ry}^*$ is a good approximation across the entire experimental range of fields (see Fig. A.2).

For longitudinal phonons we have

$$\left\langle \sin^2\theta_q a_{q,l}^2\right\rangle_\Omega = \frac{8}{35} , \tag{A.13}$$

while for transverse modes

$$\left\langle \sin^2\theta_q a_{q,t}^2\right\rangle_\Omega = \frac{32}{105} . \tag{A.14}$$

Substituting these integrals into the Eq. (A.12), the final result for the spin relaxation rate

is

$$\frac{1}{T_1} = \frac{256\chi^{10}}{35(1+\chi^2)^{12}} \frac{\gamma^2 e^4 h_{14}^2 (g\mu)^3 B^5}{\pi\rho\hbar^6} \left(\frac{1}{\Delta E_R} - \frac{1}{\Delta E_R + \hbar\omega_c}\right)^2 F_{ph} \cdot \left[\frac{1}{s_l^5}\exp\left(-\frac{\chi^2 q_l^2 l^2}{1+\chi^2}\right) + \frac{4}{3s_t^5}\exp\left(-\frac{\chi^2 q_t^2 l^2}{1+\chi^2}\right)\right], \tag{A.15}$$

in agreement with Eq. (3.13) of the main text.

We note that in the limit of very strong magnetic fields where $l_b \ll a_B^*$ and $\hbar\omega_c \gg \Delta E_R$ one has to take into account the modification of the separation between the ground and the excited states by the magnetic field. As a rough estimate one may replace ΔE_R in Eq. (A.15) by $\hbar\omega_c$, in which case, within the LWA, one has $T_1 \propto B^3$. Our estimates show that this limit is not fulfilled in any sample for the magnetic fields under study.

Finally, we briefly analyze the deformation potential interaction in which case instead of Eq. (3.10) one has Eq. (A.7). It follows from Eq. (A.7) that transition can be assisted by the logitudinal acoustic phonons only. Making use of the analytical form of the wavefunctions, Eq. (A.9), and the matrix elements of the Dresselhaus spin-orbit interaction, Eq. (A.10), as well as Eq. (A.11) we obtain

$$\frac{1}{T_1} = \frac{64\chi^{10}}{3\pi\hbar\rho(1+\chi^2)^{12}} \left(\frac{g\mu B}{\hbar s_l}\right)^5 \frac{\gamma^2 D^2}{s_l^2 l_b^4} F_{ph} \cdot \left(\frac{1}{\Delta E_R} - \frac{1}{\Delta E_R + \hbar\omega_c}\right)^2 \exp\left(-\frac{\chi^2 q_l^2 l^2}{1+\chi^2}\right). \tag{A.16}$$

The angular integrations over the phonon wavevectors has been carried out, as before, neglecting the difference between $l_{\rho,1\mathrm{s}}$ and $l_{z,1\mathrm{s}}$ in the exponent and using the expression $\langle(\xi_i\hat{e}_i)^2(\xi_x^2+\xi_y^2)\rangle_\Omega = 2/3$. The analysis shows that the deformation potential contribution is much smaller than the piezo-interaction, Eq. (A.15) for the relevant magnetic fields. The contribution from the deformation potential interaction is more important than the piezo-interaction at high fields due to its stronger B-field dependence. The crossover field for GaAs is about 40 T, which is much larger than the magnetic fields in this study. The crossover fields for InP and CdTe are 9.1 T and 3.9 T. Although deformation potential interaction for these two materials is comparable to the piezo-interaction at the fields achievable in our experiment, it is still much weaker than the direct spin-phonon interaction.

A.4 *Spin relaxation via the direct spin-phonon mechanism*

A.4.1 General expression for the direct spin-phonon spin-relaxation rate

The direct spin-phonon interaction Hamiltonian [94, 177, 85] is

$$U_{dir} = \frac{\hbar v_0}{2}[\sigma_x(u_{xy}k_y - u_{xz}k_z) + \sigma_y(u_{yz}k_z - u_{xy}k_x)], \tag{A.17}$$

where we ignore the σ_z term because it does not contribute to spin relaxation, $\mathbf{k} = -i\boldsymbol{\nabla} - (e/\hbar)\mathbf{A}$, and we use the symmetric gauge $\mathbf{A} = (-By/2, Bx/2, 0)$. The deformation tensor u_{ij} due to phonon $\mathbf{q}, \alpha$ is

$$u_{ij}^{\mathbf{q},\alpha} = \sqrt{\frac{\hbar}{2\rho\omega_{\mathbf{q},\alpha}}} e^{i(\mathbf{qr}-\omega_{\mathbf{q},\alpha}t)} \frac{i(\hat{e}_i^{(\mathbf{q},\alpha)}q_j + \hat{e}_j^{(\mathbf{q},\alpha)}q_i)}{2} b^\dagger_{\mathbf{q},\alpha} + \text{c.c.} \tag{A.18}$$

where $\boldsymbol{e}_\alpha$ is the polarization of phonon mode α:

$$\begin{aligned} \mathbf{e}_l &= q^{-1}[q_x, q_y, q_z], \\ \mathbf{e}_{t_1} &= (q_x^2 + q_y^2)^{-1/2}[q_y, -q_x, 0], \\ \mathbf{e}_{t_2} &= q^{-1}(q_x^2 + q_y^2)^{-1/2}[q_xq_z, q_yq_z, -(q_x^2 + q_y^2)]. \end{aligned} \tag{A.19}$$

Subscripts t_1 and t_2 denote two degenerate transverse modes. The relaxation rate $\Gamma_{\downarrow\uparrow}$ is found from Eq. (3.8) using

$$M_{\downarrow\uparrow} = \langle 1\text{s}, \downarrow | U_{dir} | 1\text{s}, \uparrow\rangle \ . \tag{A.20}$$

According to the general principles of quantum mechanics, the momentum operator and deformation tensor in Eq. (A.17) must be symmetrized, i.e. $u_{ij}k_l \to \{u_{ij}, k_l\}$, where $\{a, b\} = (ab + ba)/2$ [50, 178, 179]. Due to this symmetrization and the fact that the ground state is a localized state, all terms with k_z integrate to zero. Further simplifications yield

$$\langle 1\text{s}, \downarrow | U_{dir} | 1\text{s}, \uparrow\rangle = i\frac{\hbar v_0}{4}\sqrt{\frac{\hbar}{2\rho\omega_{\mathbf{q},\alpha}}} \left(\hat{e}_x^{(\mathbf{q},\alpha)}q_y + \hat{e}_y^{(\mathbf{q},\alpha)}q_x\right) \times$$
$$[\langle 1\text{s}|\{\exp(i\mathbf{qr}), k_y\}|1\text{s}\rangle - i\langle 1\text{s}|\{\exp(i\mathbf{qr}), k_x\}|1\text{s}\rangle] \,,$$

$$\begin{aligned}\langle 1\mathrm{s}|\{\exp(i\mathbf{qr}),k_x\}|1\mathrm{s}\rangle &= \frac{eB}{2\hbar}\langle 1\mathrm{s}|\exp(i\mathbf{qr})y|1\mathrm{s}\rangle\,, \\ \langle 1\mathrm{s}|\{\exp(i\mathbf{qr}),k_y\}|1\mathrm{s}\rangle &= -\frac{eB}{2\hbar}\langle 1\mathrm{s}|\exp(i\mathbf{qr})x|1\mathrm{s}\rangle\,.\end{aligned} \tag{A.21}$$

Substituting Eq. (A.20) into Eq. (3.7) and taking the phonon factor F_{ph} into consideration, we obtain the general expression for the spin-relaxation rate

$$\frac{1}{T_1} = F_{ph}\frac{v_0^2 e^2 B^2}{2^9\pi^2\hbar\rho}\sum_\alpha \frac{q_\alpha^3}{s_\alpha^2}\int d\Omega_q \left|\,\left(\hat{e}_x^{\mathbf{q},\alpha}\xi_y + \hat{e}_y^{\mathbf{q},\alpha}\xi_x\right)\cdot\langle 1\mathrm{s}|\exp(i\mathbf{q}_\alpha\mathbf{r})(x-iy)|1\mathrm{s}\rangle\right|^2, \tag{A.22}$$

which can be evaluated either numerically or using an analytic approximation.

A.4.2 Numerical calculation of direct spin-phonon spin-relaxation rate

Similar to Appendix A.3.2, the azimuthal part of the integral $\langle 1\mathrm{s}|\exp(i\mathbf{q}_\alpha\mathbf{r})(x-iy)|1\mathrm{s}\rangle$ can be calculated analytically to simplify the numerical calculation. We introduce the notation for this matrix element:

$$\kappa_\alpha(\theta_q) = e^{i\phi_q}\langle 1\mathrm{s}|e^{i\mathbf{q}_\alpha\mathbf{r}}(x-iy)|1\mathrm{s}\rangle,$$

and obtain

$$\kappa_\alpha(\theta_q) = 4\pi\int_0^\infty \rho^2\,d\rho\int_0^\infty dz\,\Phi_{1\mathrm{s}}^2(\rho,z)\cdot\cos(z\,q_\alpha\cos\theta_q)J_1(\rho\,q_\alpha\sin\theta_q). \tag{A.23}$$

The simplified expression for the spin-relaxation rate is

$$\frac{1}{T_1} = F_{ph}\frac{\nu_0^2 e^2 B^2}{2^9\pi\hbar\rho}\int_0^\pi d\theta_q\,\sin^3\theta_q\cdot\left[\sin^2\theta_q\frac{q_l^3}{s_l^2}|\kappa_l|^2 + (1+\cos^2\theta_q)\frac{q_t^3}{s_t^2}|\kappa_t|^2\right], \tag{A.24}$$

which can be calculated numerically using standard procedures.

A.4.3 Analytic calculation of direct spin-phonon spin-relaxation rate

To derive an analytical result we use trial wavefunctions of a Gaussian or exponential form. First, we approximate the ground state wave function by a Gaussian

$$\psi_{1s} = \frac{1}{(\sqrt{\pi}l)^{3/2}} e^{-r^2/(2l^2)}, \tag{A.25}$$

with $l = [1/(a_B^*)^2 + 1/(2l_b^2)]^{-1/2}$. The matrix element can be found analytically,

$$\langle 1s| \exp(i\mathbf{qr}) r_j |1s\rangle = \frac{1}{2} i q_j l^2 e^{-q^2 l^2/4}\,, \tag{A.26}$$

where $j = x, y$.

Using Eqs. (3.7), (A.20) we obtain the relaxation rate assuming that the spin-up state has a higher energy as compared with the spin-down one

$$\Gamma_{\downarrow\uparrow} = \frac{(N_{ph}+1)v_0^2}{256\pi\rho\hbar}(eBl^2)^2 \sum_\alpha \frac{(g\mu B)^5}{\hbar^5 s_\alpha^7} I_\alpha e^{-q_\alpha^2 l^2/2}, \tag{A.27}$$

$$I_\alpha = \left\langle \left(\hat{e}_x^{\mathbf{q},\alpha}\xi_y + \hat{e}_y^{\mathbf{q},\alpha}\xi_x\right)^2 \xi_x^2 \right\rangle_\Omega . \tag{A.28}$$

The integrals over phonon angle for the longitudinal and both transverse modes are $I_l = 4/35$ and $I_t = 16/105$. Taking into account the phonon factor F_{ph}, the final result for the relaxation rate by the direct spin-phonon process is

$$\frac{1}{T_1} = \frac{1}{2240\pi}\frac{(ev_0 l^2)^2 (g\mu)^5 B^7}{\rho\hbar^6} \cdot \left(\frac{e^{-q_l^2 l^2/2}}{s_l^7} + \frac{4e^{-q_t^2 l^2/2}}{3s_t^7}\right) F_{ph}. \tag{A.29}$$

Another possible choice of wave function for the donor-bound electron is an exponential

$$\psi_{1s} = \frac{1}{\sqrt{\pi l^3}} e^{-r/l}. \tag{A.30}$$

For this wave function,

$$\langle 1s| \exp(i\mathbf{qr}) r_j |1s\rangle = \frac{i\, l^2 q_j}{(1+q^2 l^2/4)^3}\,. \tag{A.31}$$

The relaxation rate using an exponential wave function is the same as Eq. (A.29) with $\exp(-q_\alpha^2 l^2/2)$ replaced by $4/(1+q_\alpha^2 l^2/4)^6$, in agreement with Eq. (3.15) of the main text.

We note that in the presence of a magnetic field the form of the donor-bound electron functions depends on the gauge, which calls for special care in evaluating the matrix elements in Eq. (A.21). Particularly, Eqs. (A.25) and (A.30) are valid in the symmetric gauge. For instance, in the Landau gauge, where $\mathbf{A} = (0, Bx, 0)$, Eqs. (A.25) and (A.30) acquire extra phase factors $\exp[ieBxy/(2\hbar)]$. Taking these phase factors into account one can readily check that Eqs. (A.21) and, correspondingly, Eqs. (A.27), (A.29) and (3.15) are gauge invariant.

Appendix B

TWO ROUTINES TO MAKE ZNO THIN FILM USING FIB

B.1 Routine 1: top milling

For the first routine, the ZnO sample is milled from the top side using FIB. In chapter 5, we use this method to prepare two different ZnO thin films. The first one is from a Tokyo Denpa substrate with 0.7 µm epilayer and the second one is from a bare Tokyo Denpa substrate.

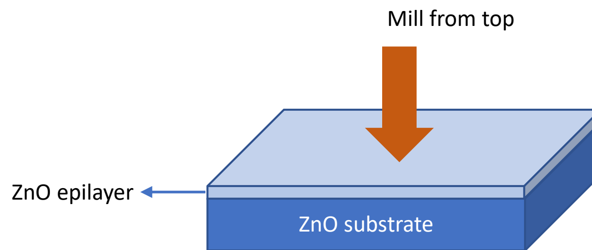

Figure B.1: Illustration of the top milling.

The fabrication procedure is shown below. The sample used here is the Tokyo Denpa substrate with 0.7 µm epilayer. The pits seen on the surface of the ZnO crystal are due to defects during the epitaxial growth, shown in Fig. (a). Before milling, an ∼1 µm thick platinum layer is deposited on top of the surface for protection from ion damage. Though this platinum layer can protect the ZnO from ion damage in the latter steps, the first several µm region below the platinum has already been directly exposed to ions as the platinum deposition requires ion exposure. Then, two trenches are cut on the two sides of the platinum layer (Fig. (b)). The thin ZnO film left in the middle is the part we want to transfer to a metal grid.

SEM images taken during the fabrication process

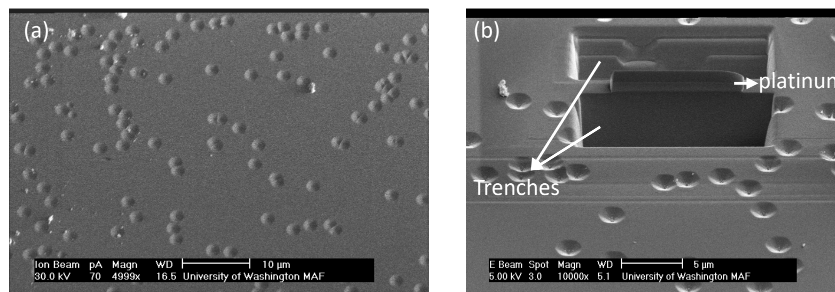

Then, a transfer pin is inserted and attached to the edge of the ZnO film using platinum deposition. The surrounding of the thin film is cut so that it can be detached from the bulk ZnO crystal (Fig. (c)). The thin film is then picked up and ready for transferring to the metal grid (Fig. (d)).

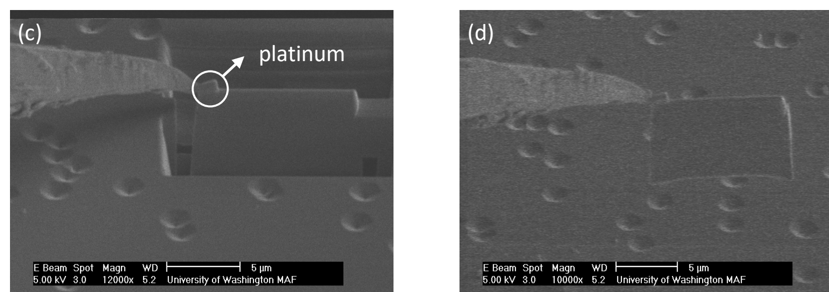

The thin film is transferred and attached to a metal grid with platinum deposition (Fig. (e)). The transfer pin is detached using FIB. Then both sides of the ZnO film are attached to the metal grid with platinum (Fig. (f)).

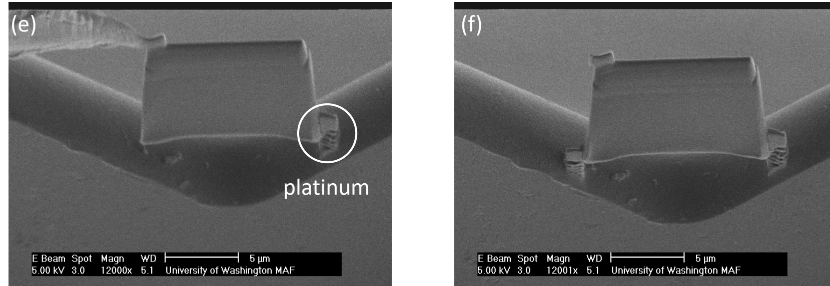

The thickness of the thin film can be further reduced by ion milling with low current beam (Fig. (h)). The surface damage on the two sides is reduced by this final polishing process. We note that the top ∼1 µm region in the thin film is platinum.

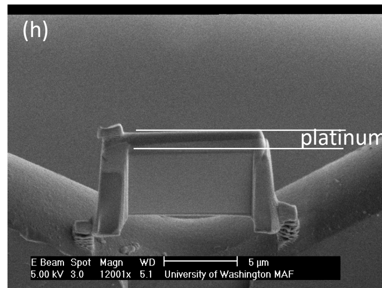

B.2 *Routine 2: side milling*

For the second routine, the ZnO sample is milled from the side surface using FIB. In chapter 5, we use this method to prepare two different ZnO thin films. Both of them are from a Tokyo Denpa substrate with 3 µm epilayer. With this side milling, we extract ZnO thin films purely from the epilayer region. The first ZnO thin film is transferred to a Si substrate and the second thin film is transferred to a metal grid similar as the first routine. In this two thin films, we can directly observe the PL signals from donors in the epilayer.

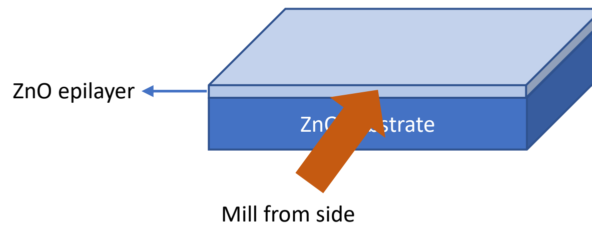

Figure B.2: Illustration of the side milling.

The fabrication procedure is shown below. The sample used here is the Tokyo Denpa substrate with 3 µm epilayer. Before milling, an ∼1 µm thick platinum layer is deposited on the side surface of the crystal for protection from ion damage. Similar as the first routine, though this platinum layer can protect the ZnO from ion damage in the latter steps, the first several µm region below the platinum has already been directly exposed. A trench is then cut on the side surface of the crystal. Figure (a) and (b) are the SEM images taken at different tilting angles of the crystal.

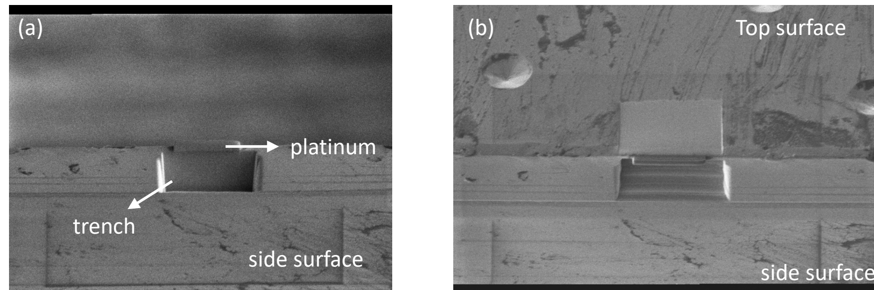

Then, a transfer pin is inserted and attached to the edge of the ZnO film using platinum deposition. The surrounding of the thin film is cut so that it can be detached with the bulk ZnO crystal (Fig. (c-d)).

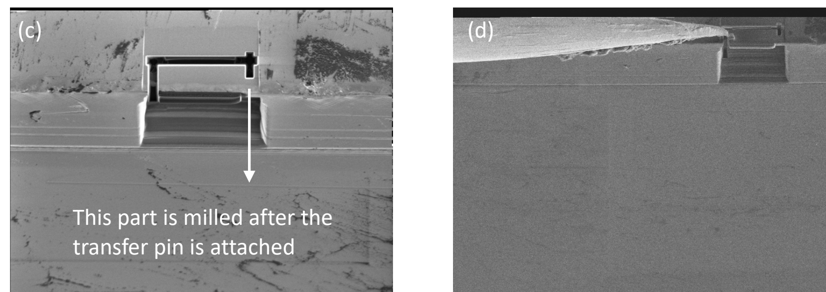

After detached from the bulk crystal, the thin film is transferred and attached to a silicon substrate with platinum deposition (Fig. (e)). Then the transfer pin is detached using FIB (Fig. (f)). We are not able to do a final polishing for the thin film attached to a Si substrate. The advantage to put the ZnO film on a silicon substrate is the ease for further treatments such as etching or annealing.

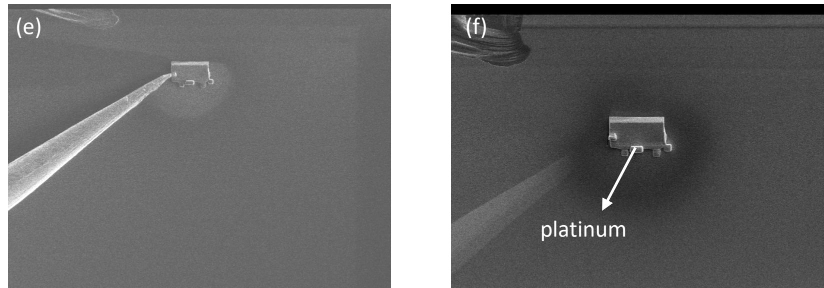

In this section, we only show the procedure to transfer the side-milled thin film to a Si substrate. The procedure to transfer it to a metal grid is similar as the first routine so we do not show it here.

BIBLIOGRAPHY

[1] K. Saeedi, S. Simmons, J. Z. Salvail, P. Dluhy, H. Riemann, N. V. Abrosimov, P. Becker, H.-J. Pohl, J. J. L. Morton, and M. L. W. Thewalt, “Room-temperature quantum bit storage exceeding 39 minutes using ionized donors in silicon-28,” *Science*, vol. 342, no. 6160, p. 830, 2013.

[2] T. F. Watson, B. Weber, Y.-L. Hsueh, L. C. L. Hollenberg, R. Rahman, and M. Y. Simmons, “Atomically engineered electron spin lifetimes of 30 s in silicon,” *Sci. Adv.*, vol. 3, no. 3, p. e1602811, 2017.

[3] J. T. Muhonen, A. Laucht, S. Simmons, J. P. Dehollain, R. Kalra, F. E. Hudson, S. Freer, K. M. Itoh, D. N. Jamieson, J. C. McCallum, A. S. Dzurak, and A. Morello, “Quantifying the quantum gate fidelity of single-atom spin qubits in silicon by randomized benchmarking,” *J. Phys.: Condens. Matter*, vol. 27, no. 15, p. 154205, 2015.

[4] S. C. Benjamin, B. W. Lovett, and J. M. Smith, “Prospects for measurement-based quantum computing with solid state spins,” *Laser & Photonics Review*, vol. 3, pp. 556–574, Nov. 2009.

[5] N. H. Nickerson, J. F. Fitzsimons, and S. C. Benjamin, “Freely scalable quantum technologies using cells of 5-to-50 qubits with very lossy and noisy photonic links,” *Phys. Rev. X*, vol. 4, p. 041041, Dec 2014.

[6] G. Tosi, F. A. Mohiyaddin, V. Schmitt, S. Tenberg, R. Rahman, G. Klimeck, and A. Morello, “Silicon quantum processor with robust long-distance qubit couplings,” *Nat. Commun.*, vol. 8, no. 450, p. 450, 2017.

[7] N. Sangouard, C. Simon, H. de Riedmatten, and N. Gisin, “Quantum repeaters based on atomic ensembles and linear optics,” *Rev. of Mod. Phys.*, vol. 83, p. 33, Mar. 2011.

[8] H. J. Briegel, W. Dür, J. I. Cirac, and P. Zoller, “Quantum Repeaters: The Role of Imperfect Local Operations in Quantum Communication,” *Phys. Rev. Lett.*, vol. 81, pp. 5932–5935, Dec. 1998.

[9] K.-M. C. Fu, W. Yeo, S. Clark, C. Santori, C. Stanley, M. Holland, and Y. Yamamoto, “Millisecond spin-flip times of donor-bound electrons in GaAs,” *Phys. Rev. B*, vol. 74, p. 121304, 2006.

[10] K.-M. C. Fu, S. M. Clark, C. Santori, C. R. Stanley, M. C. Holland, and Y. Yamamoto, "Ultrafast control of donor-bound electron spins with single detuned optical pulses," *Nature Physics*, vol. 4, p. 780, Aug. 2008.

[11] S. M. Clark, K.-M. C. Fu, Q. Zhang, T. D. Ladd, C. Stanley, and Y. Yamamoto, "Ultrafast Optical Spin Echo for Electron Spins in Semiconductors," *Phys. Rev. Lett.*, vol. 102, p. 247601, June 2009.

[12] K.-M. C. Fu, C. Santori, C. Stanley, M. C. Holland, and Y. Yamamoto, "Coherent population trapping of electron spins in a high-purityn-type GaAs semiconductor," *Physical Review Letters*, vol. 95, oct 2005.

[13] X. Linpeng, T. Karin, M. V. Durnev, R. Barbour, M. M. Glazov, E. Y. Sherman, S. P. Watkins, S. Seto, and K.-M. C. Fu, "Longitudinal spin relaxation of donor-bound electrons in direct band-gap semiconductors," *Physical Review B*, vol. 94, p. 125401, sep 2016.

[14] X. Linpeng, M. L. Viitaniemi, A. Vishnuradhan, Y. Kozuka, C. Johnson, M. Kawasaki, and K.-M. C. Fu, "Coherence properties of shallow donor qubits in ZnO," *Physical Review Applied*, vol. 10, p. 064061, dec 2018.

[15] X. Linpeng, T. K. andd Mikhail V. Durnev, M. M. Glazov, R. Schott, A. D. Wieck, A. Ludwig, , and K.-M. C. Fu, "Optical control and coherence measurements of acceptor bound holes in strained gaas," *in preparation*, 2020.

[16] H. J. Kimble, "The quantum internet," *Nature*, vol. 453, pp. 1023–1030, 2008.

[17] P. C. Humphreys, N. Kalb, J. P. J. Morits, R. N. Schouten, R. F. L. Vermeulen, D. J. Twitchen, M. Markham, and R. Hanson, "Deterministic delivery of remote entanglement on a quantum network," *Nature*, vol. 558, p. 268, June 2018.

[18] G. Waldherr, Y. Wang, S. Zaiser, M. Jamali, T. Schulte-Herbruggen, H. Abe, T. Ohshima, J. Isoya, J. F. Du, P. Neumann, and J. Wrachtrup, "Quantum error correction in a solid-state hybrid spin register," *Nature*, vol. 506, pp. 204–207, Feb. 2014.

[19] H. Bernien, B. Hensen, W. Pfaff, G. Koolstra, M. Blok, L. Robledo, T. Taminiau, M. Marhkham, D. Twitchen, L. Childress, and R. Hanson, "Heralded entanglement between solid-state qubits separated by three metres," *Nature*, vol. 497, p. 86, 2013.

[20] A. Delteil, Z. Sun, W. bo Gao, E. Togan, S. Faelt, and A. Imamoğlu, "Generation of heralded entanglement between distant hole spins," *Nature Physics*, vol. 12, p. 218, dec 2015.

[21] D. Brunner, B. D. Gerardot, P. A. Dalgarno, G. Wüst, K. Karrai, N. G. Stoltz, P. M. Petroff, and R. J. Warburton, "A coherent single-hole spin in a semiconductor," *Science*, vol. 325, p. 70, jul 2009.

[22] J. H. Prechtel, A. V. Kuhlmann, J. Houel, A. Ludwig, S. R. Valentin, A. D. Wieck, and R. J. Warburton, "Decoupling a hole spin qubit from the nuclear spins," *Nature Materials*, vol. 15, p. 981, jul 2016.

[23] X. Xu, B. Sun, P. R. Berman, D. G. Steel, A. S. Bracker, D. Gammon, and L. J. Sham, "Coherent population trapping of an electron spin in a single negatively charged quantum dot," *Nature Physics*, vol. 4, p. 692, aug 2008.

[24] K. D. Greve, P. L. McMahon, D. Press, T. D. Ladd, D. Bisping, C. Schneider, M. Kamp, L. Worschech, S. Höfling, A. Forchel, and Y. Yamamoto, "Ultrafast coherent control and suppressed nuclear feedback of a single quantum dot hole qubit," *Nature Physics*, vol. 7, p. 872, aug 2011.

[25] H. Watzinger, J. Kukučka, L. Vukušić, F. Gao, T. Wang, F. Schäffler, J.-J. Zhang, and G. Katsaros, "A germanium hole spin qubit," *Nature Communications*, vol. 9, p. 3902, sep 2018.

[26] R. Maurand, X. Jehl, D. Kotekar-Patil, A. Corna, H. Bohuslavskyi, R. Laviéville, L. Hutin, S. Barraud, M. Vinet, M. Sanquer, and S. D. Franceschi, "A CMOS silicon spin qubit," *Nature Communications*, vol. 7, p. 13575, nov 2016.

[27] T. Karin, R. J. Barbour, C. Santori, Y. Yamamoto, Y. Hirayama, and K.-M. C. Fu, "Radiative properties of multicarrier bound excitons in GaAs," *Phys. Rev. B*, vol. 91, p. 165204, apr 2015.

[28] D. J. Hilton and C. L. Tang, "Optical orientation and femtosecond relaxation of spin-polarized holes in GaAs," *Phys. Rev. Lett.*, vol. 89, p. 146601, sep 2002.

[29] L. Viña, T. Damen, J. Cunningham, J. Shah, and L. Sham, "Spin relaxation dynamics in GaAs quantum wells: Free carriers and excitons," *Superlattices and Microstructures*, vol. 12, p. 379, jan 1992.

[30] D. Heiss, S. Schaeck, H. Huebl, M. Bichler, G. Abstreiter, J. J. Finley, D. V. Bulaev, and D. Loss, "Observation of extremely slow hole spin relaxation in self-assembled quantum dots," *Phys. Rev. B*, vol. 76, p. 241306, dec 2007.

[31] D. V. Bulaev and D. Loss, "Spin relaxation and decoherence of holes in quantum dots," *Physical Review Letters*, vol. 95, p. 076805, aug 2005.

[32] E. J. Stanton, J. Chiles, N. Nader, G. Moody, N. Volet, L. Chang, J. E. Bowers, S. W. Nam, and R. P. Mirin, “Efficient second harmonic generation in nanophotonic GaAs-on-insulator waveguides,” *Optics Express*, vol. 28, p. 9521, mar 2020.

[33] X. Yuan, F. Weyhausen-Brinkmann, J. Martín-Sánchez, G. Piredda, V. Křápek, Y. Huo, H. Huang, C. Schimpf, O. G. Schmidt, J. Edlinger, G. Bester, R. Trotta, and A. Rastelli, “Uniaxial stress flips the natural quantization axis of a quantum dot for integrated quantum photonics,” *Nat. Commun.*, vol. 9, p. 3058, aug 2018.

[34] S. L. Chuang, *Physics of Photonic Devices.* Wiley, 2009.

[35] A. S. M. Rao and K. Narender, “Studies on thermophysical properties of CaO and MgO by γ-ray attenuation,” *Journal of Thermodynamics*, vol. 2014, p. 123478, 2014.

[36] V. K. Yang, M. Groenert, C. W. Leitz, A. J. Pitera, M. T. Currie, and E. A. Fitzgerald, “Crack formation in GaAs heteroepitaxial films on si and SiGe virtual substrates,” *J. Appl. Phys.*, vol. 93, p. 3859, apr 2003.

[37] H. M. G. A. Tholen, J. S. Wildmann, A. Rastelli, R. Trotta, C. E. Pryor, E. Zallo, O. G. Schmidt, P. M. Koenraad, and A. Y. Silov, “Active tuning of the g-tensor in InGaAs/GaAs quantum dots via strain,” *Phys. Rev. B*, vol. 99, p. 195305, may 2019.

[38] C. Testelin, F. Bernardot, B. Eble, and M. Chamarro, “Hole–spin dephasing time associated with hyperfine interaction in quantum dots,” *Physical Review B*, vol. 79, p. 195440, may 2009.

[39] B. Eble, C. Testelin, P. Desfonds, F. Bernardot, A. Balocchi, T. Amand, A. Miard, A. Lemaître, X. Marie, and M. Chamarro, “Hole–nuclear spin interaction in quantum dots,” *Phys. Rev. Lett.*, vol. 102, p. 146601, apr 2009.

[40] A. Baldereschi and N. O. Lipari, “Spherical model of shallow acceptor states in semiconductors,” *Phys. Rev. B*, vol. 8, p. 2697, sep 1973.

[41] L. M. Woods, T. L. Reinecke, and R. Kotlyar, “Hole spin relaxation in quantum dots,” *Phys. Rev. B*, vol. 69, p. 125330, mar 2004.

[42] D. Bimberg, “Anomaly of the linear and quadratic zeeman effect of an effective-mass acceptor: C in GaAs,” *Phys. Rev. B*, vol. 18, p. 1794, aug 1978.

[43] A. V. Malyshev and I. A. Merkulov, “Magnetic moment of an acceptor center in cubic semiconductors,” *Phys. Solid State*, vol. 39, p. 49, jan 1997.

[44] V. E. Kirpichev, I. V. Kukushkin, V. E. Bisti, K. von Klitzing, and K. Eberl, “Magnetooptic measurements of the cyclotron mass and g-factor of light holes in GaAs,” *Jetp Lett.*, vol. 64, p. 814, dec 1996.

[45] I. A. Merkulov, A. L. Efros, and M. Rosen, "Electron spin relaxation by nuclei in semiconductor quantum dots," *Physical Review B*, vol. 65, p. 205309, apr 2002.

[46] T. Kobayashi, J. Salfi, C. Chua, J. van der Heijden, M. G. House, D. Culcer, W. D. Hutchison, B. C. Johnson, J. C. McCallum, H. Riemann, N. V. Abrosimov, P. Becker, H.-J. Pohl, M. Y. Simmons, and S. Rogge, "Engineering long spin coherence times of spin–orbit qubits in silicon," *Nature Materials*, jul 2020.

[47] A. Jarmola, V. M. Acosta, K. Jensen, S. Chemerisov, and D. Budker, "Temperature- and magnetic-field-dependent longitudinal spin relaxation in nitrogen-vacancy ensembles in diamond," *Phys. Rev. Lett.*, vol. 108, p. 197601, May 2012.

[48] A. M. Tyryshkin, J. J. L. Morton, S. C. Benjamin, A. Ardavan, G. A. D. Briggs, J. W. Ager, and S. A. Lyon, "Coherence of spin qubits in silicon," *J. Phys.: Condens. Matter*, vol. 18, no. 21, 2006.

[49] J. Tribollet, "Theory of the electron and nuclear spin coherence times of shallow donor spin qubits in isotopically and chemically purified zinc oxide," *Eur. Phys. J. B*, vol. 72, no. 4, pp. 531–540, 2009.

[50] A. V. Khaetskii and Y. V. Nazarov, "Spin-flip transitions between Zeeman sublevels in semiconductor quantum dots," *Phys. Rev. B*, vol. 64, p. 125316, 2001.

[51] S. D. Barrett and P. Kok, "Efficient high-fidelity quantum computation using matter qubits and linear optics," *Phys. Rev. A*, vol. 71, p. 060310(R), 2005.

[52] L. Childress, J. M. Taylor, A. S. Sorensen, and M. D. Lukin, "Fault-tolerant quantum repeaters with minimal physical resources and implementations based on single-photon emitters," *Phys. Rev. A*, vol. 72, p. 52330, 2005.

[53] C. Simon, M. Afzelius, J. Appel, A. Boyer de la Giroday, J. S. Dewhurst, N. Gisin, Y. C. Hu, F. Jelezko, S. Kröll, H. J. Müller, J. Nunn, S. E. Polzik, G. J. Rarity, H. De Riedmatten, W. Rosenfeld, J. A. Shields, N. Sköld, M. R. Stevenson, R. Thew, A. I. Walmsley, C. M. Weber, H. Weinfurter, J. Wrachtrup, and J. R. Young, "Quantum memories," *Eur. Phys. J. D*, vol. 58, no. 1

[54] K. C. Fu, C. Santori, C. Stanley, M. C. Holland, and Y. Yamamoto, "Coherent population trapping of electron spins in a high-purity n-type GaAs semiconductor," *Phys. Rev. Lett.*, vol. 95, p. 187405, Oct. 2005.

[55] K. De Greve, S. M. Clark, D. Sleiter, K. Sanaka, T. D. Ladd, M. Panfilova, A. Pawlis, K. Lischka, and Y. Yamamoto, "Photon antibunching and magnetospectroscopy of a single fluorine donor in ZnSe," *Appl. Phys. Lett.*, vol. 97, no. 24, p. 241913, 2010.

[56] G. Balasubramanian, P. Neumann, D. Twitchen, M. Markham, R. Kolesov, N. Mizuochi, J. Isoya, J. Achard, J. Beck, J. Tissler, V. Jacques, P. R. Hemmer, F. Jelezko, and J. Wrachtrup, "Ultralong spin coherence time in isotopically engineered diamond," *Nat. Mater.*, vol. 8, pp. 383–387, 2009.

[57] A. M. Tyryshkin, S. Tojo, J. J. L. Morton, H. Riemann, N. V. Abrosimov, P. Becker, H. J. Pohl, T. Schenkel, M. L. W. Thewalt, K. M. Itoh, and S. A. Lyon, "Electron spin coherence exceeding seconds in high-purity silicon," *Nat. Mater.*, vol. 11, no. 2, pp. 143–147, 2012.

[58] I. A. Merkulov, A. L. Efros, and M. Rosen, "Electron spin relaxation by nuclei in semiconductor quantum dots," *Phys. Rev. B*, vol. 65, p. 205309, Apr. 2002.

[59] M. Kroutvar, Y. Ducommun, D. Heiss, M. Bichler, D. Schuh, G. Abstreiter, and J. J. Finley, "Optically programmable electron spin memory using semiconductor quantum dots," *Nature*, vol. 432, pp. 81–84, Nov. 2004.

[60] J. M. Elzerman, R. Hanson, L. H. Willems van Beveren, B. Witkamp, L. M. K. Vandersypen, and L. P. Kouwenhoven, "Single-shot read-out of an individual electron spin in a quantum dot," *Nature*, vol. 430, pp. 431–435, 07 2004.

[61] D. Heiss, M. Kroutvar, J. J. Finley, and G. Abstreiter, "Progress towards single spin optoelectronics using quantum dot nanostructures," *Solid State Commun.*, vol. 135, no. 9-10, pp. 591–601, 2005.

[62] S. Amasha, K. MacLean, I. P. Radu, D. M. Zumbühl, M. A. Kastner, M. P. Hanson, and A. C. Gossard, "Electrical control of spin relaxation in a quantum dot," *Phys. Rev. Lett.*, vol. 100, p. 046803, Jan 2008.

[63] C.-Y. Lu, Y. Zhao, A. N. Vamivakas, C. Matthiesen, S. Fält, A. Badolato, and M. Atatüre, "Direct measurement of spin dynamics in InAs/GaAs quantum dots using time-resolved resonance fluorescence," *Phys. Rev. B*, vol. 81, p. 035332, Jan 2010.

[64] F. Meier and B. Zakharchenya, *Optical orientation.* North Holland, Nov. 1984.

[65] R. I. Dzhioev, K. V. Kavokin, V. L. Korenev, M. V. Lazarev, Ya, M. N. Stepanova, B. P. Zakharchenya, D. Gammon, and D. S. Katzer, "Low-temperature spin relaxation in *n*-type GaAs," *Phys. Rev. B*, vol. 66, p. 245204, Dec. 2002.

[66] F. Berski, J. Hübner, M. Oestreich, A. Ludwig, A. D. Wieck, and M. Glazov, "Interplay of electron and nuclear spin noise in *n*-type GaAs," *Phys. Rev. Lett.*, vol. 115, p. 176601, Oct. 2015.

[67] Samples were grown by metalorganic vapour phase epitaxy at between 540 and 580˙ C using trimethylindium and either phosphine or tertiarybutylphosphine.

[68] C. R. Stanley, M. C. Holland, A. H. Kean, M. B. Stanaway, R. T. Grimes, and J. M. Chamberlain, "Electrical characterization of molecular beam epitaxial gaas with peak electron mobilities up to $\simeq 4\times10^5\text{cm}^2\text{V}^{-1}\text{s}^{-1}$," *Appl. Phys. Lett.*, vol. 58, pp. 478–480, Feb. 1991.

[69] S. Seto, A. Tanaka, Y. Masa, S. Dairaku, and M. Kawashima, "Annealing behavior of bound exciton lines in high quality CdTe," *Appl. Phys. Lett.*, vol. 53, no. 16, pp. 1524–1526, 1988.

[70] The carrier concentration was not measured but is believed to be greater than 10^{14} cm^{-3} but less than 10^{15} cm^{-3} based on measurements on samples grown from the same starting material. The lineshapes of the one LO-phonon replica of the free exciton support this; the inverse Maxwell-Boltzmann distribution of CdTe-1 is sharper than that of CdTe-2.

[71] D. A. Turton, G. D. Reid, and G. S. Beddard, "Accurate analysis of fluorescence decays from single molecules in photon counting experiments," *Anal. Chem.*, vol. 75, pp. 4182–4187, June 2003.

[72] R. P. Seisyan, "Diamagnetic excitons and exciton magnetopolaritons in semiconductors," *Semicond. Sci. Technol.*, vol. 27, no. 5, p. 053001, 2012.

[73] M. I. Dyakonov, *Spin physics in semiconductors.* Berlin, Heidelberg: Springer-Verlag, 2008.

[74] M. M. Glazov, "Spin noise of localized electrons: Interplay of hopping and hyperfine interaction," *Phys. Rev. B*, vol. 91, p. 195301, May 2015.

[75] A. V. Shumilin and V. V. Kabanov, "Kinetic equations for hopping transport and spin relaxation in a random magnetic field," *Phys. Rev. B*, vol. 92, p. 014206, Jul 2015.

[76] K. V. Kavokin, "Spin relaxation of localized electrons in n-type semiconductors," *Semicond. Sci. Technol.*, vol. 23, p. 114009, Nov. 2008.

[77] B. I. Shklovskii and A. L. Efros, *Electronic Properties of Doped Semiconductors.* Springer Series in Solid-State Sciences, Springer-Verlag Berlin Heidelberg, 1984.

[78] M. I. Dyakonov and V. I. Perel', "Optical orientation in a system of electrons and lattice nuclei in semiconductors. Theory," *JETP*, vol. 38, p. 177, Jan. 1974.

[79] M. Syperek, D. R. Yakovlev, I. A. Yugova, J. Misiewicz, I. V. Sedova, S. V. Sorokin, A. A. Toropov, S. V. Ivanov, and M. Bayer, "Long-lived electron spin coherence in CdSe/ZnSSe self-assembled quantum dots," *Phys. Rev. B*, vol. 84, p. 085304, 2011.

[80] M. Gueron, “Density of the conduction electrons at the nuclei in indium antimonide,” *Phys. Rev.*, vol. 135, pp. A200–A205, Jul 1964.

[81] E. A. Chekhovich, A. B. Krysa, M. S. Skolnick, and A. I. Tartakovskii, “Direct measurement of the hole-nuclear spin interaction in single InP/GaInP quantum dots using photoluminescence spectroscopy,” *Phys. Rev. Lett.*, vol. 106, p. 027402, Jan. 2011.

[82] C. Testelin, F. Bernardot, B. Eble, and M. Chamarro, “Hole–spin dephasing time associated with hyperfine interaction in quantum dots,” *Phys. Rev. B*, vol. 79, p. 195440, May 2009.

[83] D. Pines, J. Bardeen, and C. P. Slichter, “Nuclear polarization and impurity-state spin relaxation processes in silicon,” *Phys. Rev.*, vol. 106, pp. 489–498, May 1957.

[84] E. Abrahams, “Donor electron spin relaxation in silicon,” *Phys. Rev.*, vol. 107, pp. 491–496, July 1957.

[85] D. M. Frenkel, “Spin relaxation in GaAs-$Al_xGa_{1-x}As$ heterostructures in high magnetic fields,” *Phys. Rev. B*, vol. 43, pp. 14228–14231, 1991.

[86] L. M. Woods, T. L. Reinecke, and Y. Lyanda-Geller, “Spin relaxation in quantum dots,” *Phys. Rev. B*, vol. 66, p. 161318, Oct 2002.

[87] F. Marquardt and V. A. Abalmassov, “Spin relaxation in a quantum dot due to Nyquist noise,” *Phys. Rev. B*, vol. 71, p. 165325, Apr. 2005.

[88] M. D. Petrovićfi and N. Vukmirović, “Spin relaxation in CdTe quantum dots with a single Mn atom,” *Phys. Rev. B*, vol. 85, p. 195311, May 2012.

[89] O. Madelung, *Semiconductors: Data handbook.* Springer, 3rd ed., Jan. 2004.

[90] K. Rottner, R. Helbig, and G. Müller, “Piezoelectric constant of InP,” *Appl. Phys. Lett.*, vol. 62, pp. 352–353, Jan. 1993.

[91] J. M. Jancu, R. Scholz, de Andrada, and G. C. L. Rocca, “Atomistic spin-orbit coupling and k·p parameters in III-V semiconductors,” *Phys. Rev. B*, vol. 72, p. 193201, 2005.

[92] http://www.ioffe.ru/SVA/NSM/Semicond/, 2016. Accessed: 2016-05-16.

[93] O. Madelung, U. Rössler, and M. Schulz, eds., *II-VI and I-VII Compounds; Semimagnetic Compounds.* Landolt-Börnstein - Group III Condensed Matter, Volume 41B, Springer-Verlag, 1999.

[94] M. I. D'yakonov, V. A. Marushchak, V. I. Perel', and A. N. Titkov, "The effect of strain on the spin relaxation of conduction electrons in III-V semiconductors," *Sov. Phys. JETP*, vol. 63(3), p. 655, 1986.

[95] A. Gavini and M. Cardona, "Modulated piezoreflectance in semiconductors," *Phys. Rev. B*, vol. 1, pp. 672–682, 1970.

[96] V. F. Gantmakher and Y. B. Levinson, *Carrier scattering in metals and semiconductors*. North-Holl., 1987.

[97] C. Schimeczek and G. Wunner, "Accurate 2d finite element calculations for hydrogen in magnetic fields of arbitrary strength," *Comput. Phys. Commun.*, vol. 185, pp. 614–621, Feb. 2014.

[98] E. Y. Sherman and D. J. Lockwood, "Spin relaxation in quantum dots with random spin-orbit coupling," *Phys. Rev. B*, vol. 72, p. 125340, Sep 2005.

[99] M. Cardona, N. E. Christensen, and G. Fasol, "Relativistic band structure and spin-orbit splitting of zinc-blende-type semiconductors," *Phys. Rev. B*, vol. 38, pp. 1806–1827, Jul 1988.

[100] A. Twardowski, E. Pokita, and J. A. Gaj, "Valence band spin-orbit splitting in CdTe and $Cd_{1-x}Mn_xTe$ and giant Zeeman effect in the Γ_7 band of $Cd_{1-x}Mn_xTe$," *Solid State Commun.*, vol. 36, no. 11, pp. 927–930, 1980.

[101] D. T. F. Marple and H. Ehrenreich, "Dielectric constant behavior near band edges in CdTe and Ge," *Phys. Rev. Lett.*, vol. 8, pp. 87–89, Feb 1962.

[102] M. Cardona, K. L. Shaklee, and F. H. Pollak, "Electroreflectance at a semiconductor-electrolyte interface," *Phys. Rev.*, vol. 154, pp. 696–720, Feb 1967.

[103] K. Heshami, D. G. England, P. C. Humphreys, P. J. Bustard, V. M. Acosta, J. Nunn, and B. J. Sussman, "Quantum memories: emerging applications and recent advances," *J. of Mod. Opt.*, vol. 63, no. 20, p. 2005, 2016.

[104] A. Orieux and E. Diamanti, "Recent advances on integrated quantum communications," *Journal of Optics*, vol. 18, no. 8, p. 083002, 2016.

[105] T. D. Ladd, F. Jelezko, R. Laflamme, Y. Nakamura, C. Monroe, and J. L. O'Brien, "Quantum computers," *Nature*, vol. 464, p. 45, 03 2010.

[106] N. H. Nickerson, Y. Li, and S. C. Benjamin, "Topological quantum computing with a very noisy network and local error rates approaching one percent," *Nat. Commun.*, vol. 4, p. 1756, Apr. 2013.

[107] R. Raussendorf and H. J. Briegel, “A One-Way Quantum Computer,” *Phys. Rev. Lett.*, vol. 86, p. 5188, May 2001.

[108] C. Santori, P. E. Barclay, K.-M. C. Fu, R. G. Beausoleil, S. Spillane, and M. Fisch, “Nanophotonics for quantum optics using nitrogen-vacancy centers in diamond,” *Nanotechnology*, vol. 21, p. 274008, July 2010.

[109] M. W. Doherty, N. B. Manson, P. Delaney, F. Jelezko, J. Wrachtrup, and L. C. L. Hollenberg, “The nitrogen-vacancy colour centre in diamond,” *Physics Reports*, vol. 528, no. 1, p. 1, 2013.

[110] T. Schröder, S. L. Mouradian, J. Zheng, M. E. Trusheim, M. Walsh, E. H. Chen, L. Li, I. Bayn, and D. Englund, “Quantum nanophotonics in diamond [Invited],” *Journal of the Optical Society of America B*, vol. 33, p. 65, Mar. 2016.

[111] R. Nagy, M. Widmann, M. Niethammer, D. B. . R. Dasari, I. Gerhardt, O. O. Soykal, M. Radulaski, T. Ohshima, J. Vučković, N. T. Son, I. G. Ivanov, S. E. Economou, C. Bonato, S.-Y. Lee, and J. Wrachtrup, “Quantum Properties of Dichroic Silicon Vacancies in Silicon Carbide,” *Phys. Rev. Applied*, vol. 9, p. 034022, Mar. 2018.

[112] D. J. Christle, P. V. Klimov, C. F. de las Casas, K. Szász, V. Ivády, V. Jokubavicius, J. Ul Hassan, M. Syväjärvi, W. F. Koehl, T. Ohshima, N. T. Son, E. Janzén, A. Gali, and D. D. Awschalom, “Isolated Spin Qubits in SiC with a High-Fidelity Infrared Spin-to-Photon Interface,” *Phys. Rev. X*, vol. 7, p. 021046, June 2017.

[113] I. Izeddin, M. A. J. Klik, N. Q. Vinh, M. S. Bresler, and T. Gregorkiewicz, “Donor-State-Enabling Er-Related Luminescence in Silicon: Direct Identification and Resonant Excitation,” *Phys. Rev. Lett.*, vol. 99, p. 077401, Aug. 2007.

[114] K. J. Morse, R. J. S. Abraham, A. DeAbreu, C. Bowness, T. S. Richards, H. Riemann, N. V. Abrosimov, P. Becker, H.-J. Pohl, M. L. W. Thewalt, and S. Simmons, “A photonic platform for donor spin qubits in silicon,” *Sci. Adv.*, vol. 3, p. e1700930, July 2017.

[115] C. Beaufils, W. Redjem, E. Rousseau, V. Jacques, Kuznetsov, C. Raynaud, C. Voisin, A. Benali, T. Herzig, S. Pezzagna, J. Meijer, M. Abbarchi, and G. Cassabois, “Optical properties of an ensemble of G-centers in silicon,” *Phys. Rev. B*, vol. 97, p. 035303, Jan. 2018.

[116] D. Press, T. D. Ladd, B. Zhang, and Y. Yamamoto, “Complete quantum control of a single quantum dot spin using ultrafast optical pulses,” vol. 456, p. 218, Nov. 2008.

[117] M. Kroutvar, Y. Ducommun, D. Heiss, M. Bichler, D. Schuh, G. Abstreiter, and J. J. Finley, “Optically programmable electron spin memory using semiconductor quantum dots,” *Nature*, vol. 432, p. 81, Nov. 2004.

[118] M. R. Wagner, G. Callsen, J. S. Reparaz, J.-H. Schulze, R. Kirste, M. Cobet, I. A. Ostapenko, S. Rodt, C. Nenstiel, M. Kaiser, A. Hoffmann, A. V. Rodina, M. R. Phillips, S. Lautenschläger, S. Eisermann, and B. K. Meyer, "Bound excitons in zno: Structural defect complexes versus shallow impurity centers," *Phys. Rev. B*, vol. 84, p. 035313, Jul 2011.

[119] U. Ozgur, Y. I. Alivov, C. Liu, A. Teke, M. A. Reshchikov, S. Dogan, V. Avrutin, S.-J. Cho, and H. Morkoc, "A comprehensive review of zno materials and devices," *Journal of Applied Physics*, vol. 98, no. 4, p. 041301, 2005.

[120] A. B. Djuriić, A. M. Ng, and X. Y. Chen, "ZnO nanostructures for optoelectronics: Material properties and device applications," *Prog. Quantum Electron.*, vol. 34, no. 4, p. 191, 2010.

[121] C. Gonzalez, D. Block, R. Cox, and A. Herve, "Magnetic resonance studies of shallow donors in zinc oxide," *J. Cryst. Growth*, vol. 59, no. 1, p. 357, 1982.

[122] M. Steger, K. Saeedi, M. L. W. Thewalt, J. J. L. Morton, H. Riemann, N. V. Abrosimov, P. Becker, and Pohl, "Quantum Information Storage for over 180 s Using Donor Spins in a 28Si "Semiconductor Vacuum"," *Science*, vol. 336, p. 1280, June 2012.

[123] L. Robledo, L. Childress, H. Bernien, B. Hensen, P. F. A. Alkemade, and R. Hanson, "High-fidelity projective read-out of a solid-state spin quantum register," *Nature*, vol. 477, p. 574, Sept. 2011.

[124] S. C. Benjamin, D. E. Browne, J. Fitzsimons, and J. J. L. Morton, "Brokered graph-state quantum computation," *New J. of Phys.*, vol. 8, no. 8, p. 141, 2006.

[125] R. de Sousa and S. Das Sarma, "Theory of nuclear-induced spectral diffusion: Spin decoherence of phosphorus donors in Si and GaAs quantum dots," *Phys. Rev. B*, vol. 68, p. 115322, Sept. 2003.

[126] A. M. Tyryshkin, S. Tojo, J. J. L. Morton, H. Riemann, N. V. Abrosimov, P. Becker, H.-J. Pohl, T. Schenkel, M. L. W. Thewalt, K. M. Itoh, and S. A. Lyon, "Electron spin coherence exceeding seconds in high-purity silicon," *Nature Mater.*, vol. 11, p. 143, 12 2011.

[127] S. Akasaka, K. Nakahara, A. Tsukazaki, A. Ohtomo, and M. Kawasaki, "$Mg_x zn_{1-x} o$ films with a low residual donor concentration ($< 10^{15} cm^{-3}$) grown by molecular beam epitaxy," *Appl. Phys. Express*, vol. 3, no. 7, p. 071101, 2010.

[128] M. Nakano, A. Tsukazaki, R. Y. Gunji, K. Ueno, A. Ohtomo, T. Fukumura, and M. Kawasaki, "Schottky contact on a ZnO (0001) single crystal with conducting polymer," *App. Phys. Lett.*, vol. 91, p. 142113, Oct. 2007.

[129] B. K. Meyer, H. Alves, D. M. Hofmann, W. Kriegseis, D. Forster, F. Bertram, J. Christen, A. Hoffmann, M. Straßburg, M. Dworzak, U. Haboeck, and A. V. Rodina, "Bound exciton and donor–acceptor pair recombinations in ZnO," *Phys. Status Solidi B*, vol. 241, p. 231, Feb. 2004.

[130] M. R. Wagner, J.-H. Schulze, R. Kirste, M. Cobet, A. Hoffmann, C. Rauch, A. V. Rodina, B. K. Meyer, U. Röder, and K. Thonke, "Gamma_7 valence band symmetry related hole fine splitting of bound excitons in zno observed in magneto-optical studies," *Phys. Rev. B*, vol. 80, p. 205203, 2009.

[131] C. Cabrillo, J. I. Cirac, P. García-Fernández, and P. Zoller, "Creation of entangled states of distant atoms by interference," *Phys. Rev. A*, vol. 59, p. 1025, Feb. 1999.

[132] J. Kim, J. Puls, S. Sadofev, and F. Henneberger, "Charged carrier spin dynamics in ZnO quantum wells and epilayers," *Phys. Rev. B*, vol. 93, p. 045306, Jan. 2016.

[133] S. V. Poltavtsev, A. N. Kosarev, I. A. Akimov, D. R. Yakovlev, S. Sadofev, J. Puls, S. P. Hoffmann, M. Albert, C. Meier, T. Meier, and M. Bayer, "Time-resolved photon echoes from donor-bound excitons in ZnO epitaxial layers," *Phys. Rev. B*, vol. 96, p. 035203, July 2017.

[134] X. Linpeng, T. Karin, M. V. Durnev, R. Barbour, M. M. Glazov, Sherman, S. P. Watkins, S. Seto, and K.-M. C. Fu, "Longitudinal spin relaxation of donor-bound electrons in direct band-gap semiconductors," *Phys. Rev. B*, vol. 94, p. 125401, 2016.

[135] A. V. Khaetskii and Y. V. Nazarov, "Spin-flip transitions between Zeeman sublevels in semiconductor quantum dots," *Phys. Rev. B*, vol. 64, p. 125316, Sept. 2001.

[136] S. M. Clark, K.-M. C. Fu, T. D. Ladd, and Y. Yamamoto, "Quantum Computers Based on Electron Spins Controlled by Ultrafast Off-Resonant Single Optical Pulses," *Phys. Rev. Lett.*, vol. 99, p. 040501, July 2007.

[137] S. E. Harris, "Refractive-index control with strong fields," *Opt. Lett.*, vol. 19, p. 2018, Dec. 1994.

[138] H. Horn, A. Balocchi, X. Marie, A. Bakin, A. Waag, M. Oestreich, and J. Hübner, "Spin noise spectroscopy of donor-bound electrons in ZnO," *Phys. Rev. B*, vol. 87, p. 045312, Jan. 2013.

[139] S. Kuhlen, R. Ledesch, R. de Winter, M. Althammer, S. T. B. Gönnenwein, M. Opel, R. Gross, T. A. Wassner, M. S. Brandt, and B. Beschoten, "Unambiguous determination of spin dephasing times in ZnO by time-resolved magneto-optical pump-probe experiments," *Phys. Status Solidi B*, vol. 251, p. 1861, Sept. 2014.

[140] I. A. Merkulov, A. Efros, and M. Rosen, "Electron spin relaxation by nuclei in semiconductor quantum dots," *Phys. Rev. B*, vol. 65, p. 205309, Apr. 2002.

[141] V. V. Kurshev and T. Ichikawa, "Effect of spin flip-flop on electron-spin-echo decay due to instantaneous diffusion," *J. Magn. Reson.*, vol. 96, p. 563, Feb. 1992.

[142] J. Tribollet, J. Behrends, and K. Lips, "Ultra long spin coherence time for Fe 3+ in ZnO: A new spin qubit," *Europhys. Lett.*, vol. 84, p. 20009, Oct. 2008.

[143] Y. Jiang, N. C. Giles, and L. E. Halliburton, "Persistent photoinduced changes in charge states of transition-metal donors in hydrothermally grown ZnO crystals," *J.of Appl. Phys.*, vol. 101, p. 093706, May 2007.

[144] A. M. Tyryshkin, J. J. L. Morton, S. C. Benjamin, A. Ardavan, G. A. D. Briggs, J. W. Ager, and S. A. Lyon, "Coherence of spin qubits in silicon," *J. Phys. Condens. Matter*, vol. 18, p. 783, May 2006.

[145] W. M. Witzel and S. Das Sarma, "Quantum theory for electron spin decoherence induced by nuclear spin dynamics in semiconductor quantum computer architectures: Spectral diffusion of localized electron spins in the nuclear solid-state environment," *Phys. Rev. B*, vol. 74, p. 035322, July 2006.

[146] M. Chiba and A. Hirai, "Electron Spin Echo Decay Behaviours of Phosphorus Doped Silicon," *J. the Phys. Soc. Jpn.*, vol. 33, no. 3, p. 730, 1972.

[147] K. M. Whitaker, S. T. Ochsenbein, A. L. Smith, D. C. Echodu, B. H. Robinson, and D. R. Gamelin, "Hyperfine Coupling in Colloidal n-Type ZnO Quantum Dots: Effects on Electron Spin Relaxation," *J. Phys. Chem. C*, vol. 114, p. 14467, Sept. 2010.

[148] X. Wu, A. Yamilov, X. Liu, S. Li, V. P. Dravid, R. P. H. Chang, and H. Cao, "Ultraviolet photonic crystal laser," *Appl. Phys. Lett.*, vol. 85, p. 3657, Oct. 2004.

[149] J. C. Johnson, H. Yan, P. Yang, and R. J. Saykally, "Optical Cavity Effects in ZnO Nanowire Lasers and Waveguides," *J. Phys. Chem. B*, vol. 107, p. 8816, Aug. 2003.

[150] S. J. Pearton, D. P. Norton, K. Ip, Y. W. Heo, and T. Steiner, "Recent advances in processing of ZnO," *J. Vac. Sci. Technol. B*, vol. 22, no. 3, p. 932, 2004.

[151] K. Y. Han, S. K. Kim, C. Eggeling, and S. W. Hell, "Metastable dark states enable ground state depletion microscopy of nitrogen vacancy centers in diamond with diffraction-unlimited resolution," *Nano Letters*, vol. 10, p. 3199, aug 2010.

[152] L. Landin, M. S. Miller, M.-E. Pistol, C. E. Pryor, and L. Samuelson, "Optical studies of individual InAs quantum dots in GaAs: Few-particle effects," *Science*, vol. 280, p. 262, apr 1998.

[153] E. S. Kumar, I. P. Anderson, Z. Deng, F. Mohammadbeigi, T. Wintschel, D. Huang, and S. P. Watkins, "Effect of group-III donors on high-resolution photoluminescence and morphology of ZnO nanowires grown by metalorganic vapour phase epitaxy," *Semiconductor Science and Technology*, vol. 28, pp. 045014+, Apr. 2013.

[154] J. M. Kindem, A. Ruskuc, J. G. Bartholomew, J. Rochman, Y. Q. Huan, and A. Faraon, "Control and single-shot readout of an ion embedded in a nanophotonic cavity," *Nature*, vol. 580, p. 201, mar 2020.

[155] D.-H. Kim, H. J. Lee, and G.-C. Yi, "Repeatable switching of the bending direction of ZnO nanoneedles by ion beams," *Nanotechnology*, vol. 23, p. 075302, jan 2012.

[156] W. Q. Li, X. H. Xiao, A. L. Stepanov, Z. G. Dai, W. Wu, G. X. Cai, F. Ren, and C. Z. Jiang, "The ion implantation-induced properties of one-dimensional nanomaterials," *Nanoscale Research Letters*, vol. 8, no. 1, p. 175, 2013.

[157] X. Duan and C. M. Lieber, "Nanoscience and the nano-bioelectronics frontier," *Nano Research*, vol. 8, pp. 1–22, jan 2015.

[158] S. C. Burd, D. T. C. Allcock, T. Leinonen, J. P. Penttinen, D. H. Slichter, R. Srinivas, A. C. Wilson, R. Jördens, M. Guina, D. Leibfried, and D. J. Wineland, "VECSEL systems for the generation and manipulation of trapped magnesium ions," *Optica*, vol. 3, p. 1294, nov 2016.

[159] E. Mount, S.-Y. Baek, M. Blain, D. Stick, D. Gaultney, S. Crain, R. Noek, T. Kim, P. Maunz, and J. Kim, "Single qubit manipulation in a microfabricated surface electrode ion trap," *New Journal of Physics*, vol. 15, p. 093018, sep 2013.

[160] J. J. Pla, K. Y. Tan, J. P. Dehollain, W. H. Lim, J. J. L. Morton, D. N. Jamieson, A. S. Dzurak, and A. Morello, "A single-atom electron spin qubit in silicon," *Nature*, vol. 489, pp. 541–545, sep 2012.

[161] M. Veldhorst, J. C. C. Hwang, C. H. Yang, A. W. Leenstra, B. de Ronde, J. P. Dehollain, J. T. Muhonen, F. E. Hudson, K. M. Itoh, A. Morello, and A. S. Dzurak, "An addressable quantum dot qubit with fault-tolerant control-fidelity," *Nature Nanotechnology*, vol. 9, pp. 981–985, oct 2014.

[162] W. R. L. Lambrecht, A. V. Rodina, S. Limpijumnong, B. Segall, and B. K. Meyer, "Valence-band ordering and magneto-optic exciton fine structure in ZnO," *Phys. Rev. B*, vol. 65, p. 075207, Jan. 2002.

[163] A. V. Rodina, M. Dietrich, A. Göldner, L. Eckey, A. Hoffmann, A. Efros, M. Rosen, and B. K. Meyer, "Free excitons in wurtzite GaN," *Phys. Rev. B*, vol. 64, p. 115204, Aug. 2001.

[164] M. Bayer, G. Ortner, O. Stern, A. Kuther, A. A. Gorbunov, A. Forchel, P. Hawrylak, S. Fafard, K. Hinzer, T. L. Reinecke, S. N. Walck, J. P. Reithmaier, F. Klopf, and F. Schäfer, “Fine structure of neutral and charged excitons in self-assembled In(Ga)As/(Al)GaAs quantum dots,” *Phys. Rev. B*, vol. 65, p. 195315, May 2002.

[165] Y. Don, M. Zielinski, and D. Gershoni, “The Optical Activity of the Dark Exciton,” *arXiv:1601.05530*, 2016.

[166] M. L. W. Thewalt, A. Yang, M. Steger, D. Karaiskaj, M. Cardona, H. Riemann, N. V. Abrosimov, A. V. Gusev, A. D. Bulanov, I. D. Kovalev, A. K. Kaliteevskii, O. N. Godisov, P. Becker, H. J. Pohl, E. E. Haller, J. W. Ager, and K. M. Itoh, “Direct observation of the donor nuclear spin in a near-gap bound exciton transition: P31 in highly enriched S28i,” *Journal of Applied Physics*, vol. 101, p. 081724, Apr. 2007.

[167] P. P. Paskov, T. Paskova, P. O. Holtz, and B. Monemar, “Spin-exchange splitting of excitons in GaN,” *Phys. Rev. B*, vol. 64, p. 115201, Aug. 2001.

[168] V. Niaouris, X. Linpeng, M. Viitaniemi, and K.-M. C. Fu, “Ensemble spin relaxation studies of shallow donor qubits in zno,” *in preparation*, 2020.

[169] X. Han, C. Xiong, K. Y. Fong, X. Zhang, and H. X. Tang, “Triply resonant cavity electro-optomechanics at x-band,” *New Journal of Physics*, vol. 16, p. 063060, jun 2014.

[170] A. Banholzer, R. Narkowicz, C. Hassel, R. Meckenstock, S. Stienen, O. Posth, D. Suter, M. Farle, and J. Lindner, “Visualization of spin dynamics in single nanosized magnetic elements,” *Nanotechnology*, vol. 22, p. 295713, jun 2011.

[171] A. C. Torrezan, T. P. M. Alegre, and G. Medeiros-Ribeiro, “Microstrip resonators for electron paramagnetic resonance experiments,” *Review of Scientific Instruments*, vol. 80, p. 075111, jul 2009.

[172] O. Benningshof, H. Mohebbi, I. Taminiau, G. Miao, and D. Cory, “Superconducting microstrip resonator for pulsed ESR of thin films,” *Journal of Magnetic Resonance*, vol. 230, pp. 84–87, may 2013.

[173] E. Yablonovitch, B. J. Skromme, R. Bhat, J. P. Harbison, and T. J. Gmitter, “Band bending, Fermi level pinning, and surface fixed charge on chemically prepared surfaces,” *Appl. Phys. Lett.*, vol. 54, no. 6, pp. 555–557, 1989.

[174] W. Bludau and E. Wagner, “Impact ionization of excitons in GaAs,” *Phys. Rev. B*, vol. 13, pp. 5410–5414, Jun 1976.

[175] W. Rosner, G. Wunner, H. Herold, and H. Ruder, "Hydrogen atoms in arbitrary magnetic fields. I. Energy levels and wavefunctions," *J. Phys. B: At. Mol. Phys.*, vol. 17, no. 1, p. 29, 1984.

[176] Z. Li-Bo and D. Meng-Li, "High Accuracy Calculation for Excited-State Energies of H Atoms in a Magnetic Field," *Commun. Theor. Phys.*, vol. 52, no. 2, p. 339, 2009.

[177] G. E. Pikus, V. A. Maruschak, and A. N. Titkov, "Spin splitting of energy bands and spin relaxation of carriers in cubic III-V crystals," *Sov. Phys. Semicond.*, vol. 22, p. 115, 1988.

[178] R. Winkler, *Spin–orbit coupling effects in two-dimensional electron and hole systems.* Springer, 2003.

[179] E. L. Ivchenko and G. E. Pikus, *Superlattices and other heterostructures: symmetry and optical phenomena.* Springer, 1997.